2015-04-06

Statistical properties of defect turbulence in two and three dimensions

St-Yves, Ghislain

UNIVERSITY OF CALGARY

Statistical properties of defect turbulence in two and three dimensions

by

Ghislain St-Yves

A THESIS

SUBMITTED TO THE FACULTY OF GRADUATE STUDIES

IN PARTIAL FULFILLMENT OF THE REQUIREMENTS FOR THE

DEGREE OF DOCTOR OF PHILOSOPHY

DEPARTMENT OF PHYSICS AND ASTRONOMY

CALGARY, ALBERTA

February, 2015

Abstract

Spatiotemporal chaos in oscillatory and excitable media is often characterized by the presence of phase singularities called defects. Understanding such defect mediated turbulence is an important challenge in nonlinear dynamics. This is especially true in the context of ventricular fibrillation in the heart, where the mechanism leading to ventricular fibrillation, and the importance of the thickness of the ventricular wall, is contentious. Here, we study defect mediated turbulence arising in many regimes of conceptual models of oscillatory and excitable media and investigate the statistical properties of the turbulent state that results.

Two central ideas are put under scrutiny. First, that the turbulence is driven, and its observables influenced, by the mechanism of breakup and second, that the dimensionality of the medium leads to a different, potentially more complex, turbulence. We find evidences that support the idea of instability driven turbulence for different 2-dimensional instabilities. Furthermore, breakup from purely 3-dimensional instabilities offers a completely different mechanism. For 2D mechanisms in 3D media, we find that the thickness of the medium does not have a significant influence far from onset in fully developed turbulence while there is a clear transition in behavior if the system is close to a spiral instability. We further provide clear evidence that the observed transition is purely a consequence of the dimensionality of the medium. Using 3D defect tracking, we show that the statistical properties arising from 2D instability driven turbulence are different from those in turbulent regimes arising from 3D instabilities, but only close to onset.

As a consequence of this study, we are lead to the counterintuitive conclusion that even in the absence of pure 3D instabilities, 3D simulations may be necessary to capture even the simplest statistical feature of the turbulent behaviour of real 3D systems. However, even if the 3D statistics are different from the 2D ones, they are not distinguishable in a general context, a conclusion that opposes a previous conjecture.

Acknowledgements

I am of course indebted to my supervisor Joern Davidsen, whom I know, even though we may not always have pushed the limits of all things academic together, works for his students and supports them in his own way — Sometimes only by not unduly interfering and serving as an administrative paperwork protection buffer. There is some wisdom in that. I am also very grateful for all the years of discussions, stimulation, and encouragement from my collegues and friends in Calgary. In particular, a special thanks to Aicko, Claire, Golnoosh, Ali, Fernando, Christiane, Elliot and Chad, and to others as well. Also to my friends back in Québec whom I saw very little in the past years, but whom I still cherish. Finally, I wish to thank my family for their support. They must be wondering what I'm still doing in school after all these years of mystery. If I knew I would tell them.

Table of Contents

List of Tables

List of Figures and Illustrations

List of Symbols, Abbreviations and Nomenclature

Symbol	Definition
AP	Action potential
APD	Action potential duration
AT	Amplitude turbulence
BF(I)	Benjamin-Feir (instability)
CFD	Cumulative Frequency Distribution
CGLE	Complex Ginzburg-Landau equation
DDDT	Dimension dependent defect turbulence
DI	Diastolic interval
DMT	Defect mediated turbulence
ECG	Electrocardiogram
EI	Eckhaus instability
FT	Filament turbulence
IDDMT	Instability-driven defect mediated turbulence
NLT	Negative line tension
PDF	Probability Density Function
PLT	Positive line tension
PO	Peroxidase Oxidase
RD	Reaction-diffusion
RFD	Relative Frequency Distribution
SDL	Synchronization defect line
ST	Strong turbulence
STC	Spatiotemporal chaos
VF	Ventricular fibrillation

WT	Winfree turbulence
$\vec{A}(\vec{r},t)$	Solution field
$C(\lvert\Delta\vec{r}\rvert)$	Spatial correlation function
$h(\lvert\Delta\vec{r}\rvert)$	Pair correlation function
L	Real linear size of the medium
L_z	Thickness of the medium
N	Number of nodes in the simulation along one direction
Δx	L/N: Discretization size
Δt	Time interval of the simulation
Δs	Sampling interval. The time interval of the analysis
D	Diffusion constant
$\hat{D}$	Diffusion tensor
l	Length of a filament
q	Topological charge of a defect
n	Number of defects
$\langle n\rangle$	Average number of surface defects
σ_n	Standard deviation of the time series of surface defects.
$\bar{n}$	$n/\langle n\rangle$: Normalized number of defects.
ϕ	A phase
$\phi(\vec{r})$	A phase field
V	Volume of the system
A	Total surface of the system
$A_\perp$	Cross section of a system with normal $\hat{z}$
$\tilde{n}$	$\langle n\rangle \times A_\perp/A$: Normalized surface defect density
E	Transmembrane voltage
$r_e(n)$	Rate of event e as a function of n

γ_n	$2\sigma_n^2/\langle n \rangle$: Shape factor of the distribution of defects
$\bar{c}_0$	Normalized constant creation rate component
n-span	Number of defects in a cluster of defects
t-span	Total lifetime of a cluster of defects
α	Exponent of the tail of the n-span distribution of defects
γ	Exponent of the tail of the t-span distribution of defects
κ	Exponent of the tail of the length distribution of filaments

Chapter 1

Introductory matter

Chaos, in its vernacular usage, means a state of confusion, of disorder. It was thought to be the state of matter before the creation of distinct and orderly forms [1]. The politician may think of chaos as anarchy, i.e. the absence of government, lawlessness, etc. However, chaos isn't without law[1]. To the physicist, it has acquired a rather specific meaning during the 20th century. Chaos is a regime of certain dynamical systems which are extremely sensitive to the particular initial conditions and to small disturbances, and whose bounded asymptotic behavior is neither stationary nor periodic [2, p. 323]. The trajectories of such systems often have the appearance of being random or disordered though they still satisfy the simple, usually fully deterministic, dynamical laws of the system. In short, chaos for the physicist is not lawlessness, it is not confusion and there is order.

It is hard to generalize what we know about chaos because the phenomenon spans a large class of dynamical system whereas, say ordinary differential equations, are just one type of dynamical system among many. Most of what we know concerns the basic concepts and method to assess the presence of chaos in a dynamical system, as well as a knowledge of the ways in which regular dynamics can degenerate into a chaotic one (bifurcation theory of low dimensional systems). Experimentally, these concepts and methods permit us to detect chaotic behavior in real-world and experimental systems and, if we do not possess a definite model, to accept on ground of plausibility that these systems may yet yield to a profound explanation in terms of simple rules even though the trajectory of the system may appear extremely complex. These simple rules may be derived from elucidating the forces that are at play, the mechanism of action of some enzymes, or some particular connection of a network. Although it seems simple in principle, it often proves difficult and many assumptions

[1] Anarchy neither for that matter, it is self-law in government.

and simplifications have to be made such that many models are produced this way, with no *a priori* means of selection. Luckily, our understanding of bifurcation and chaos also constrains the models such that certain transitions and observables make certain demands on the particular form of the underlying dynamical model. For instance, a chaotic regime that requires a certain minimum embedding dimension imposes a lower bound estimate of the dimension of the dynamical system that would represent the phenomenon faithfully.

Most of our tools to assert the presence of chaos in low dimensional systems have to do with measuring the Lyapunov exponents either directly from numerical simulations [3, 4] or from a measured time series of the trajectory of the system [5]. These exponents also characterize the chaotic attractor dimension, which can also be assessed using other, often less costly, methods such as by measuring the correlation dimension of the fractal attractor [6]. These dimensions are single numbers characterizing the dynamical complexity of the chaotic attractor (the dynamical state the system happens to be in) and correlates inversely with how far one can expect to be able to make accurate prediction of the future state of the system. Predictability is, of course, the name of the game. The ability to predict future markets is what investors rely on to make profit. Our ability in the prediction of weather is what farmers rely on to make profitable decisions on when to work the fields, and what emergency services rely on to issue tornado warnings. Our ability in the prediction of heart arrhythmia could eventually help determine a proper course of medical treatment, potentially saving lives, and so on. Note how, in all these cases, the chaotic nature of these systems transforms deterministic predictions into a probabilistic forecast.

Another picture of chaos which has struck the public's imagination is the infamous butterfly effect. It became synonymous with the unpredictable effect of small or unknown causes and reflects the sensitivity to initial condition of chaotic systems. In this imagined scenario, a butterfly flapping its wings on one side of the world could cause a hurricane on the other side. Small perturbations grow. In this case however, the system (earth's atmosphere) is

very high dimensional and talking of the trajectory of the system fails to evoke a clear picture of what is really going on in the system. Therefore, we are naturally led to resort to a description of *patterns* and speak of the weather, wind and hurricanes and perturbations like an airplane or butterfly producing vortices and currents. Not all these local patterns evoke the idea of chaos (or turbulence) and, on the other extreme, apparent chaos may be local and, with suitable coarse graining, weather appears almost periodic over a year. Any attempt at a description thus has to first choose what it wants to describe and the scale of the phenomenon of interest. In certain cases though, the system itself presents conspicuous features at a certain scale and so the choice appears to be made for us. All that remains in these cases is to suitably represent the system such that all behaviors at the scale of interest are faithfully represented. This is a difficult problem in and of itself in general and considerable efforts are still being devoted to it [7].

Not all dynamical systems show interesting patterns. The states of systems in thermal equilibrium are always time-independent and often uniform and homogeneous. The most interesting and intricate fractal-like behaviors exist only in non-equilibrium systems. While the turbulent patterns we observe in fluid dynamics either come from local variation of pressure and velocity field, in absence of convection, only the local concentrations of particles (roughly equivalent to the pressure at fixed temperature) form the contour of the patterns. However, the Second Law of thermodynamics cannot be escaped and steady nonequilibrium conditions have to be maintained externally to observe steady patterns. The most common mechanism for maintaining the system out of equilibrium for pattern formation in fluids comes from the perpetual transport or convective flow maintained mechanically or thermally. In the absence of convection, we must look for another mechanism to supply energy to our system. Resupplying an ongoing chemical reaction[2], thereby maintaining it out of chemical equilibrium, offers such a means. For this reason, systems whose dissipation mechanism

[2]There is, of course, material flow in the resupply tubes but only a negligible one in the reaction vessel which is system under consideration

occurs purely through diffusion and are maintained away from chemical equilibrium are called reaction-diffusion (RD) systems. RD systems are much simpler than their fluid dynamics parents. Nevertheless, they yield similar chaotic-like solutions reminiscent of turbulence in hydrodynamical systems. In the remainder of this thesis, turbulence always refers to the spatiotemporal chaos found in RD system, which we shall describe in more detail later. In spite of their relative simplicity, they yield an abundant spectrum of behavior, transition and patterns.

Not only are RD systems rich enough to entertain us, they are also of extreme relevance. Homeostasis, a concept almost equivalent to the idea of life itself, means the maintaining of relatively constant conditions away from equilibrium. Furthermore, the inter- and intracellular media are gel-like [8, p. 78] and effectively not stirred (without convection) and, disregarding active transport which must nevertheless be prevalent, diffusion is the only other possible dominant form of dissipation. Hence it does not come as a surprise, even if instances may be difficult to observe, that we find many examples of pattern formation (modeled accurately with RD systems) in the context of life. Chemical waves are often implicated in the mechanisms responsible for biological function [9, 10, 11, 12, 13]. In particular, chemical spiral waves are known to play a role in signaling processes leading to cell division [14], intracellular calcium waves in oocytes [15], aggregation processes and morphogenesis in colonies of the amoeba Dictyostelium [16, 17, 18], and the pumping action of the heart [19, 20, 21], to name a few specific examples. These kinds of chemical waves are not limited to the living world. However, homeostasis cannot account for the maintaining of the near steady out-of-equilibrium dynamical state in those cases. Very often, a state of equilibrium is only reached after multiple pattern time-scale (e.g. many transient local oscillations) such that the conditions in a short time interval are almost constant, though never exactly, or maintained away from equilibrium artificially by manipulating the boundary conditions (i.e. input/output of reagents) in experimental settings. For example, electroconvection in

liquid crystal [22], catalytic oxidation pattern on a surface of platinum [23, 24] and a panoply of patterns and bifurcations in the non-stirred Belousov-Zhabotinsky (BZ) reaction [25, 26] are classic laboratory case studies of RD pattern forming systems.

1.1 Pattern forming systems

What is a pattern forming system? Any sufficiently complex system; complex enough that it is more aptly described by a high level theory than by the lowest level known, could be called a pattern forming system[3]. Indeed, the new language of the high level theory is only justified as long as it identifies some regularities that are beyond the scope of the low level theory[4]. Such regularities are patterns in the broadest sense. However, when we talk about pattern forming system, we usually have a more precise context in mind. Indeed, we always refer to spatially extended domain, either discrete (lattice) or continuous (field), whose local values, also discrete or continuous, trace the so-called pattern. The pattern is therefore like the outline of a picture. There is another element essential to having a pattern *forming* system i.e. that this pattern is produced by self-organization i.e. spontaneous symmetry breaking out of the otherwise more symmetric dynamics of the system. Hence, pattern forming systems cannot exist without a notion of time or timing for the system, which can also be discrete or continuous. Another way of saying this is that pattern forming systems can't be understood separately from a dynamical perspective – the patterns are not

[3]Note that I do not assume a reductionist view of reality. Ultimately, patterns are relative to a certain description, and descriptions are intimately linked to theories. If one want to describe a tree, one could simply point at a tree and say "this is a tree". A this level of description, no pattern of tree is possible, things just are things in themselves. Then someone else could say that trees are composed of certain things into certain arrangements. The set of all these arrangements that are trees is a pattern. The pattern describes a certain regularity of structure. This philosophy of nature is, as far as the current understanding of this author goes, the only one that is consistent with the ever ongoing quest for "reality" of science and the fact that theories along the way in this process also happen to "work". A reductionist view falls appart at every revolution, whereas a pattern view is always ready for further details in the description or even a complete change of paradigms.

[4]"[...]beyond the scope of the low level theory" must not be construed as a hard limit. Scope of theories are changed, improved, and moved all the time. In this case, certain patterns might be within the scope of the underlying theory while others aren't, though they might be one day.

a result of the mere extremum of some physical quantity. Finally, even though the dynamics itself is always acting, the pattern formed can be either static (fixed point of the dynamics) or dynamic (the pattern has its own dynamics which can be very intricate). The various possible representations of pattern forming systems are summarized in Table 1.1.

Space	Time	State	Type of pattern forming system
Continuous	Continuous	Continuous	Partial Differential Equation
Discrete	Continuous	Continuous	Coupled Ordinary Differential
Discrete	Discrete	Continuous	Coupled maps
Discrete	Discrete	Discrete	Cellular Automata

Table 1.1: Different representation of pattern forming systems [27, p. 201].

As per the examples listed above, we will be exclusively interested in the case of continuous time and space since this is the most apt representation of non-stirred chemical reactions, electro-physiological systems like muscles, neuron fibers (not network of fibers), heart tissues, etc. However, the other representations also have their advantage in some situations. For example, coupled differential equations seem most appropriate in scenarios involving networks of continuous state units like neural networks or chemical systems where the reaction is only allowed on some spatially localized subunit, but where the reactant can travel diffusely from one unit to another on a fast time scale (see for example our paper on chimera state for an example of globally coupled differential equation systems and a novel pattern emerging as a result [28]). In all these cases, space is heavily anisotropic i.e. information only travels along specific directions. Alternatively, in cases where one or more chemical species travel almost instantly with respect to other time scales, it may be more adequate to simulate global space-independent coupling [29]. The same sort of conceptual simplification can be used in systems that toggle rapidly between a basal and an active state (or any other number of discrete states) which can be adequately represented by a cellular automata model, given that we have some insight on the dynamics of these states.

In this thesis, we shall exclusively consider pattern formation models that fall under the

category of RD systems. All RD systems take the general condensed form

$$\partial_t \vec{A}(\vec{r},t) = \vec{F}\left(A_1, A_2, \ldots A_N; \lambda\right) + \vec{\nabla}\hat{D}\vec{\nabla}\vec{A} \tag{1.1}$$

where $\vec{F}$ is a N-vector of ODEs (the local reaction part) with λ as a set of control parameters. The diffusion tensor $\hat{D}$ characterizes the diffusion of all species $\vec{A} = (A_1, A_2, \ldots A_N)$ in all possible directions. Its simplest expression is a diagonal matrix with coefficients $(D_a, D_b, \ldots)$ and describes the case where all species diffuse homogeneously and isotropically. Needless to say, RD models have been used successfully to represent a wide variety of phenomena in many of the systems mentioned above [27].

1.2 Common patterns and stability

Surprisingly, the patterns found in many of these systems, biological or otherwise, are remarkably similar. In the course of this thesis, we shall describe some characteristics of these patterns in more detail but for now we simply want to bring the attention to the seemingly generic character of the patterns presented by a multitude of systems. First there are the steady patterns like the simple steady state, steady stripe and spot patterns and the labyrinthine patterns of morphogenesis process [30] which evoke, in particular, animal pigmentation patterns. Then there are the dynamical patterns like propagating waves, target patterns and dynamical spots, stripes, lattice structures and spiral waves of various periodicity. In three dimensions, spirals become elongated scroll waves that can form helical coils, rings, and complex loops and tangles of scrolls. Finally, when these dynamical patterns, spiral patterns and tangles of scroll waves become highly irregular, we have states that fall under the mantle of spatiotemporal chaos (STC) which are characterized by the disappearance (exponential decay) of long range spatial and temporal correlations. Specifically, the spatial correlation function is defined as

$$C(|\Delta\vec{r}|) = \langle A(\vec{r},t)A(\vec{r}+\Delta\vec{r},t)\rangle_{\vec{r},t} - \langle A(\vec{r})\rangle^2_{\vec{r},t}\,, \tag{1.2}$$

where $A(\vec{r}, t)$ is any one of the field component of $\vec{A}$ in Eq. 1.1 and $\langle \cdot \rangle_{\vec{r},t}$ signifies the average over $\vec{r}$ and t. A similar correlation function can be defined for the temporal correlations. Examples of the previous patterns found in simulation of RD systems are shown on Figure 1.1.

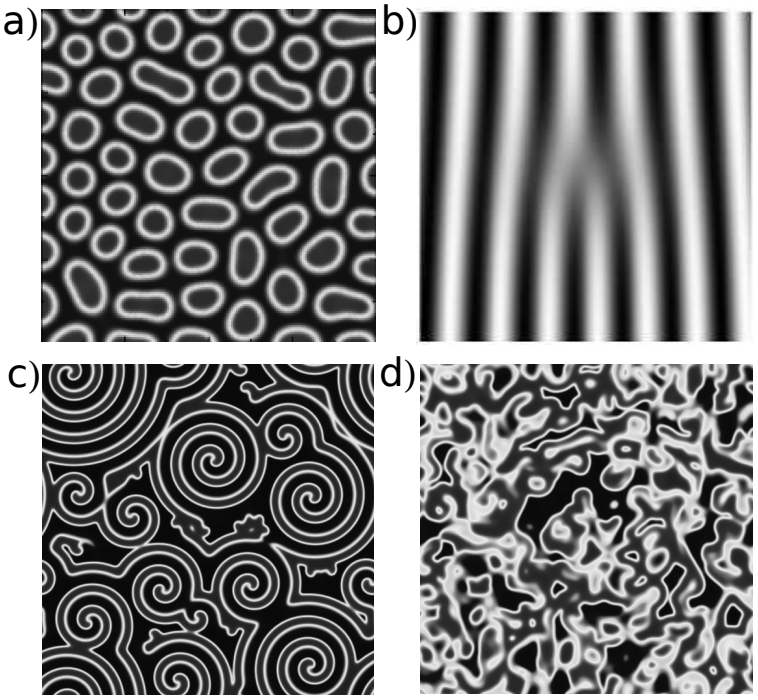

Figure 1.1: Patterns in simulations of RD systems. a) Spot pattern from Turing instability of the uniform state (H. U. Bödeker/ Wikipedia Commons/ CC BY-SA 3.0). b) Stripe pattern with a single dislocation (defect of wavenumber). c) Spiral turbulence and d) Amplitude turbulence. Both c) and d) contain a multitude of vortices or phase defects. b), c) and d) are my own work.

A single system may show multiple patterns. Patterns are selected depending the initial conditions, boundary conditions and values of control parameters of the system. A pattern is analogous to an attractor for a low-dimensional system. Attractors are invariant manifolds and, while the state of the system on a stable invariant manifold may change over time according to the dynamics, the manifold itself on which the trajectory lies does not vary. Formal proof of the existence of a low-dimensional chaotic attractor took decades to be produced, even for relatively simple ODE systems like the Lorenz equations [31, 32], even

though the presence of chaotic attractors had long been suspected. Likewise, even if the existence of invariant manifolds for high-dimensional chaos is uncertain, or their relevance to the phenomenon of turbulence contentious [33], the analogy between patterns and attractors remains a strong and necessary one. Patterns may be dynamical and changing, like the trajectory on the attractor, but the question of the stability of the pattern is determined by the invariance of some statistical measures. When these measures do not vary in time, the pattern is said to be stable. Patterns change into other patterns when they become unstable. The stability of the pattern is therefore of paramount importance.

Linear stability[5] , numerical linear stability and evaluation of Lyapunov exponents are tools to assess the stability of attractors and of patterns. When a pattern loses stability, it is replaced by a stable one after some transient period. This rule enforces a conceptual and logical hierarchy of patterns which goes more or less as follows. There is always a region of parameter space that corresponds to some state with low forcing vs. dissipation and where nonlinearity plays only a small negligible role. In such a regime, the system rapidly settles on a stable fixed point and the corresponding pattern is a uniform state. This is, of course, excruciatingly boring. Then the driving force vs. dissipation (which is represented by the control parameter λ) is increased and, at some critical value of that control parameter λ_c, the uniform state becomes unstable. It doesn't become unstable arbitrarily: a certain mode or set of modes (depending on the symmetries of the dynamics) start to grow first and nonlinearities usually (in the case of supercritical instabilities) are such that the pattern saturates into something that resembles these modes (stripes, lattice, convection cells, etc.). Such an instability of the uniform state is called a *primary instability* and the new saturated state is called a *nonlinear state*. That the nonlinear states happen to be close in form to the unstable modes is indeed a convenient coincidence and doesn't have to remain so. Carrying

[5]Linear stability describes the behavior of small perturbations close to certain state by the linearized dynamics of the governing equation around that state. As per linear dynamics, small perturbation can only shrink, be steady or grow and can be oscillatory (complex eigenvalue of the linear operator) or not. This classifies entirely the linear stability of states.

on with the procedure, the nonlinear state is also subject to the same analysis and can eventually lose its stability with enough forcing. Instability of nonlinear states are called *secondary instabilities* and so, it would appear, the game repeats.

There is, however, an additional complication along the way of the seemingly simple procedure outlined above which is that many of the most complex patterns do not grow continuously from other patterns. This is the case of subcritical bifurcations. In other words, there can't be any perturbation theory where one assumes that the solution is close to a certain state and change only the values or parameters a little bit to find a perturbed solution. The new state is an all or nothing deal, and so, it often demands new concepts and methods even for the most basic characterization.

Furthermore, from the perfect symmetry of the uniform state, we cannot directly account for the symmetry breaking patterns that are observed in nature and in models (Figure 1.1) without considering the boundary conditions of the system (or the initial condition if the current state didn't grow from the uniform state as we have described) or some transient modifications to the dynamics (e.g. perturbations such as touching the medium with a stick or thermal fluctuations). The reason is that, in such cases, the patterns selected by the aforementioned process is at odds with the boundary conditions of the medium and a defect in the regularity of the description is bound to appear to restore the demands enforced by the boundaries. Likewise, certain "regular" patterns are already symmetry broken to begin with. Indeed, at the center of a spiral wave there is an unavoidable phase singularity or vortex (a.k.a. topological defect or simply *defect*), which is a point that does not oscillate like the others and where no phase can be ascribed. Likewise the center locus of scroll waves forms a line of vortex (a.k.a. filament or defect in 3-dimensions). From there also, the problem of linear stability usually becomes mathematically intractable due to the complexity of the patterns and we need to change our language somewhat. We can still study the stability of certain structures numerically in a limited sense, to great insights, but the stability of any

actual pattern (even a simulated one) always turns out more complicated than that of the simple regular structures.

1.3 Topological defects in science

Topological defect is a concept common to many branches of physics because most theories are amenable to a geometric interpretation, and the defects are in a sense the simplest example of the limitation of the description. Although the general causes for the appearance of defects are related, there are various subtleties, and various types of defects depending on the nature of the aforementioned description. First, let's look at some aspect of defects in the context of patterns. We read that

> A defect can be thought of as a local imperfection in an otherwise perfect pattern, and experimental and natural patterns often contain many defects, either due to the effect of boundaries or due to a spatially inhomogeneous initial condition. [27, p. 279, par. 2]

In this sense, it is something that breaks the regularity of the description. Many pattern forming systems show regions of different local order separated by a boundary. These breaks in the local order are defects in the large sense. The previous interpretation also seems to imply that defects are a practicality, i.e. that they are the result having realistic conditions in a model or in a phenomenon. However, we know that some patterns, even though they may accept a simple "regular" mathematical description, possess points or a locus of points where a given description is inapplicable or yields a singularity i.e.

> [...] a place where slopes become infinite, where the rate of change of one variable with another exceeds all bounds, and where a big change in an observable is caused by an arbitrarily small change in something else [13, p. 71, par. 3].

However, it seems necessary to distinguish two types of defects in patterns. First there are the essential defects which are present as a consequence of the organization of the perfect mathematical pattern itself and cannot be eliminated by removing some sort of imperfection, noise or changing the boundary conditions. On the other hand, there are non-essential defects which are the intersections of regions with different local order (e.g. boundaries) and may appear for various practical reasons.

Defects can be of any dimension depending on the context. In N-dimensional media, an $(N-1)$-dimensional hypersurface locus mark the boundary between two hypervolumes with different local order. Point defects exist in any dimension greater than zero and higher dimensional defects exist in higher dimensions under different names; hole, vortex, filament, string, boundary, texture, etc. However, we will not cover all of this zoo of defects. Our interest in defects will focus on loci of points where the rate of change of the phase with respect to the position is infinite. At these points, the phase itself is undefined and there is a phase singularity. We will return to the practical definition and identification of these points in section 2.1.2. For now, let's consider further the significance of these loci of phase singularities. It is essential to recall that a singularity is something that is part of a certain model since

> Singularities underly limitations in our basic concept to describe the situation. They do not occur in nature, only in the models. [13, p. 72, par. 2]

Indeed, phase singularities are the result of us forcing a periodic quantity model (in our cases, this "model" usually corresponds to the reaction part of our RD system) on a local field variable which is, itself, not always periodic but sufficiently so that it is not completely absurd to apply the periodic model. The complete RD system is usually not perfectly periodic because of the interaction (diffusion), which is what permits wave propagation and the emergence of complex patterns in the first place. On the other hand, this interaction often

slaves nearby or even far-away regions of the system such that the effective dimension of the medium (the number of degrees of freedom needed to describe the situation) is tremendously reduced. The possibility of a reduced dimension description is always at the forefront of research because it potentially can reduce an intractable problem to manageable one, and lead us in our understanding of the phenomenon. In this, essential defects often act as organizing centers which provide the possibility for a reduced description.

1.4 Defect mediated turbulence

Many regimes in RD systems are dominated by the unceasing breakup of waves corresponding to the creation and annihilation of new topological phase defects [34, 35, 36, 37]. Such a state of *defect mediated turbulence* (DMT) is one important and common case of STC in pattern forming systems. The *mechanism of breakup* that maintains the spatiotemporal chaos appears strongly dependent on the particular regime of the system, and possibly on the instabilities, or class of instabilities, of spirals that preceded it. We shall come back to this question in detail in Chapters 3 and 4.

Contrary to regular stationary or periodic patterns, the description of a complex spatiotemporally chaotic state *demands* a statistical perspective and the state can only be said to be stable with respect to the stationarity of the statistical description. In the seminal work of Gil *et al.* [34, 38] on DMT in the complex Ginzburg-Landau equation (CGLE), the defects were assumed to be statistically independent entities that are created and annihilated at a rate dependent (or independent, as may be the case) on the number of defect pairs[6] already present in a certain volume. Therefore, the probability distribution of the number of defect pairs $p(n,t)$ at any time t satisfies the master equation

$$\frac{\partial p(n,t)}{\partial t} = r_+(n-1)p(n-1) + r_-(n+1)p(n+1) - (r_-(n) + r_+(n))\,p(n) \tag{1.3}$$

[6]As we will see in chapter 2, topological phase defects are created and annihilated pairwise and so, only the defect pairs act as independent entities. The pairs correspond to pairs of defects of opposite topological charges.

where $r_+(n)$ and $r_-(n)$ are the total creation and annihilation rates in that volume. Demanding the stationarity of this distribution for turbulent steady states, which seems to be a demand based on the existence of a high-dimensional attracting manifold for the solution[7], yields the condition

$$p(n) = \frac{r_+(n-1)}{r_-(n)} p(n-1), \tag{1.4}$$

subject to the boundary condition at $p(0)$ and normalization condition $\sum_{n=0}^{\infty} p(n) = 1$. Based on the creation process of new defect pairs due to the random fluctuations of the field in the CGLE, the creation rate was assumed (and found) to be essentially constant $r_+(n) = c$ and independent of the presence of other defects. However, the annihilation rate was found to be proportional to the square of the number of defects $r_-(n) = an^2$, corresponding to a uniform chance of any oppositely charged defect to collide with any other. This was shown to generate a square poissonian distribution of defect pairs $p(n) \propto (c/a)^n / (n!)^2$. This model of defects is thereafter referred to as the null model. Gil *et al.*'s work has seen many successors generalizing their type of mean field description, or other statistical descriptions, of the population of defects. It has been shown that with reasonable assumptions, one can account for different boundary conditions [24, 42], different generating mechanisms [43] and the presence of noise [44]. These results have also been found to be in remarkable agreement in various experimental systems [42, 45, 24].

However, it is extremely likely that such a statistical model of defects is an unavoidably incomplete description. From a similar discussion on the description of a perturbed stripe state far from onset (whose properties are more mathematically well-defined),

> We might hope to get a complete description of the pattern dynamics, even far from threshold, in terms of two coupled descriptions, a phase dynamics that describes a slow spatial variation in

[7] This is an intuitive understanding based on the extensive behavior of the attractor dimension in one and two dimensional spatiotemporally chaotic systems [39, 40, 41]. This high dimensionality may factorize however.

> the vicinity of a defect, and a fast local dynamics that describes the response of a topological defect to the phase dynamics. [...] Difficulties that arise are the need for rules defining how topological defects are created in regions of large pattern deformation, and how defects with opposing winding number may annihilate when they get close enough [27, p. 319, par. 5].

The previous statistical description of (vortex) defect falls under the second part of this program (phase description vs. defect description), and the rules of creation of new topological defects is what we know as the breakup mechanism. In the case presented above, the breakup mechanism is a response to the apparent random fluctuation of the phase dynamics, which is deemed random and intractable. However, a close inspection of other turbulent states, which is what we shall be concerned about in this thesis, should reveal that this is not the only breakup mechanism and that the phase dynamics may play a more or less active role in determining how the breakup occurs in certain cases.

Also regarding the incompleteness of the statistical description, it has been shown by direct measurements of fractal dimension in small 2D STC states of the CGLE [39] that the overall fractal dimension carried by the defects only accounts for a fraction of the total attractor dimension. Therefore, a significant fraction of this dimension remains in the chaotic fluctuation of the fields. This leads to an interesting issue: while we can certainly characterize the pattern through its defects[8], there remains the question of what exactly is being characterized in the process, and what remains purely in the field and would require a concurrent "phase" description. Also, irrespective of the completeness of the description, the previous statistical description appears *ad hoc* and without connection to neighboring states i.e. that the current model does not indicate, nor drive us to expect, that the statistics may scale in a certain way close to certain transitions either when the turbulent state is formed

[8]We "can" in the sense that nothing is stopping us!

or near new types of non-equilibrium phase transitions.

Nevertheless, even in an incomplete description, the topological defects often organize the turbulence. We all know that the first way to reduce the apparent complexity in physical problem is to identify suitable symmetries. By identifying the symmetries, we effectively slave degrees of freedom to one another in the description. For example, uniform states have continuous translational and rotational symmetries while spirals have discrete rotational symmetries only. Fixed points have continuous time translational symmetries while periodic oscillations have only discrete one. In a change from uniform to spiral pattern, or fixed point to oscillatory, many symmetries are lost. In this picture, defects are remnants of previous symmetries. For instance, spiral waves have a central topological defect that is essentially a fixed point which possess more symmetries than any other points. Often the symmetries that such point possess are remnants of symmetries that were shared by the whole pattern before it underwent a transition or bifurcation. Another example is the synchronization defect lines found in period doubling bifurcation of spirals [46]. These loci possess a periodicity lower than that of the bulk of the medium i.e. the periodicity before the period doubling and act as boundary for the synchronization of spatially extended domains. Now that we have introduced the type of pattern forming system and the type of phenomenon we will be concerned about, let us go back to a specific system and describe in more detail its anatomy and how patterns, defects, STC and DMT might relate to real world phenomena and possible applications either involving these states, or as form of control over these uncoordinated states.

1.5 Motivations

In this section, we will attempt to motivate our main questions and direction of approach. First, we will explore the case of the heart dynamics which lies at the confluence of many avenues of research. We shall then use this example as a motivation for more general questions

regarding spatiotemporal chaos and defect mediated turbulence.

1.5.1 A multilevel complex system: Fibrillation in the heart

Ventricular fibrillation (VF) is a state of spatiotemporal disorder and incoherent electrical activity encountered in the heart. It is the leading cause of death in industrialized countries [47]. From a purely scientific perspective, the breadth of approaches and studies that focus on elucidating the mechanisms that lead to, are causes of, and treatment of, VF is quite amazing and ranges from *ab initio* molecular dynamics simulations to large scale clinical testing in patients. By comparison, the subject of this thesis pertains to the rather small fringe of computational pattern formation.

The descriptive models of the heart present a multilevel hierarchy of causes and effects. The hierarchical division does not necessarily represent an essential difference in the system itself or its representations, but is a useful separation for the purpose of dividing the problem into smaller ones. At the top level we have the entire organ and its function as depicted in figure 1.2a. The organ is the heart and its function is to pump blood in response to the physical activity of the organism. There are higher levels still, in which the organ is only a part, but the heart is an almost autonomous unit — it receives information about the state of the organism it is in and regulates itself. Apart from the pacemaker region which more or less acts as a time-dependent boundary condition for the rest of the organ, it is reasonable to regard cardiac tissue as a completely autonomous system. Certain observables pertain to the organ as a whole. For example, the electrocardiogram (ECG) is the resultant effect of the action potential (AP) weighted over a large area through flesh and bone in a very specific manner[9]. We mention this here because it is often confused with the AP, which is an observable at the level of single cells or membranes. Even though both look like waves of excitation or pulses, they are usually very different.

[9]For instance, the position of the recording electrodes are fully specified by procedure. Different locations would result in a presumably mutated ECG, which would be difficult to interpret.

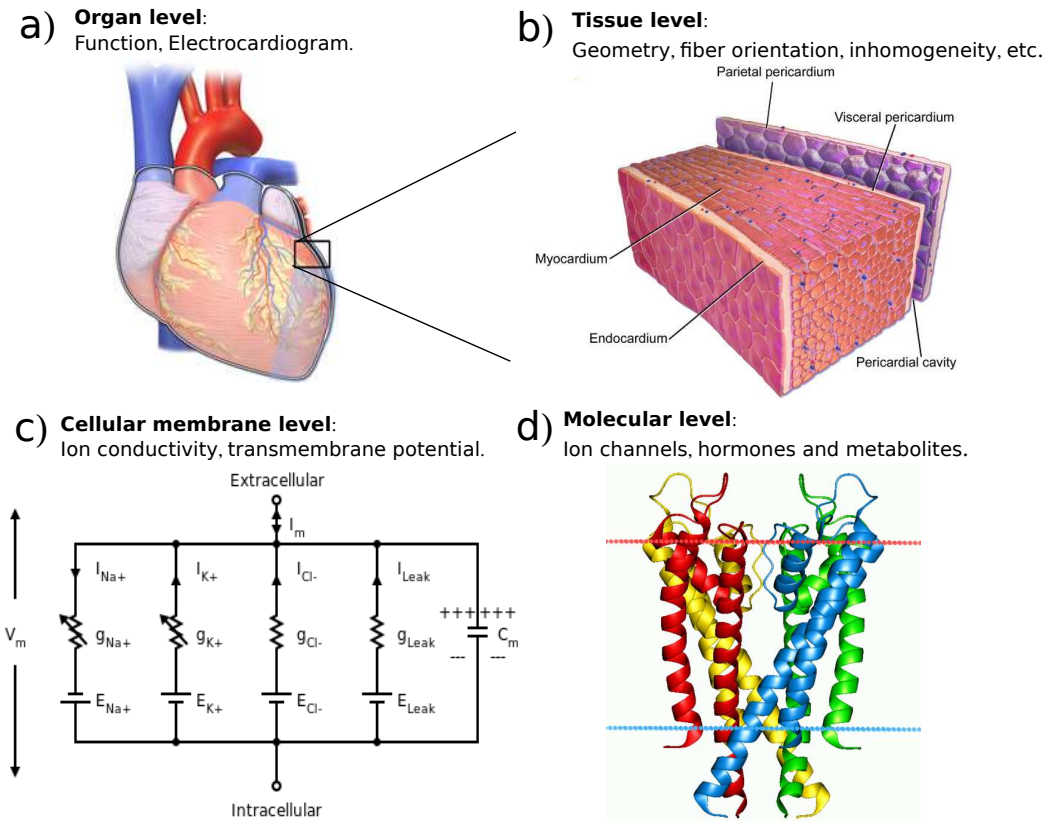

Figure 1.2: Multi level hierarchical structure of the heart. a) The whole organ (Bruce-Blaus [48]/ Wikipedia Commons/ CC BY 3.0). b) The ventricular wall is an excitable medium (*ibid*). c) The cellular membrane represented as an electrical circuit (Nrets/ Wikipedia Commons/ CC BY-SA 3.0). d) A single ion channel at the molecular level (Andrei Lomize/ Wikipedia Commons/ CC BY-SA 3.0). Complex patterns of activation are observed at the level of the whole organ or tissue, and supervene on the properties at the lower levels.

If we go down one level of organization we have the cardiac tissue (Figure 1.2b) which is for all intents and purposes an excitable medium i.e. a medium that actively responds to finite perturbations but is otherwise stable at the rest state. It has many physical properties that influence the propagation of nonlinear waves. First is its complex geometry. The heart is not a sphere and the many arteries and veins on the surface, as well as the interior's structure, wall thickness and other subsystems composed of cells of different kinds (e.g. Purkinje fibers — a sort of highway system for the AP with self oscillation capabilities) influence wave propagation. However, if we consider the ventricular wall itself, it is more

or less a thick slab of excitable tissue. Even so, the muscle fibers tend to orient in specific directions and are not simply stacked throughout the muscle layers but each muscle sheet is rotated with respect to one another. In addition, the excitations propagate about three times faster along these fibers than across [49, 50, 20]. All together, it means that the heart tissue is a highly anisotropic and inhomogeneous medium even in its healthy state. Even though the heart tissue is composed of discrete cells, for the purpose of simulating the whole tissue a continuum representation is often adequate for the observation of the basic phenomenology, which is what we do when we study pattern formation with a RD-like equation. All the information about the tissue anisotropy, inhomogeneity and cell coupling is then encoded in the diffusion tensor of the governing equation. The geometry plays an important role for the AP propagation in healthy conditions and during VF. It has been shown by surgical removal of layers of tissue that one could reach a volume (or thickness) in which VF could not be sustained, suggesting that VF is a purely 3D phenomenon [51, 50, 20]. Corroborating this evidence, it is known that small animals are less liable to VF and that a small heart can even naturally recover from VF to normal tachycardia (rapid heart beat) [51, Figure 1]. Furthermore, the critical size (thickness and/or volume depending on the case) of the system must certainly be a function of the wavelength of the pattern and this offers a mechanism of action for certain drugs at the level of the tissue — forcing a change in the factors that influence the wavelength changes the effective volume of the medium.

At an even lower level, we have the cellular membrane (of all these muscle fibers) and their properties as depicted in Figure 1.2c. Even a single cell membrane is already an excitable medium. However it is not the level that we usually want to study in the context of cardiac dynamics as a pattern forming system. Yet, the properties at this level are of course crucial to the properties of the tissue. When we talk of transmembrane potential, restitution curves and conduction velocity along the fibers, it is to these membrane's properties that we are referring. Of course some of these properties are averaged over many different instances so it might

be hard to say they represent any particular one. Models of the AP more or less describe this level of organization. Following the pioneering work of Hodgkin and Huxley [52], many other realistic models of the concentration of various electrolytes and voltages across various specific cell types have been designed that involve dozens of simultaneous ODEs [53, 54] and this is still an ongoing area of research [55]. Alternatively, simple conceptual models effectively average over all the individual contributions at this level to retain only the essential excitable behavior [56, 20].

Finally, at the lowest level that we will consider, the molecular level, we have the various ion channels, pumps and other metabolic mediators embedded in the cellular membranes and floating in the cellular medium (Figure 1.2d). Most active pharmaceutical agents have an effect at this level. For example, it is known that potassium channel blockers induce an increase in action potential duration (APD; the duration of the pulse). Other events in the body can induce effects at this level. For instance, lack of oxygen (due to clogging of the arteries) gradually reduces the excitability of the medium, which in turn has an effect on the pattern (or stability of the pattern). Therefore, mechanisms that act at this level cause changes at the higher levels. The relation of cause and effect is often not known precisely, and it is more useful to think of this relation in terms of supervenience [57] rather than in cause and effect i.e. the pattern and its properties supervene on the micro-properties of the membrane. Causes and effects act on the same level whereas supervenience merely means that a change at the higher level implies that there has been a change in the lower level. The opposite is not true: not all changes of the lower level properties produce a change in the properties that supervene them.

What do these levels of description tell us about the functioning of the organ? Certainly a fundamental understanding of the lowest level gives us better estimates of the parameters of the model or an *in silico* way to assess the effect of new compounds (an old idea of biochemical engineering which, in spite of enormous efforts, is still in its infancy). Putting all of this

together certainly helps to build very realistic models of cardiac tissue. The geometry of the tissue and the high anisotropy, which at the end of the day cannot be deduced independently from actual dissections, has been used to produce extraordinarily physiologically accurate models of particular hearts [58, 59, 60]. However, in spite of this tempting possibility, it also transpires that these complications are not always necessary for a description of the fundamental phenomenon of re-entry (autonomous re-excitation of the medium) and VF, since homogeneous and isotropic tissue models produce good representation, though very abstract, of the actual phenomena [51]. Likewise, as physicists, it is usually our understanding that overly realistic realizations only serve to obscure the fundamental abstract relations and laws that may apply. For instance, even homogeneous and isotropic models support symmetry broken patterns, which exposes the question of spontaneous symmetry breaking that occur through certain bifurcations. However, a realistic, highly inhomogeneous and anisotropic model in these cases would have only served to obscure this question since the dynamical systems would have been already very asymmetric. Fundamental electrochemical models of the cell membrane that are derived for the microscopic level do not specify how the model should extend to spatially extended systems. The addition of complications, and analysis of their effects, is therefore entirely left up to the kind of questions that require answering. This is very important because this is what offers us a great deal of autonomy (in the study of the pattern formation level) from that of other levels of description, in spite of the importance of *all* level of descriptions. In other words, we recognize that the specific details of the system are not important *only if* we are interested in abstract questions at the higher level of description.

Undoubtedly, patterns relate to function in the heart. Although it was mostly hypothetical at first, measurements *in vivo* demonstrated *a* correspondence between spontaneous re-entry (a single vortex) and tachycardia and multiple re-entry (mutiple vortices or DMT-like state) and VF, as shown in Figure 1.3. A similar association is shown in [27, p. 440] with

quasiperiodically meandering re-entry corresponding to torsade de pointe (a special form of tachycardia) and chaotic meandering re-entry corresponding to polymorphic tachycardia, a fancy term to say weird-looking rapid heartbeat. Mechanisms of fibrillation do not always require a critical thickness or multiple re-entry. It has also been shown that fibrillation-like ECG could be reproduced by a single irregularly meandering re-entrant wave [61]. Therefore, the correspondence we have illustrated may not be as clear cut as implied and is still the subject of active research. Doubtless there are multiple mechanisms responsible for the initiation and maintenance of VF [20, 62]. However, regardless of the actual mechanisms, all the states involved correspond to a certain ECG pattern which is, from the point of view of pattern formation, a very coarse representation of the state. Even so, the ECG is useful in its own right as an overall representation of the state and I'm certain wouldn't be replaced by a "real time" description of the pattern even if we could. The physician likely has no need for the pattern formation level apart from a few numbers just as the pattern formation scientist has no need for the molecular dynamics level apart from a few numbers. If we can eventually provide a useful contribution relevant to clinical medicine, it will probably have to be expressed in the language of ECG, not of pattern formation. Although that is not something we will consider in this thesis, this fact is already understood by those who consider physiologically accurate models of the heart and they produce synthetic ECG to show and correlate their results [60]. This is, all things considered, quite an amazing and elegant experimental pipeline!

The discussion of levels of description, cause and effects and supervenience of the pattern properties also serves to put into context two existing popular approaches used for treating cardiac arrhythmias. In the language of dynamical systems, the first involves changing the control parameters of the system whereas the second involves modifying the dynamical equation for a short time in the hope that, in returning to the original dynamics, we would have perturbed the state of the system in such a way that it wouldn't return immediately

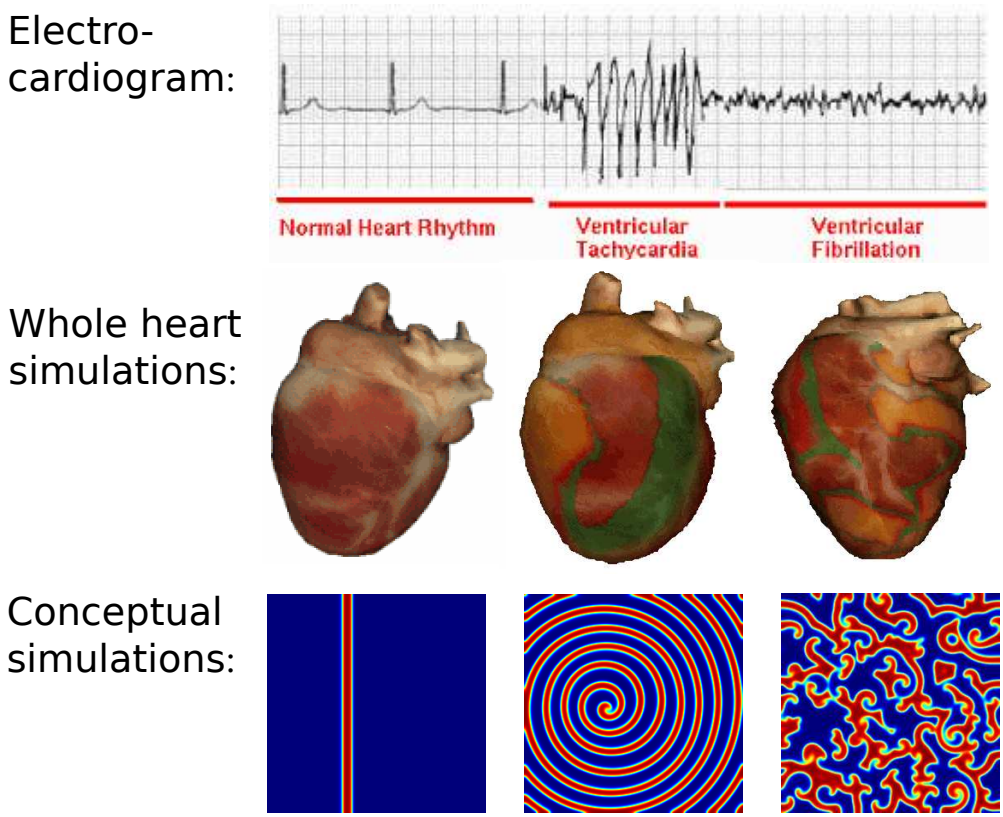

Figure 1.3: Patterns are intimately linked to functions. From left to right, normal heart activity characterized by its ECG which corresponds to coherent excitation pulses. Re-entrant activity in the form of a spiral wave on the ventricular wall corresponding to fast re-activation or tachycardia. Finally, multiple re-entry or spiral wave turbulence characterized by an incoherent ECG that does not achieve large amplitude pulses that would be required for any pumping action. The superimposed colors correspond to different states of depolarization (transmembrane voltage) of the tissue/medium. (Adapted from Ref. [63] in accordance with NJPs CC BY 3.0 licence).

to the turbulent state associated with the absence of useful function.

The first method involves finding factors that increase the stability of the pattern, and by tweaking these factors using pharmaceutical agents, we may at least prevent degeneration to arrhythmia in certain individual [64]. For example, we mentioned that potassium channel blockers induce an increase in APD, which in turn reduces the diastolic interval (DI, the time between two pulses) such that reentrant activity is less likely to excite the medium between two normal activations. However, many of these medications have multiple mechanisms of action and usually many side effects. In addition, the constant intake of medication is a

source of annoyance and decreases the overall quality of life of the patient.

The second method, in contrast, consists in dealing with the aftermath i.e. control of turbulence after its onset. How can we effectively bring back the system to a more ordered state? The conventional method involves resetting the whole medium with a large excitation pulse produced by a defibrillator. Defibrillators are not always successful and are very painful. A more direct, but invasive, approach to patients at risk involves subcutaneous defibrillators. By being placed closer to the tissue they can afford a smaller voltage to produce the same effect. However, this requires expensive surgery and is only used in the most extreme cases. It has also been shown that, at least in theory, many smaller shocks at a specific frequency can have the same resetting effect as a larger single shock [65, 66]. Recently, such a method, called low-energy anti-fibrillation pacing (LEAP), has been tested *in vitro* and *in vivo* and found to effectively terminate atrial fibrillation (AF) for artificially induced AF in canine heart [67]. However, the experimental setup still appears to be very invasive but could eventually provide a less painful alternative to the one-shock defibrillation. In short, the known approaches involve either controlling the parameter space or controlling the pattern. In both cases, understanding of the pattern forming system level, and of the fundamental factors governing the pattern, is a key element.

These two methods are not mutually exclusive. Patients under preventive treatment may still go into cardiac fibrillation and defibrillation is not 100% effective and sometimes needs to be coupled with the direct use of pharmaceuticals to increase the effectiveness of defibrillation. Furthermore, not all gains are additive and reduction of the risk of a certain mechanism may very well enhance another [20]. All in all, a better understanding of all levels is needed for the elucidation of the complex interplay between the different treatment methods and their effects at every level. The pattern forming system is the lowest level in which both methods can be discussed comparatively and as such, the properties of the pattern and its complex parameter space need to be understood as precisely as possible for

an optimal realization of treatments.

This brief overview of a real-world system should have provided a reasonable perspective of the complications and contingencies involved in these phenomena. The literature on the subject is vast and many works have focused on the description of defects and filaments in relatively complex models, which preclude[10] a statistical description (see for example [58, 59, 21, 55]). Furthermore, many of these works consider defects and filaments only as a shorthand description for the state [68, 58], without considering what is captured, or can be captured, by such a description. This does not mean that they can't identify any generic features, but they are far more likely to detect idiosyncrasies of the models. Also, as we have stated, only a statistical description can be meaningful when comparing complex turbulent states (even if we are unsure *how*) and it appears that simplifications are essential to make progress in the factors that influence DMT.

1.5.2 General questions

We have given an overview of the complications involved in a real-world system. One can spend an entire lifetime working on very specific aspects of a complex system like the heart. Likewise, a plethora of papers can be found regarding seemingly minuscule details on the mechanism of some complex chemical reaction or on the mechanism of action of an enzyme in a cell. However, the apparent genericity of the phenomena these systems exhibit and the existence of normal forms[11] in some cases offers us some hopes of the existence of a *universal* description that does not depend on the enormous amount of complexities and contingencies of the real systems. Therefore, even though the questions themselves can be seen as motivated by the real-world phenomenon of the heart dynamics, they are also reformulated in a much broader context to encompass any defect mediated turbulence in a large variety of media.

[10] At the present time

[11] Normal forms are the universal limiting behavior close to certain transitions.

The role of instabilities

Any sufficiently complex dynamics can show multiple types of instabilities of simple wave and spiral patterns. When these instabilities lead to a breakup of the regular structures, they may be referred to as breakup mechanisms. Breakup mechanisms of spirals in 2D fall into at least two broad phenomenological classes: Breakup close to the spiral core (Figure 1.4a) and breakup in the far field (Figure 1.4b). The relation between this coarse classification and the details of the instability is certainly a complex one. For instance, instabilities of wavetrain can travel forward (in the direction of emitted waves) or backward (toward the core) leading to far-field and core breakup respectively. Conversely, meandering core instability might break the spiral at the core or the Doppler shift effect[12] on the emitted wave could induce breakup in the far-field [69]. The initial breakup usually doesn't completely destroy the pattern and local patterns remain. In such cases, the local patterns grow only to the extent they are allowed to without breaking up again in an endless sequence of breakup and the turbulence often appears as a competition between stabilizing and destabilizing effects. How does the breakup mechanism influence the characteristics of the observed turbulence in such a case? Does the breakup mechanism matter or only the existence of opposing stabilizing/destabilizing effects? And what about far from onset once the breakup of local structure is more complete? Is the breakdown of structure a continuous process as characterized by the statistical measures of defects? These questions can be addressed in any phenomenological model where breakup occurs.

The previous phenomenological description applies for breakup in any medium since core and far-field is only specified relative to the existing patterns, and the patterns are common to many media types. In addition to the instabilities of patterns, many simple bifurcations of the local dynamics can induce change (hence produce instabilities) in the patterns[13] and eventually may lead to breakup. These bifurcations of the local dynamics can readily be

[12]The emitted waves of a meandering spiral are compressed in the direction of motion of the core and longer when the core is moving away to the direction of travel of the waves.

[13]It's not something impossible for excitable media, but it is certainly more uncommon

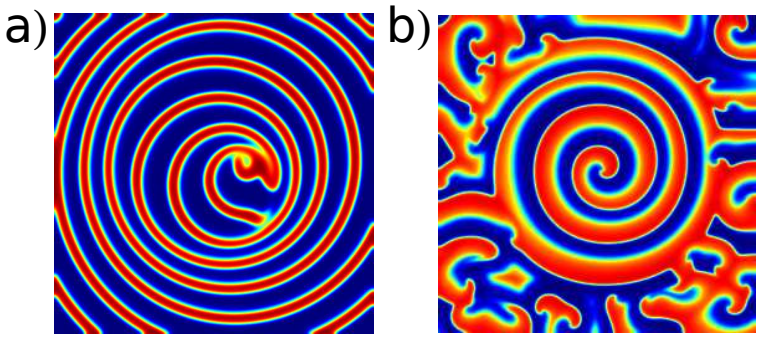

Figure 1.4: Phenomenology of spiral breakup in two excitable media. a) In a core breakup in the Bär model presented in Section 3.3.4, the initial wave break occurs close to the center of the unstable spiral and the disturbance propagates outward to rapidly invade the whole pattern. b) By comparison, far-field breakup manifests far from the center and the encroaching turbulence propagates inward. In this example, the far-field instability results from the alternans instability in the Karma model of Section 4.3.3.

observed in the simplest case of well-stirred chemical system (where the diffusion is rendered negligible due to active mixing). However, in the non-stirred case, the resulting effect on the spatially extended patterns can be non-trivial. For instance, the Willamowski-Rössler (WR) system of equations is known to be able to produce simple oscillations that lead to chaos following an infinite period doubling sequence of bifurcations [35][14]. Spatially extended media versions of this route have been investigated and the properties of the patterns follow a similar sequence of bifurcations although it has been noted that the onset of STC occurs after a finite sequence of period doubling [70, p. 281]. In the STC state, a similar sequence is also observed from the spiral core through synchronization defect lines (SDLs) [71] which is consistent with the interpretation of defects as remnants of previous symmetries. The STC state resulting has been found to be of two kinds: one characterized by the appearance and chaotic motion of SDLs of various periodicity [46] that collide and recombine according to specific topological rules in a regime of phase turbulence (i.e. no phase defect creation) while the other, still driven by the presence of SDLs, leads to the creation and annihilation

[14]This period doubling sequence in low-dimensional systems is one of the few generic "routes" to chaos and possesses some universal scaling properties that are common to any such route, in any system, no matter the details of composition [2, p. 372].

of new topological phase defects as the endpoints of these lines [72], and can therefore also be characterized as DMT. However, in both cases, it appears that the non-trivial description is found in the field (as characterized by the SDLs) whereas the topological phase defects behave as randomly independent entities, like in the simple oscillatory case with the exception of some non-trivial correlations in the time series of defects [35].

What about other generic low-dimensional routes to chaos like quasiperiodicity which, unlike period doubling, involves only a finite sequence of bifurcation to chaos? How does the breakup occur in such a case and is the DMT generated by such a mechanism also satisfying a similar description? Let us call *instability-driven defect mediated turbulence* (IDDMT) the idea of the influence of the instability on the breakup mechanism and that of the breakup mechanism on the statistical features of DMT. In the strong form, IDDMT would imply that every instability has a direct influence of some observable properties of DMT. In its weaker form, only the class of breakup mechanisms would influence the observable properties of DMT. Does IDDMT apply in one form or another?

The role of the dimension of the system

The case of VF in the heart is without a doubt the driving factor behind most of the research on the new[15] 3D instabilities of scroll waves. It has been recognized very early that the prediction of negative line tension (NLT) of filaments of scroll waves [73, 74], by which filaments destabilize like compressed rubber bands, implies the existence of a purely 3D spatiotemporally chaotic regime (Winfree turbulence) unless another nonlinear effect stabilizes the growing filaments [74]. Furthermore, the conspicuous circumstances of a minimum volume for VF, and the absence of 2D spatiotemporal chaos in many realistic models of cardiac dynamics have led to the idea that VF must be a fundamentally 3D phenomenon as well. According to the IDDMT, such a fundamentally different mechanism of breakup could be expected to produce a very different turbulent state and indeed it does [43]. On the other hand,

[15]New with respect to the literature on 1D and 2D instabilities

as we have previously mentioned, there remain many alternatives to a purely 3D breakup mechanism in the case of the heart. Strangely though, there is a surprising lack of numerical data regarding what to expect when the various 2D turbulent regimes are extended to three dimensions and so we echo a previous suggestion that "for AW [excitable] media, [...] some types of instabilities are possible in 2-D. It would be interesting to compare properties of these different instabilities and chaos generated by them, to see if the 3-D AW turbulence is also much more complicated than the 2-D one" [75]. The suggestion that the 3D turbulence generated by a 2D mechanism would be more complex could be called *dimension dependent defect turbulence* (DDDT).

To test DDDT, one would need a way to compare the statistical features of 2D and 3D turbulence on the same level. As motivated by the study of the heart dynamics where 3D observations are especially difficult, we are also led to consider the special case of surface turbulence in 3D media i.e. only the 2D DMT visible from the surface. This is not a fundamental limitation in general however and many observations of the complete filament dynamics have been made using tomographic techniques in the BZ reaction [76, 77]. However, such methods are impractical or would be too invasive in the case of the heart. This leads to the general problem of considering only the surface observable of 3D turbulence, which at the same time provides a common set of observables to qualify and quantify the turbulent dynamics between 2D and 3D simulations.

Finally, in relation to the falsifiability of competing models in the case of VF, apparent spatiotemporal chaos and multiple re-entrant waves can be reproduced with much simpler 2D models (simpler than their 3D counterparts). However, such models would appear completely useless to account for the experimental observation of wall-thinning that were discussed and which would seem to require at least a full 3D representation. What about other regimes? Is a full 3D perspective always required and can we tell when it is and isn't? Are there other observables that may be conducive to distinguishing experimentally certain turbulent

states from others? This line of inquiry links back to the previous IDDMT hypothesis, now extended to 3D mechanisms.

Distinguishability, phase transitions and scaling laws

A tantalizing question regards the existence of nonequilibrium phase transition. Many of the properties of phase defects in DMT appear to behave in a manner qualitatively analogous to those of particles at a phase transition. For instance, a multi-defect "solid" state in the region of spiral stability becomes an unstable spiral "liquid" dominated by rotational modes where defects meander while retaining some crystalline structure (like water retains many H-bonds in the liquid phase). This latter state, in turn (in a turbulence transition), becomes analogous to a spiral "gas" dominated by translational modes of defects where short range interactions (collision of defects) are much more frequent and dominate the turbulence [78]. However, in this case, no one has yet been able to provide a satisfactory analogous description to the common power law behavior of the order parameter at the transition point found in equilibrium phase transitions and the comparison remains superficial. Likewise, many characteristic features of DMT states appear to behave as power laws like one would observe for the correlation function close to the critical value of a control parameter in equilibrium transitions. This suggests a description of DMT in terms of universality classes, but no one has been able to make the formal connection and experimental observations are still very scarce.

One nonequilibrium phase transition was found to occur at the onset of SDL turbulence [79]. It has been observed that the average total SDL length in the medium appears to behave as an order parameter satisfying power law scaling behavior close to the onset of two such instabilities, like in a continuous phase transition. In this case, the power law close to onset was found to have different critical exponents depending on the regime [79]. However, SDLs are an observable limited only to the particular period doubling dynamics. Are there more general defect observables that would act as an order parameter and indicate the onset

of a nonequilibrium phase transition in the case of DMT?

Perhaps the most novel non-equilibrium transition involving defects is the defect unbinding transition, wherein the distribution of spacetime loops of defects in 2D decay exponentially on one side of the transition, and as a power law on the other side [80, 81]. Again, in this case, the analogy is partial and it is only the statistical description of the state that scales in a seemingly universal way [45], not the *connection* between states close to the transition point i.e. no order parameter was found that generically satisfied a relation like $\mathcal{O} \propto |\lambda - \lambda_c|^{-\eta}$ where λ_c is a critical value of the control parameter λ and η is the critical exponent describing the order parameter $\mathcal{O}$ at onset of the transition.

In any case, the idea of nonequilibrium phase transitions underlies the possibility of distinguishability of different turbulent states. The idiosyncrasies of the particular systems and parameter regimes may, at face value, distinguish different turbulent regimes or different mechanisms [82] but, without well-defined transitions, may also turn out to be part of a continuum of descriptions. Distinguishability demands that the set of observables that characterize the state be generic i.e. apply to all such state and unique i.e. must be at least qualitatively different from any other state. In equilibrium phase transition, the order parameter is zero on one side, and finite on the other, thereby distinguishing the two phases.

1.5.3 Simplifications

The previous questions are quite general and their formulations and elucidations will necessarily demand a statistical description. Also, the widest applicability (universality) demands higher abstractions. We therefore, as a rule, strive for the largest abstraction possible while still maintaining an experimental (numerical) approach due to the roadblocks facing realistic models and analytical methods. Here is a short list of the simplifications we shall use for our investigation and that were implicitly assumed in the formulation of the previous questions:

1. *Paradigmatic models.* We are interested in certain types of instabilities and

spiral breakup mechanisms, not necessarily in specific models of cardiac electrophysiology. We therefore extend our line of inquiry to oscillatory, excitable and bistable media. Whenever possible, we want to study normal forms of the dynamics.

2. *Homogeneity.* Unlike realistic models, we only consider homogeneous systems. In the case of the heart dynamics, inhomogeneities are certainly a prevalent cause of breakup, but such breakup would be non-generic. We are only interested in genuine self-sustained dynamics.

3. *Isotropy.* We shall only consider isotropic medium. The effects of anisotropy are two-fold: they accentuate previous instabilities [83] and they can induce new instabilities [49]. Both effects can be ignored on first analysis.

4. *Simple geometry.* We only consider simple geometry: cube, slab, sheet. The finite size effects are more easily accounted in such simple geometry. Realistic models of the heart often have many nooks that sustain complex "anatomical" re-entry [49], which again, complicate the solution in a non-generic manner.

5. *Simple boundary conditions.* We considered only two type of BCs: No-flux and periodic as limiting cases. This is, of course, quite unrealistic especially considering the complex electrophysiological conditions surrounding the heart.

6. *Noise-free.* We did not simulate the effect of experimental noise and imperfect measurements.

These simplifications implicitly direct the type of questions we can hope to tackle, while other questions are necessarily out of bounds. For instance, we cannot ask about the effect of lower extracellular potassium concentration because our conceptual models will likely not know what potassium is. However, we can ask what happens in regimes of lower and higher

excitability because this broad classification of regimes is something that exists in both the realistic and the conceptual models of excitable media. Likewise, we cannot, or it would be pointless to, produce a synthetic ECG of a cube or a slab system but we can easily assess the effect of the system size in the thermodynamic limit and so on. To paraphrase, the format of the analysis constrains the type of questions it can answer.

1.6 Structure of the thesis

Chapter 2 will be dedicated to the question of how to characterize the DMT states by focusing on its singular defect points/loci. We will review previous methods and develop new improved ones. The exploration of the methods shall reveal some difficulties that had been overlooked by previous attempts, and which we endeavored to correct. Although the precise details of these numerical methods have not been part of a separate publication, they have been used extensively in our two published works [36, 84] and in another related work [28].

Chapter 3 will be focused on the investigation of various DMT regimes in 2-dimensional media and to the transition between qualitatively different turbulent regimes. We shall first review our work on DMT in a locally quasiperiodic biochemical RD model which appears to support the universality of the simple statistical description of defects. However, like in other cases, the behavior of defects is nonetheless marked by non-trivial correlations. Then, we shall expand on the idea of IDDMT with other instabilities of oscillatory and excitable media.

In Chapter 4, we will turn our attention to 3D media. We shall present the results of our recently submitted publication [84], which is the first attempt at a quantitative statistical description of the transition of DMT between 2D and 3D media. The remainder of the chapter is focused on the characterization of other 3-dimensional instability-driven turbulence which substantiate the previous findings.

Finally, in Chapter 5, we shall consider how our previous results reflect on the problem of distinguishability of turbulence generated from 2D and 3D mechanisms, and the related problem of the distinguishability from surface observables alone. We will conclude with our current prospects and perspectives regarding the applicability of our results in the case of the heart dynamics.

Chapter 2

Characterization of DMT

In this chapter, we introduce various methods to detect and track topological phase defects in 2D and 3D media. Even though these numerical methods have been used directly in two published papers [36, 84], they will be described in detail here for the first time.

2.1 Definitions

We have seen that defects are singular points or loci of points where the local description of a pattern cannot be applied. The nature of the description determines the type of defects. Since we will be exclusively concerned with periodic, quasiperiodic and chaotic phenomena involving oscillations, we will be only interested in phase defects i.e. points or loci where the phase of the oscillation cannot be ascribed.

2.1.1 From state to phase

Any periodic, or periodic-like, dynamical behavior of a phase space trajectory can be replaced by a phase description. However, a phase description introduces an essential singularity in the description which corresponds to zero amplitude oscillations. The region of phase space (which is the same as the state space for a set of first-order ODEs) corresponding to these oscillations is known as the phaseless set. We read that

> [...] in a two-dimensional state space the phaseless set is at least an attracting or repelling steady-state point and that in a three-dimensional state space the phaseless set is at least an extension of that point into a one-dimensional curve. This curve consists of the two trajectories leading toward or away from the

steady-state. This phaseless set is the convergence point for all the isochrons, arranged in order around the cycle. [13, p. 166, par. 3]

This is illustrated in Figure 2.1.

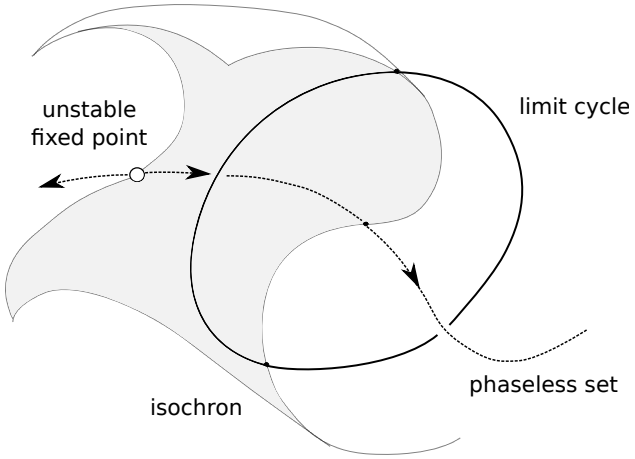

Figure 2.1: The phaseless set, isochrons, fixed point and limit cycle in a typical ODE of dimension larger than two. If we use the fixed point in this projection as our center of rotation to define a phase, oscillations won't register as an increase in phase by a factor 2π as they should. However, there is a point (or many) on the phaseless set that would be an appropriate center.

Therefore, a phase can be defined as[1][2]

$$\phi = \tan^{-1} \frac{b(\vec{A}) - b_0}{a(\vec{A}) - a_0}, \tag{2.1}$$

where $a(\vec{A})$ and $b(\vec{A})$ are two coordinates in a suitable projection of the limit cycle traced by $\vec{A}$ (the state of the uniform system in this case) and a_0 and b_0 are ideally the intersections of the phaseless set with this projection. There can, however, generally be more than one reasonable choice for this center. Luckily, the precise value does not matter and any reasonable[3] choice would do. From this, and for a periodic attractor with monotonically (but irregularly)

[1]There is an infinity of equivalent phase maps but not all of them are desirable.

[2]Most mathematical libraries contain a version of $\tan^{-1}$ that use 2 parameters. This enables the evaluation of the quadrant and to extend the support of the function to $[-\pi, \pi[$ or $[0, 2\pi[$ depending on the implementation.

[3]As long as the phase thereby defined advance by 2π every oscillation.

increasing phase, a unique phase with $\dot{\theta} = \omega_0$, where ω_0 is the angular frequency of the oscillation, can be defined with a change of variable (see for example Ref. [85, p. 177])

$$\theta(\phi) = \omega_0 \int_0^{\phi} \dot{\phi}(\phi')^{-1} d\phi'. \tag{2.2}$$

The isochrons in Figure 2.1 are defined as the loci of all points $(a, b, \dots)$ such that

$$\lim_{n\to\infty} \theta(a(nT), b(nT)) = \theta(a_C, b_C), \tag{2.3}$$

where T is the period of the limit cycle and $(a_C, b_C, \dots)$ is a point on the limit cycle that can be mapped into a single phase θ through the relation 2.1 and 2.2. For any value of the phase θ, these points form $D-1$ dimensional hypersurfaces, called isochrons, that intersect the stable (or unstable) limit cycles as represented on Figure 2.1. Therefore, Eq. 2.3 implies that two points with phase θ_1 and θ_2 will always have $\Delta\theta = \theta_2 - \theta_1$, even as they both converge toward (or away from) the limit cycle due to the dissipation. Note that, in general, two points $(a_1, b_1, \dots)$ and $(a_2, b_2, \dots)$ on the same isochron would not satisfy $\phi(a_1, b_1) = \phi(a_2, b_2)$ since being on a isochron is a property that requires the whole dynamics, not only the coordinates of the point.

Identification of a proper phase center can be quite problematic in some cases and some work has been invested into automated phase attribution methods [86]. For our cases however, we found that it is usually sufficient to consider the velocity field such that

$$\phi = \tan^{-1} \frac{\dot{b}}{\dot{a}} \tag{2.4}$$

because all our oscillations (in the (a, b) projection) were unimodal. The center is then always simply $(\dot{a}_0, \dot{b}_0) = (0, 0)$, independent of the particular features of the system which is greatly advantageous when exploring the parameter space of a system. Such a phase definition had been suggested in a different context for the same reasons [87].

2.1.2 Phase defects in 2D

In spatially extended systems, the phase field $\phi(\vec{r},t)$ describes the local phase of oscillation of a set of oscillating fields $\vec{A}(\vec{r},t)$. However, the topology of the phase field is, in general, riddled with topological phase defects due to the singularity in the phase definition. These topological defects are defined by the non-zero closed line integral of the phase gradient a.k.a winding number (e.g. [27, p. 160] and [86, 88])

$$q = \frac{1}{2\pi}\oint_C \vec{\nabla}\phi \cdot d\vec{l}, \tag{2.5}$$

such that a spatial region bounded by the contour C is said to have topological charge q, where q is an integer value. In the limit where the contour shrinks to a point and the non-zero value remains, we deduce that there must be a single topological defect at that point with the charge given by q.

Let's consider the case of an archimedean spiral, the spiral pattern that we encounter frequently in 2D pattern forming systems. A static spiral solution can be written as

$$\vec{A}(r,\theta) = \vec{F}\left(\frac{2\pi r}{\lambda} + \theta\right) \tag{2.6}$$

where $\vec{F}$ is a vector of periodic function that set the relative phase, magnitude and form of the field components and λ is the wavelength. The phase of the pattern is also described by a similar relation such that

$$\phi(r,\theta) = f\left(\frac{2\pi r}{\lambda} + \theta\right) \tag{2.7}$$

where $f(x)$ is a mod(2π)-periodic function of its argument. Replacing in Eq. 2.5 with a contour integral surrounding the center of the spiral, we have

$$q = \frac{1}{2\pi}\oint_C \vec{\nabla}\phi \cdot d\vec{l} = \frac{1}{2\pi}\int_0^{2\pi} f'\left[\frac{2\pi}{\lambda}\hat{r} + \frac{1}{r}\hat{\theta}\right]\cdot r d\theta\hat{\theta} \tag{2.8}$$

$$= \frac{1}{2\pi}\int_0^{2\pi} f' d\theta = \frac{1}{2\pi} f|_{\theta=0}^{\theta=2\pi} = 1. \tag{2.9}$$

Hence it shows that we have a topological defect of the phase field in the center of our spiral pattern. Furthermore, this defect is the result of the mathematical singularity of the polar

system of coordinates and this coordinate system was adequate to our problem because of the (discrete) rotational symmetries of this pattern. This defect is essential to the description and organizes the regular pattern in the sense that it is necessarily surrounded by all phases. Such a phase defect can also adequately be referred to as a *vortex*. Keeping the same contour but using a spiral pattern that rotates in the opposite direction would have revealed a defect of opposite charge. Therefore, the sign of the defect specifies the direction of rotation of the surrounding spiral vortex. Topological charges greater than one are possible, though they are not found in the many regimes that we will explore[4], and indicate the presence of multi-armed spirals or multiple spirals of lesser charges within the same contour (e.g. bound pair).

Given the phase definition 2.1, one can easily see that the isolines of the fields[5] $a(\vec{r})$ and $b(\vec{r})$ evaluated at a_0 and b_0 would only intersect at points where the phase cannot be defined (point of zero amplitude oscillations). This provides an alternative representation of the defects, as well as a simple way to deduce the law of creation and annihilation of phase defects since isolines (lines of equal value of the field) of a smooth field can only terminate at the boundary or form closed loops. Therefore, new intersections of the isolines $a(\vec{r}) = a_0$ and $b(\vec{r}) = b_0$ in the bulk would necessarily involve the creation of a pair of counter-rotating vortices. Likewise, annihilation of vortices can also only occur pairwise for the same reason.

Another straightforward property is the null total topological defect charge in any periodic system. Since isolines can only trace closed curves in such an instances, any intersection of $a = a_0$ with $b = b_0$ must necessarily have another intersection to return to the original side as demanded by the closure of all isoline curves. It therefore follows that to every defect there must be an oppositely charged one such that the total topological defect charge in periodic systems is always zero. In the case of no-flux boundary conditions, isolines are not necessarily closed curves and can terminate at the boundary. In this case, only the average

[4]In the CGLE, it can be shown that only single-armed spirals are stable [89]. In other systems, it is only an empirical observation and not impossible *a priori*.

[5]At one particular time.

number of positive and negative phase defects are generally equal, and any instantaneous picture may reveal more of one than the other.

2.1.3 Phase defects in 3D

In 3D media, phase defects form spatial curves called filaments that are the continuation of the 2D surface defects. Just as surface vortices have a direction of rotation (charge), filaments have an orientation which dictates the direction of rotation of the surrounding scroll wave. The continuity of the filaments directly follows from the smoothness of the field and properties of the isosurfaces (the extension of the previous isolines to 3D). The intersection of two isosurfaces is guaranteed to form a continuous curve that is either closed (loop) or ends at the boundary of the medium. The previous topological constraints to the creation and annihilation of phase defects imply that the filaments have a much richer way of being created and annihilated. Filaments can be created and annihilated far from any other filament when the two isosurfaces just collided at a new location. Filaments can also split, merge and recombine which makes them much more difficult to identify and track. Section 2.3 will develop in more details how the various filament events can be detected.

2.2 Numerical methods in 2D

2.2.1 Defect detection

Figure 2.2 shows various representations of a state of a system in a regime of DMT which suggest various methods for the practical identification of defects. We first present a version of the *phase* method which relies on computing discrete phase gradients along fundamental contours. The procedure goes as follows: First, we calculate a phase everywhere based on the local value of the field $\vec{A}(\vec{r}) = (A_1(\vec{r}), A_2(\vec{r}), \dots)$. Then, we evaluate all the discrete gradient elements along a fundamental contour counterclockwise. If any of these gradients is larger than π, add one to the phase jump count, if it is smaller than $-\pi$, remove one

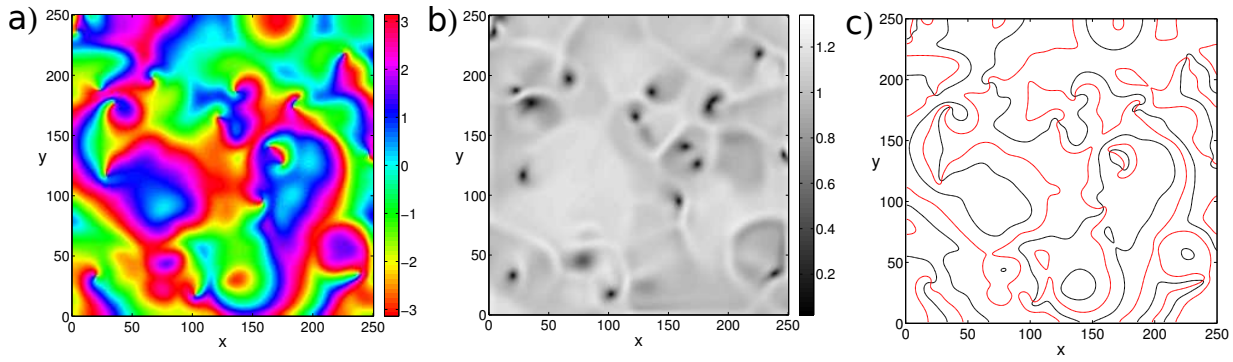

Figure 2.2: Three partial representations of the 2D numerical solution. a) A phase is attributed to every point in the medium. Defects are singular point surrounded by all phases. b) We can define the amplitude of the local oscillations. Defects are located at points where the amplitude tends toward zero. c) Isoline representation of the field. The red and black lines are isolines of two of the field components at a certain "central" value. Each lines map to two phases for unimodal oscillations. Defects correspond to the intersection of these isolines. This is our method of choice.

from the phase jump count. Once the contour is completed, if the final phase jump count is non-zero, we deduce that there is a topological defect inside the contour with the topological charge equal to its phase jump count. Optionally, one can evaluate the position of the defect to a sublattice precision using the fact that defects also correspond to zeros of the amplitude $R^2 = (a - a_0)^2 + (b - b_0)^2$. Otherwise the position of the defect is assumed to be known up to the lattice resolution only. This method is especially easy to implement. However, its main inconvenience is that the $\tan^{-1}$ function invoked to evaluate the phase is a rather computationally costly operation and it needs to be computed for the whole field. Also, one can only ascribe one defect per fundamental surface element in a discretized medium. Therefore there is a lower limit to the separation of a pair of defects given by the precision of the position of the defects.

The second method that we employed, the *bilinear* interpolation method, is much more elegant. The bilinear interpolation of a function f inside a unit square is given by

$$f(x, y) = (1 - y)\left[(1 - x)f_{(0,0)} + xf_{(1,0)}\right] + y\left[(1 - x)f_{(0,1)} + xf_{(1,1)}\right] \tag{2.10}$$

where $f_{(i,j)}$ is the function evaluated at the corresponding corners and $x \in [0, 1]$ and $y \in [0, 1]$

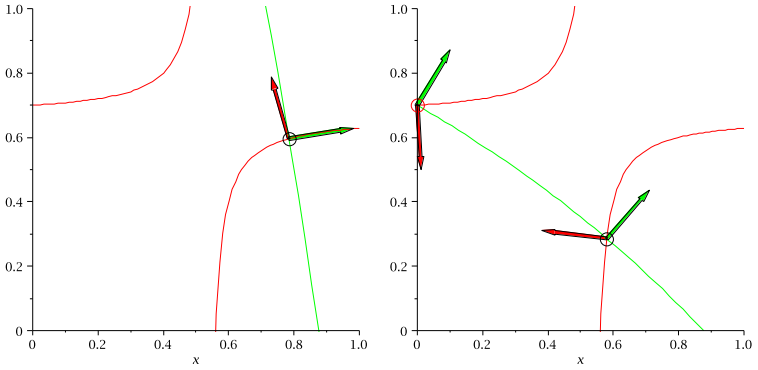

Figure 2.3: Bilinear interpolation of isolines. Given the numerical lattice data, one needs to interpolate the isolines to identify the positions of the defects at a sublattice level. The interpolation method is bilinear and produce perfectly consistent results. However, one must always remember that this precision is somewhat artificial and has an inherent uncertainty due to the choice of isolines and interpolation method. Bilinear interpolation of a single square surface element always yields either a) one, b) two or no defects if there are no intersections.

are the coordinates at which to estimate the value of the function inside one lattice unit. According to this interpolation, we are looking for the intersection of isolines that are solution of the algebraic system of equations

$$a(x, y) = a_0, \qquad b(x, y) = b_0 \tag{2.11}$$

If a solution (x_q, y_q) exists inside the area constrained by $0 \leq x_q < 1$ and $0 \leq y_q < 1$, then there is a defect at that position with a yet unspecified topological charge. Notice that this method, like all methods that are known to this author, requires finding an appropriate center of rotation (the same as before), although no explicit definition of the phase is needed in this case. Also, notice that this system of equations can have at most two solutions, therefore two topological charges can be ascribed to every surface element. Two such example solutions are shown in Figure 2.3.

The previous system of equation can be easily solved and we have

$$y_q = \frac{\Delta a_c - x_q \Delta a_{10}}{\Delta a_{01} - x_q \nabla a_{11}} = \frac{\Delta b_c - x_q \Delta b_{10}}{\Delta b_{01} - x_q \nabla b_{11}}, \tag{2.12}$$

where $\Delta f_c = f_c - f_{00}$, $\Delta f_{01} = f_{01} - f_{00}$, $\Delta f_{10} = f_{10} - f_{00}$ and $\nabla f_{11} = f_{11} - f_{10} - f_{01} + f_{00}$.

Solving for x_q we find the two roots are given by the standard quadratic equation solution $x_q = \frac{-b \pm \left(b^2 - 4ac\right)^{1/2}}{2a}$ where

$$\begin{aligned} a &= \Delta b_{10} \nabla a_{11} - \Delta a_{10} \nabla b_{11} \\ b &= \Delta a_c \nabla b_{11} - \Delta b_c \nabla a_{11} + \Delta a_{01} \Delta b_{10} - \Delta b_{01} \Delta a_{10} \\ c &= \Delta a_c \Delta b_{01} - \Delta b_c \Delta a_{01} \end{aligned} \tag{2.13}$$

Finally, it can be shown that the sign of the charge can be calculated by evaluating the cross product of the gradients of the two fields (Eq. 2.15):

$$\begin{aligned} \frac{\partial f}{\partial x}|_{(x_q, y_q)} &= \Delta f_{10} + y_q \nabla f_{11} \\ \frac{\partial f}{\partial y}|_{(x_q, y_q)} &= \Delta f_{01} + x_q \nabla f_{11} \end{aligned} \tag{2.14}$$

It is then a simple matter of consistency with the previous method (and/or with the direction of the rotation of the spiral around the defect) whether a positive result corresponds to a positive charge or a negative one. Accordingly, the charge at each point is

$$q = \text{sign} \left(\frac{\partial a}{\partial x} \frac{\partial b}{\partial y} - \frac{\partial a}{\partial y} \frac{\partial b}{\partial x} \right) |_{(x_q, y_q)}. \tag{2.15}$$

An additional benefit of this method is that we can use any of the calculated gradients as a representation of the phase θ (a different phase this time) of the pseudo-rigid spiral around its defect. For a single spiral, we would expect this phase to increase with a constant rate $\dot{\theta} = 2\pi/T$, where T is the period of rotation, whereas many interacting spirals might perturb their periods and their local rates of rotation. It can therefore be used to monitor how the interaction affects the rotation of a vortex and, even more interestingly, how the interaction affects the phase twist and other geometric factors of the filaments in 3D media.

2.2.2 Defect tracking and identification of events

We developed a new recursive tracking method based on intuition and similar ideas as described in Ref. [81]. Given that we have the positions of all defects at time t and $t + 1$

respectively, we identify defects from t to $t+1$ according to the maximum likelihood given by spatial proximity. However, it is important to recognize that even though a particular defect may be closest to another, the opposite may very well not be true. Therefore, we do not want to link two defects too soon without considering what is best for both parties. In fact, a global optimized solution would probably be the best but would be too computationally costly in many cases, so we need a solution that offers a compromise between speed and an optimal solution. We also need to take into consideration the possible annihilation, creation, leaving and entering of new defects. All these cases are events that cannot be identified from a frame at t to one at $t+1$ — they correspond to defects that were present at time t and vanished from frame $t+1$ or vice-versa. Furthermore, these events need to be identified positively. A positive identification means that we need to form a criterion to detect when these events occur instead of identifying these events as everything that is not a continuation from t to $t+1$, which would be a negative criterion. To do that, we chose to implicitly add the mirror image of every defect (a defect with opposite charge at the mirror image location as reflected by the closest boundary) and permit linking of defects and anti-defects in the same frame if no closer/better continuation is available. These links would then correspond to creation/annihilation events if none of the defects involved are self images and to entering/leaving events if they are. Annihilation/leaving events are identified in the frame at time t (corresponding to the disappearance of labels from the tracking scheme) whereas creation/entering events are identified at time $t+1$ (corresponding to the addition of new labels to the tracking scheme) as represented in Figure 2.4. Defects at time t that find their closest match at time $t+1$ are continuations, in which case the label at time t is propagated to $t+1$. All the links must also necessarily follow the topological rules of defects i.e. continuation can only be with a defect of the same charge and creation/annihilation with oppositely charged defects.

The last thing that needs to be specified is the measure used to determine which defect

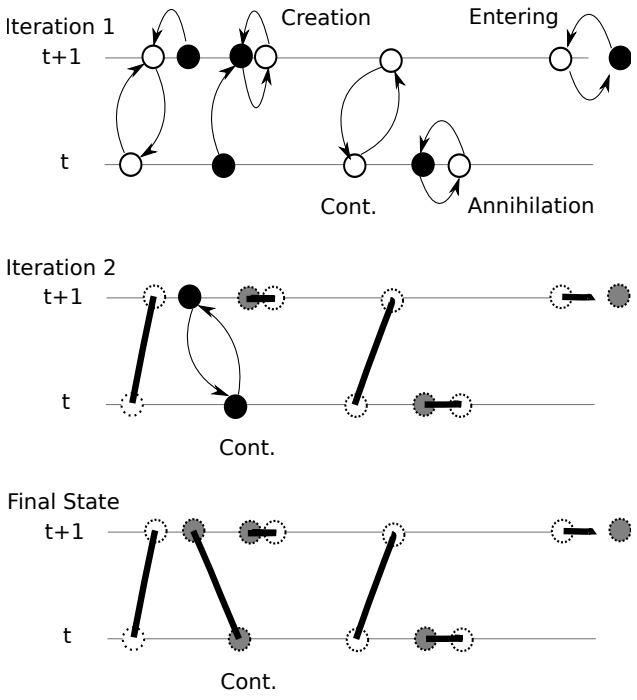

Figure 2.4: Schematic representation of the recursive linking process. Every defect selects their preferred linking partner according to some measure. Partners that form a loop of reference are linked (represented by a thick line on the following recursive step) and the remainder look for their second choice of partner until no defects are left. The charge of the defects, represented by a full *vs.* empty circle, prohibits certain links. For example, no defect at time t can be linked to a defect with opposite charge at time $t+1$. Likewise, no defect of the same charge can be linked in the same frame.

is more likely to be the proper linking partner. The Euclidian distance would be sufficient in many cases, but we chose to introduce a bias variable that changes the effective distance between anti-defect pairs such that

$$d(x_1, x_2) = \begin{cases} |\vec{r}_2 - \vec{r}_1| & q_1 = q_2 \quad \text{and} \quad t_1 \neq t_2 \\ C_{\text{bias}}\left(|\vec{r}_2 - \vec{r}_1|\right) & q_1 \neq q_2 \quad \text{and} \quad t_1 = t_2 \\ \infty & \text{otherwise} \end{cases} \tag{2.16}$$

where $\vec{r}_1$, $\vec{r}_2$, q_1, q_2 and t_1, t_2 are the positions, topological charges and time frames of two defects x_1 and x_2. Defects are linked together and their label shared (for continuation) if this distance is minimal from both defects' points of view. If they disagree, they will be re-evaluated at the next recursive iteration until all defects are linked in this manner. Although

this may seem convoluted and somewhat arbitrary, it permits us to treat all defect events on the same footing and adjust the relative preference of continuation vs. other events via a single parameter. As a rule, we always want to favor continuation over new creation or annihilation to avoid bead-like chains of annihilation/creation over and over again so we typically set $C_{\text{bias}} = 2$ to this effect. On the other hand, values too large would result in long, unphysical, and unlikely continuation links. There is fortunately a large range of this parameter where the results are robust, which is what we are interested in. The specific range will depend on the frequency of sampling and the time scale of the dynamics and must be ascertained through the robustness of the results.

The resulting identification of events in 2D can be confirmed directly in an interesting way. We built a model of bipartite random walkers on a lattice where the creation rate is set such that there is a constant (independent of the number of pairs already present) probability that a new defect pair be created side by side somewhere on the lattice. Furthermore, the annihilation events (when two random walker come into contact on the same lattice site) can be directly read from the trajectory of the random walkers, whose identities are preserved from frame to frame and so, do not need identification. It is important that the rule of evolution be stochastic with a chance for the walker to stay immobile. We found that, if we applied the previous clustering method to the random walkers, we obtained rates that matched almost exactly the expected values. This is the most significant and meaningful test of such a method to date as far as we know.

2.3 Numerical methods in 3D

2.3.1 Localization of the defect loci: filaments

By extension of the 2D case, vortex filaments are 1D parametric curves $[x(s), y(s), z(s)]$ with arclength s. In every volume element (or voxel), filament segments are solutions of the

isosurfaces intersection equations

$$a(x,y,z) = a_0, \qquad b(x,y,z) = b_0 \tag{2.17}$$

where $f(x,y,z)$ is the trilinear interpolation on a unit cube

$$\begin{aligned} f(x,y,z) &= z\left[(1-y)\left[(1-x)f_{(0,0,1)} + xf_{(1,0,1)}\right] + y\left[(1-x)f_{(0,1,1)} + xf_{(1,1,1)}\right]\right] \\ &+ (1-z)\left[(1-y)\left[(1-x)f_{(0,0,0)} + xf_{(1,0,0)}\right] + y\left[(1-x)f_{(0,1,0)} + xf_{(1,1,0)}\right]\right] \end{aligned} \tag{2.18}$$

and $f_{(i,j,k)}$ correspond to the respective voxel corners. After a few considerations, one realizes that there may be as many as six solutions curves and that this problem is indeed more difficult than what we would wish. Therefore, instead of solving the full 3-dimensional problem above, we chose to apply the simpler 2D defect identification method on all the surface elements in our voxel[6]. As we do that, we attribute a single defect label to every defect detected. Then, for every voxel, we consider the list of all defects present on the surface of that voxel. Topological constraints on a closed surface insure us that there will be an equal number of positive and negative defects and all that remains is to link them. For consistency and in accord with the expected solutions of the full 3D problem above, we link pairs of defects such that the total length of the filament segments inside the volume element is minimal (See Fig 2.5). Although the maximum number of pairs is six, it is very unlikely and one usually has a maximum number of two pairs when two filaments are close to colliding and the minimization of the total length in any particular volume element is easily performed. The simple linking rule also demands that all valid links must go from a negatively charged defect to a positive one (in every voxel) and this guarantees that the loci of segments form directional lines (filament) with no branching and that they either have no endpoints (loops) or both a positive and a negative topological charge endpoints at the boundary.

[6]We later realized that the same rationale was used by Clayton [90] in his implementation.

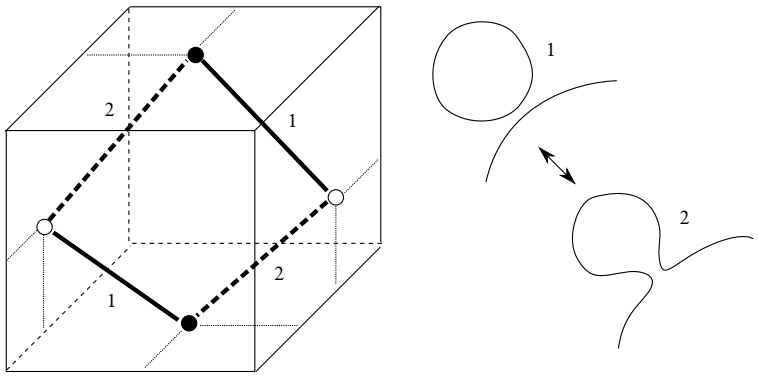

Figure 2.5: Linking of the surface defects in a voxel. In a voxel containing more than two surface defects, a choice has to be made regarding defect linking (left). This choice may result in two widely different filament pictures (right). Therefore, the choice has to be made consistently from frame to frame.

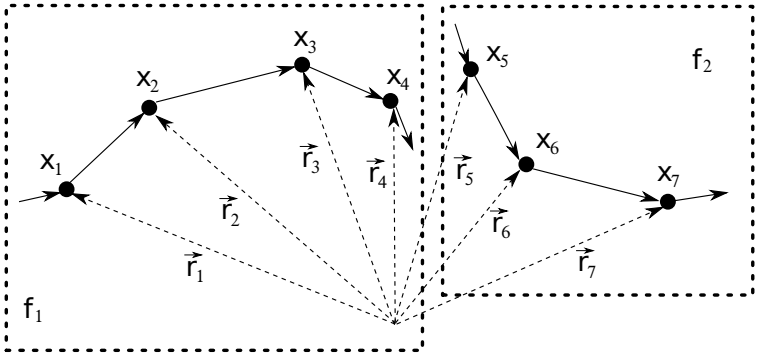

Figure 2.6: Definition of filaments. Defect filaments are contiguous and ordered sets of vectors defined by their end points. The end points are all intersections on the surface elements formed by the cubic (or possibly complex) lattice of the simulation.

2.3.2 Filament clustering

Based on the previous identification, it is natural to define a filament as the set of points that are the endpoints of the directional line segments defining its shape (see fig 2.6). These small vectors link any two following points along the length of the filament. However, we shall omit the directionality for now and only consider the position of the end points of the corresponding segments. Therefore, we have that filaments are sets of points, given by $f_i = \{\cup_{j \in f_i} x_j\}$ where x_j are all the endpoints at position $\vec{r}_j$ in a certain frame at time t, that can be contiguously linked. Filament clustering is the process of attributing a single

filament label to every contiguous loci of filament segments. This is easily accomplished using a well-known Hoshen-Kopelman [91] algorithm once the linking rules between point defects have been established in every voxel, as per the previous section. An example of the resulting clustering is shown in Figure 2.7. Finally, we used a weighted least squares fitting method [92] to estimate the local geometric curvature and twist of the filaments in an attempt to assess statistical geometrical measures of the filament population.

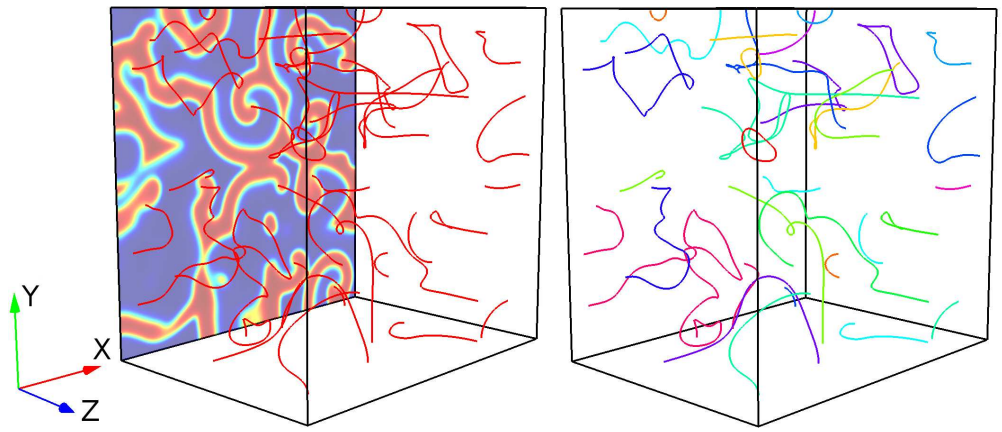

Figure 2.7: Example of filaments in the modified Bär model studied in Chapter 4. Filaments are identified on the left but are not yet labelled uniquely. Filaments have been uniquely labelled on the right but still need to be identified from frame to frame.

2.3.3 Filament tracking and identification of events

Once all filaments are uniquely identified, we need to propagate their labels from one frame to the next. This is known as filament tracking. In the case of defect tracking, we used the distance between defects as a proxy for identity; defects close in space in consecutive time steps were deemed more likely to be the same defect having moved a bit than two defects far apart. We used a conceptually similar procedure by defining a distance measure between filaments. However, it is further complicated by the fact that, unlike defects, filaments can split, merge, recombine, be created and annihilated, enter and leave and change types (which will be defined in the next section). Therefore, we need a measure that would enable us to

decide which of possibly many of these scenarios has occurred for a given filament (or group of filaments). Before we can do that, we need to assess what characteristics of the filaments such a measure would need to be able to capture.

Filament subpopulations

We make a distinction between filaments that intersect the surface of the medium, which we call *strands*, and the filaments that are completely within the bulk, which we call *loops* since they don't have end points. The fact that the only possible end points of filaments occur on the boundary of the medium is a simple consequence of the topological constraint of the phase field. But why do we make this distinction? The answer is very simple: the strand rates are equivalent to the rates of defects as seen from the surface of the medium. Hence, by applying the tracking algorithm for all filaments divided into strands and loops, we are at leisure to extract the total rates as well as the surface rates. Indeed, we have tested that both the 2D method described previously and the 3D method give consistent results for surface defects of 3D media. This was, as a matter of fact, a consistency test that insured that the more complex 3D method was identifying events properly.

Another study [68] distinguished various types of strand filament subpopulations according to which face of a cuboid they were intersecting (transmural I-shaped, cross-mural L-shaped and iso-mural U-shaped strand filaments). Although we started by making this same distinction, we shortly realized there was no real basis for it for volume of different shapes.

Filament events

A filament event occurs whenever a new contiguous filament appears or disappears in the medium or when a filament reorganizes its length through a collision with itself, other filaments or with the boundary. The filament events that were identified are recombination (collision of two strands), splitting and merging (one filament breaking into two and vice-versa), shedding and absorbing (a strand colliding with itself to form an additional loop and

vice-versa), generation and destruction (a loop appearing in the bulk and vice-versa) and entering and leaving (a strand appearing from the boundary and vice-versa). A symbolic representation of these events is shown in Table 2.1 where S, O and $*$ stand for strands, loops and any filament (loops, strands and no filament $\emptyset$) respectively. It can easily be

Event	Symbol	Reciprocal event	Symbol
generation	$\emptyset \to O$	destruction	$O \to \emptyset$
entering	$\emptyset \to S$	leaving	$S \to \emptyset$
shedding	$S \to S + O$ $O \to O + O$	absorbing	$S + O \to S$ $O + O \to O$
splitting	$S \to S + S$	merging	$S + S \to S$
loops to strands	$O \to S$	strands to loops	$S \to O$
strand creation	$* \to * + S$	strand annihilation	$* + S \to *$
loop creation	$* \to * + O$	loop annihilation	$* + O \to *$
creation	$* \to * + *$	annihilation	$* + * \to *$

Table 2.1: Events that contribute to the total creation and annihilation of filaments in the medium and their symbolic representation.

shown and confirmed experimentally, that the total strand event counts, and latter the rates derived from them, satisfy the following reciprocal equalities

$$c_{*\leftrightarrow *+S} = c_{O\leftrightarrow S} + c_{\emptyset\leftrightarrow S} + c_{S\leftrightarrow S+S} \tag{2.19}$$

which is equal to the count measured on the surface. The loops satisfy a similar equality where

$$c_{*\leftrightarrow *+O} = c_{S\leftrightarrow O} + c_{\emptyset\leftrightarrow O} + c_{S\leftrightarrow S+O} + c_{O\leftrightarrow O+O}. \tag{2.20}$$

Putting everything together yields the total filament count

$$c_{*\leftrightarrow *+*} = c_{\emptyset\leftrightarrow S} + c_{S\leftrightarrow S+S} + c_{\emptyset\leftrightarrow O} + c_{S\leftrightarrow S+O} + c_{O\leftrightarrow O+O} \tag{2.21}$$

where the term transforming strand to loop and loop to strands cancel and do not contribute to the total filament creation and annihilation counts.

Filament distance

The method we needed to develop had to be able to distinguish between all the previous filament events. Furthermore, the formulation of the filament as a set of points suggested that the Hausdorff distance may be a natural place to start in our attempt to determine filament identity from one frame to the next in a manner analogous to what has been done for the identification of 2D defects. The Hausdorff distance is defined as

$$H(X,Y) = \max(\sup_{x\in X}\inf_{y\in Y} d(x,y), \sup_{y\in Y}\inf_{x\in X} d(x,y)) \tag{2.22}$$

and is a well known metric to characterize the distance between two subsets X and Y in a metric space with metric $d(x,y)$[7] where x and y are members of X and Y respectively. In our case, no matter what happens, the union of all filaments in a frame must be close (in the sense of the Hausdorff distance) to the union of all filaments in the following frame. If this is not the case, the sampling rate is too low to permit a reasonable clustering of the filaments. However, the previous requirement does not inform us about the identity of any particular filament in the frame. For any filament which doesn't have a direct continuation, its Hausdorff distance to any other filament (in the subsequent frame) might be large. Therefore, in general, the Hausdorff distance is inadequate to characterize the relation between our filaments. However, we know that the Hausdorff distance is the maximum between the Hausdorff premetric[8] where

$$D(X,Y) = \sup_{x\in X}\inf_{y\in Y} d(x,y) \tag{2.23}$$

is the largest distance at which the closest point in Y can be from a point in X. Needless to say, in general $D(X,Y) \neq D(Y,X)$ and this is one of the characteristics we need in order to capture the asymmetry of the relation between breaking and merging of filaments. However, this is slightly impractical because we have to deal with various systems of different sizes and we would rather compare things relative to each other rather than having an absolute

[7]Typically a Euclidean metric $d(x,y) = |\vec{r}_y - \vec{r}_x|$, but sometimes a different metric is used to describe periodic geometries or complex surfaces.

[8]We call them premetric because they do not satisfy all requirement of a true metric

	$F(f_i, f_j) = 1$	$1 > F(f_i, f_j) \geq 0.5$	$0.5 > F(f_i, f_j) > 0$
$F(f_j, f_i) = 1$	Continuation	Major splitting	Minor splitting
$1 > F(f_j, f_i) \geq 0.5$	Major merging	Major recombination	Minor recombination
$0.5 > F(f_j, f_i) > 0$	Minor merging	Minor recombination	Minor recombination

Table 2.2: Filament collision according to their F-distances. The filament labels are propagated through "major" events and continuation.

measure of distances. Therefore, let us define $F(X, Y)$ as the fraction of the length of X for which Y is the closest according to $d(x, y)$[9]. This satisfies our demand since one filament can be close to another along all its length but the converse is not necessarily true. This definition of the fractional length measure, the F-distance, leads us the develop the identification scheme presented in Table 2.2. However, Table 2.2 still does not encompass all possible filament events since filaments can also enter and leave by the boundary and be created and annihilated in the bulk according to the circumstances. The solution to this problem turned out to be very elegant: We simply implicitly added the center of mass of all filaments in one frame to the filament list of the other frame. If a filament falls under the case of continuation with its own center of mass, then it entered/left if it touches the surface or was created/annihilated if it is a loop. This also solves a general concern with identification: the need to have no negative identifications i.e. things that are identified as something (the remainder) because they can't be identified positively (things that satisfy a known criterion). With this last piece, all filament events are positively identified and whatever might remain after the identification quantified the error.

The identification of filament events from frame to frame permits the propagation of unique filament labels. New labels are attributed during creation, entering, splitting and shedding events while they are lost during annihilation, leaving, merging and absorbing events. When filaments collide, the label goes with the largest part of the broken filament ("major" in the identification scheme of table 2.2). Alternatively, one can easily obtain the

[9]Note that this involves all the same operations as with evaluating $D(X, Y)$ except that, as we test all points x in X, we simply keep track of how many closest matches were in Y.

inter-events lifetime distribution from an inspection of the history of every filament label identified in this way.

2.3.4 Description of the algorithm

Previous algorithms attempting to identify filaments from time to time mostly relied on an overlap on a finite-sized grid. There are obvious advantages to such methods. For instance, the speed of such an algorithm is proportional to the volume of the system instead of the square of the volume (assuming constant density of filaments) in a case where one would compare the distance of every filament element to every other as the F-distance seems to demand. Another advantage of the former is that no explicit distance needs to be measured since everything is already binned. On the other hand, there are some noteworthy inconveniences. If the binning is inadequate to the dynamics, things could easily turn out to move in a way such that they do not overlap even though they are still close in space (or closest at least). On the other extreme, filaments could overlap too much and we wouldn't be able to decide which of many are the proper continuations. So it seems that we cannot completely avoid measuring distances after all.

Could we have the best of both worlds i.e. combine the speed of overlap and the reliability of measuring directly the F-distances? Yes. How this is accomplished is by binning the filament elements into subspaces or into a binary tree of subspaces. Before calculating the F-distance, for every filament element, we essentially determine which bin they will search into and be searched from for neighbors. These subspaces are determined from a simple function of their current position. The F-distances are then calculated in the usual manner with all the element members of a bin. Now let us consider the algorithmic complexity of this method. First, since the binning process is proportional to the number of filament elements n_{fe} (which is in turn proportional to the volume in extensive turbulence $n_{\mathrm{fe}} \propto V$), this part should be proportional to the volume of the system. Second are the F-distances calculations, since we do it for each bin separately we have that the computational complexity should be

proportional to V^2/n_b but since the density of filaments is constant (in our assumptions) we chose a number of bins $n_b \propto V$. Putting both together we see that this reduces the complexity from V^2 to V. In fact it is most likely to be proportional to $V \log V$ because of the additional overhead of the binning. This is a net gain. Indeed, in the most extreme cases, we observed a speedup of more than tenfold from calculating the F-distances over the whole volume. This optimization made possible the study of large systems with thousands of filaments, which would have been prohibitive otherwise.

2.3.5 Total surface defect tracking

We have seen that, by dividing the filaments into strands and loops, the filament detection and identification of events could be used to obtain the surface rate without any further complications. However, certain surface observables can't find a simple representation in the filament method. For instance, we couldn't evaluate the lifetime distribution of surface defects based on the lifetime of filaments since filaments can continue while receding entirely inside the bulk of the medium. Therefore, the lifetime of filaments is, in general, different than those of surface defects. Accordingly, there are some cases where we may want to apply a true surface detection method to our volumes. For these cases, we have used a simple projection method to map our simple convex surface into a 2-dimensional manifold — the surface of a unit sphere. The 2D detection method of section 2.2.2 can then be used directly provided we adapt the metric used to evaluate the distance between any two defects to accommodate this projection into a longitude/latitude coordinate system (ϕ, θ). The new distance is simply the arclength between defects x_1 and x_2 at $\vec{r}_1 = (\phi_1, \theta_1)$ and $\vec{r}_2 = (\phi_2, \theta_2)$ defined as

$$d_{\text{arc}} = \cos^{-1}\left(\sin(\phi_1)\sin(\phi_2) + \cos(\phi_1)\cos(\phi_2)\cos(\theta_2 - \theta_1)\right). \tag{2.24}$$

which replaces $|\vec{r}_2 - \vec{r}_1|$ in Eq. 2.16.

2.4 Evaluation of the rates of the defect events

In the following, both the vortex and filament rates are evaluated using the exact same techniques. The only difference is that, in the case of filaments, the overall rates can be further subdivided according to the type of event responsible for the change in the overall number of filaments, and divided between the filament subpopulations to determine the surface rates. Let us review the methods we used to evaluate these rates and some common issues and difficulties that are involved.

2.4.1 Time series method

The conventional method for measuring rates is based on the analysis of the time series n_t of the total number of objects (defects, defect pairs or filament loops or strands). If the series sampling is high enough, events do not occur concurrently in the large volume, or at least very rarely. In this case, if $n_{t+1} > n_t$, a creation event occurred between t and $t + 1$[10] when n_t objects were present in the system. On the other hand, if $n_{t+1} < n_t$, an annihilation occurred with n_t objects. The total creation/annihilation counts $C_{\pm}(n)$ are then normalized over the time length of the series to obtain the rates i.e.

$$r_{\pm}(n) = \frac{1}{T\Delta s} C_{\pm}(n) \tag{2.25}$$

where T is the number of frame analysed and Δs^{-1} is the frequency of this analysis in the time units of the system.

However, for large system size, events are bound to occur simultaneously in parts of the system that are presumably independent (due to the rapid loss of correlation with distance) and the sampling rate that would be required would quickly become prohibitive. With a sampling rate too low, many events would occur at the same time and, as we can see in Figure 2.8, might not appear at all in the time series n_t. Therefore, if one were to use the

[10] If the frequency of concurrent events is low, it can effectively be ignored, otherwise the sampling rate needs to be increased.

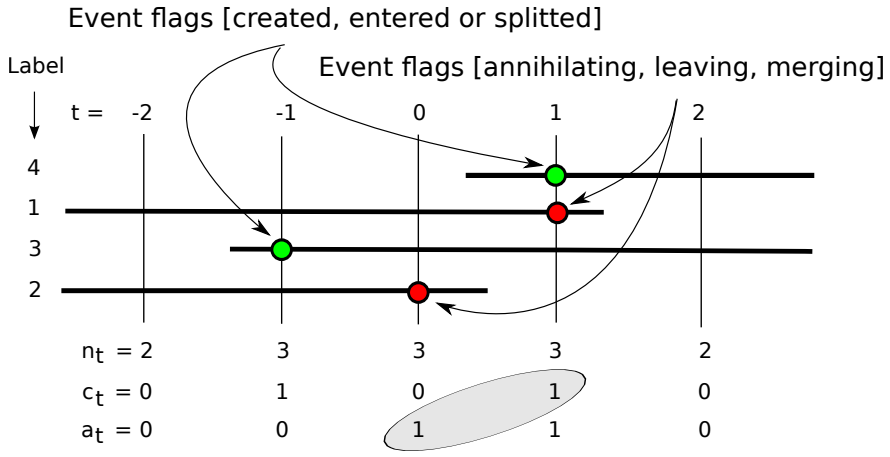

Figure 2.8: Schematic representation of the time series resulting from the defect tracking.

previous method to compute the rates of creation and annihilation in such a case, a large error could be made. However, this problem can be avoided in an interesting manner.

2.4.2 Independent events model

In this section, we describe some progress we made on evaluating the rates of events in large systems where many events occur concurrently and independently. From the time tracking algorithm, we obtain the first time at which a defect is found and the last time at which it is detected as being the same defect. Therefore, we can extract the time series c_t ($\equiv c_{*\to *+*}$ at time t), a_t ($\equiv c_{*+*\to *}$ at time t), e_t and n_t where n_t is the total number of labels existing in the system at time t, c_t is the number of labels beginning in the interval $t \in]t-1, t]$, a_t is the number of labels ending in the interval $t \in [t, t+1[$ (see Fig 2.8) and e_t is the time series of a particular event count. Accordingly, it is easy to see that

$$n_t = n_{t-1} + c_t - a_{t-1} \tag{2.26}$$

and so, c_t creation/entering events and a_{t-1} annihilation/leaving events occur between the transition from $t-1$ to t. Since we are often interested in the rates conditioned on the number of objects present in the system at the time the event took place, we need to know the probability that a given event occurred with $s \in [n_{t-1} - a_{t-1}, n_{t-1} + c_t]$ objects in the

system when going from n_{t-1} to n_t.

Let's focus for now on the problem of having N_- annihilation and N_+ creations of objects but we do not know in which order they occurred. Evidently, in the absence of further information, each defect event has uniform probability to have occurred in any particular order. Therefore, we need to find the fractional event count of a $\pm$ event when there are s objects

$$p^{\pm}(s) = \sum_{t=0}^{N_+ + N_- - 1} p(s,t) p^{\pm}(s,t) \tag{2.27}$$

where $p(s,t)$ is the probability to be at s at an intermediate time t and $p^{\pm}(s,t)$ is the probability of having the $\pm$ event at that particular intermediary time. The intermediary times are, by definition, one elementary event of the two possible kinds (+ or −). Note that $p^{\pm}(s)$ simply involves the sum over all possible histories of how to reach $s = N_+ - N_-$ from $s = 0$ in $N_- + N_+$ elementary steps. Then

$$p^{+}(s,t) = \frac{1}{N_+ + N_- - |t|} \left(N_+ - s - \frac{1}{2}|t-s| \right) \tag{2.28}$$

$$p^{-}(s,t) = \frac{1}{N_+ + N_- - |t|} \left(N_- - \frac{1}{2}|t-s| \right) \tag{2.29}$$

for $t - s \in$ even and zero otherwise. The degeneracy is given by the following product of binomial coefficients

$$p(s,t) = \frac{\binom{N_+}{s+\frac{1}{2}|t-s|}\binom{N_-}{\frac{1}{2}|t-s|}}{\binom{N_+ + N_-}{|t|}} \tag{2.30}$$

Finally, the fractional event counts $p^{\pm}(s)$ are normalized in such a way that

$$\sum_{i=-N_-}^{N_+} p^{\pm}(i) = N^{\pm} \tag{2.31}$$

hence it provides a generalization of the discrete event count that we had before where $p^{\pm}(s) = \{0, 1\}$. For example, assuming $N_+ = c_t = 2$ and $N_- = a_{t-1} = 3$, we have

$$p^{-}(s) = \left[0, \frac{1}{10}, \frac{3}{5}, \frac{8}{5}, \frac{3}{5}, \frac{1}{10} \right] \tag{2.32}$$

$$p^{+}(s) = \left[\frac{1}{10}, \frac{3}{5}, \frac{3}{5}, \frac{3}{5}, \frac{1}{10}, 0 \right] \tag{2.33}$$

where the vector components correspond to the index $s \in [n_{t-1} - 3, n_{t-1} + 2]$ and everything outside this range is zero. It is then easy to compile these fractional event counts for any event e_t for the whole time series and obtain the total event count $C_e(n)$ of event e with

$$C_e(n) = \begin{cases} \sum_t \frac{e_t}{c_t} p^+(n,t) & e_t \in c_t \\ \sum_t \frac{e_{t-1}}{a_{t-1}} p^-(n,t) & e_t \in a_t \end{cases} \tag{2.34}$$

which depends on whether the events of e_t contribute to the total creation or to the total annihilation rates and assumes that the events are independent and uncorrelated. Even though this can be false in general, it probably holds on the timescale of the sampling rate where almost simultaneous events are likely far apart in this large system and have nothing to do with each other. Finally, the rates are obtained using Eq. 2.25. We used both the original time series method and our new method with various sampling rates. Our results show that the latter converges faster (less sampling frequency required) to the real rate values i.e. the limit when the sampling rate goes to infinity and where both methods seem to converge (see Fig 2.9).

2.4.3 Pitfalls of the independent event model

One critical pitfall of the previous method occurs if the events are in fact correlated in some manner. In 2D media, we separate the events into two sets depending on whether they occurred on a positive or negative topological defect. The rates are evaluated on either or both time series. These series are highly correlated due to the nature of the most prominent events in large systems: creation and annihilation of defect pairs. However, on their own there is little or no correlation between any two creation events.

Another simple case where such a problem occurs is with a very thin slab of a 3D medium. The problem arises in the degenerate case where all filaments are purely straight lines and are now created pairwise (like a vortex pair would). All filaments (corresponding to a pair of topological charge on the surface of the medium) appear in the time series of filament events. Hence, this time series contains highly correlated creation of filament pairs and the

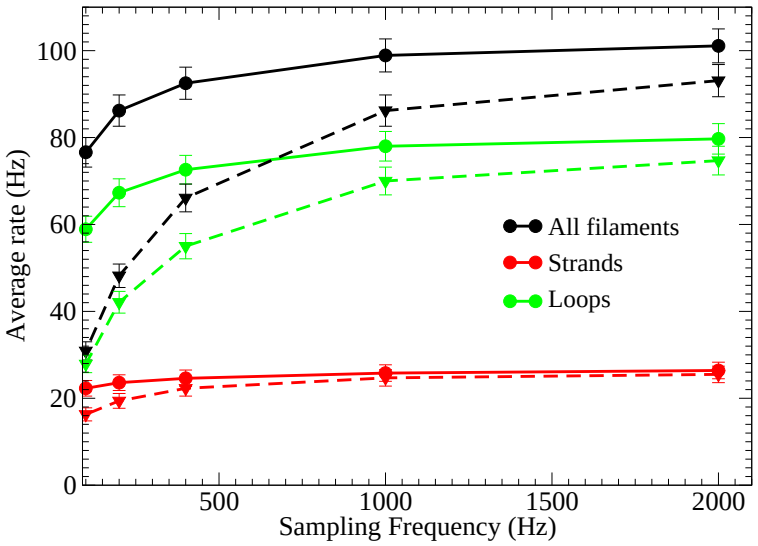

Figure 2.9: Typical average rates (in the CGLE) as a function of the sampling frequency evaluated with the time series method (triangle with dashed lines) and with the independent event model method (circle with full lines). The independent event model method converges faster to the asymptotic value at infinite sampling rates because, even at low frequencies, all events are detected by the tracking algorithm whereas events are omitted with the old time series method, resulting in lower estimates.

method breaks down. In this particular case, if there are n_t filaments in the system at time t and a pair of filaments is created, both must be conditioned on n_t. We will call this method the *dependent event method*. We have verified that both this method (on filaments in thin slab) and the independent event method (on defects in 2D) yield the same results in the limit where the sampling rate is very high, and few events occur concurrently.

2.4.4 Comparison of rates from different regimes and system size

In the course of our investigation, we chose to measure the creation and annihilation rates of defects in various systems of different sizes and in various parameter regimes. These statistical measures correspond to a limit behavior of the system that is only dependent of the particular regime (i.e. not on the initial conditions). Therefore, a sufficient transient has to be elapsed to reach this limit behavior, which is only recognized through the progressive convergence of averages (e.g. average number of defects, average rates, etc.). Also, we will

need a simple way to present and compare this heavily heterogeneous data such that our results should not depend crucially on the system size. From the comparison of many systems and regimes, we found empirically that we could assume that the *total* (it applies to both the total filament rates and the surface rates) rates have the general form

$$r_+(n) = c_0 + c_1 n \tag{2.35}$$

$$r_-(n) = a_0 + a_1 n + a_2 n^2 \tag{2.36}$$

with an average rate $\langle r \rangle$ and number of defect pairs $\langle n \rangle$. Why is it likely to be sufficient? Each of the terms stands for one or many processes and some of these processes are extremely unlikely to be dominant, which allows us to reduce the form of rates to these few terms only. There is, however, no fundamental reason to accept these other than it offers us a way to express these rates in a simple way and to compare different regimes. It is very possible that some regimes will fail to obey such a description, in which case we can't compare them or would need a more general framework. For example, some cases have shown extremely sharp saturation effects which result in high rates of annihilation of defects above a certain density and cannot be captured by the previous form.

Now let us normalize these rates with $\bar{n} = n/\langle n \rangle$ and $\bar{r}(\bar{n}) = r(n)/\langle r \rangle$ such that $\langle \bar{r} \rangle = 1$ and $\langle \bar{n} \rangle = 1$. We have

$$\bar{r}_+(\bar{n}) = c_0 \frac{1}{\langle r \rangle} + c_1 \frac{\langle n \rangle}{\langle r \rangle} \bar{n} = \bar{c}_0 + \bar{c}_1 \bar{n} \tag{2.37}$$

$$\bar{r}_-(\bar{n}) = a_0 \frac{1}{\langle r \rangle} + a_1 \frac{\langle n \rangle}{\langle r \rangle} \bar{n} + a_2 \frac{\langle n \rangle^2}{\langle r \rangle} \bar{n}^2 = \bar{a}_0 + \bar{a}_1 \bar{n} + \bar{a}_2 \bar{n}^2 \tag{2.38}$$

and by construction $\bar{c}_0 + \bar{c}_1 = 1$ and $\bar{a}_0 + \bar{a}_1 + \bar{a}_2 = 1$. Given these relations, it is sufficient to consider the normalized constant component $\bar{c}_0$, which allows us to recover the actual observed total creation rates from $\frac{r_+(n)}{\langle r \rangle} = \bar{c}_0 + (1 - \bar{c}_0)\frac{n}{\langle n \rangle}$. Extensive STC means that the attractor dimension scales with the size of the system $D \propto V$. Incidentally, in our case of DMT, the average rates and number of defects also scale with the volume of the system. Now, what happens to the normalized coefficients as the system size is increased? It depends

on what process the coefficients represent. If the form of the rate is the result of some process that occurs stochastically and independently in every part of the system, then we expect that the form should be independent of the size of the system and $\bar{c}_0$ is an intensive quantity. If on the other hand, part of the form is due to the boundary conditions or to a process that does not occur everywhere uniformly and independently (e.g. boundary effects or breakup due to global modes), then we might expect that the rate functional form may change as the system volume is increased, even if the density of defects saturates.

Another quantity we will consider for comparison between different turbulent regimes is the shape factor of the distribution of surface defect pairs, which is defined as the ratio $\gamma_n = 2\frac{\sigma_n^2}{\langle n \rangle}$ where σ_n^2 is the variance of the distribution of n. γ_n also captures information about the spatial distribution of defects [78][11] and is fully determined by the functional form of the total creation and annihilation rates [38, 42, 43].

We may note that according to this framework, the creation rates expected from the Gil *et al.* model that we discussed in section 1.4 can be expressed concisely as $\bar{c}_0 = 1.0$ where the resulting distribution of defects characterizing the fluctuations appears as a squared poissonian distribution with a shape ratio $\gamma_n = 1.0$. The detail of the rates, average number of defects and average rates, are then simply seen as characteristic of the particular model and regime, though their densities may have some scaling properties of their own close to onset of DMT.

Finally, all the other error bars on the previous observables were estimated using a jackknife method where the value of interest was computed using randomly chosen contiguous samples of half the maximum length of the simulation. Such a method has the advantage of taking into account the fluctuation of the time series, assuming that the overall sample is indeed representative of the actual behavior. We adjusted the length of the simulation to the volume and to the period of the system such that it corresponded to many thousands of

[11]Note that in our case, n is the number of defect pairs whereas in that paper, $n = n_+ + n_-$ is the total number of defects. We use the number of pairs because it corresponds directly to the number of strands in the 3D case.

spiral cycles, and a typical run would include tens of thousands of creation and annihilation events. All error bars in this thesis represent one standard deviation assessed through the previous method.

2.4.5 Trimming and filtering

This seems a good place to make a very important note about the possible spuriousness of defects due to discretization effects, incorrect or undefinable phase center and possible noise in an experimental context. The first scenario for spuriousness comes directly from the definition of defects. Since a path encircling both negative and positive topological charge would report a null topological charge inside this path, finer discretization is expected to yield an increased number of defects. On the other hand, we also expect that features of the dynamics are on a certain scale and as such, new features are not found *ad infinitum* but converge to a certain limit when discretization becomes finer and finer. Another discretization effect, only found in 3D, is due to the small features of filaments on the length scale of the discretization and the model used to link segment units on that scale (in As shown in Figure 2.5, we decided to link the filaments segments in a way that minimizes the total filament length inside every single voxel). This effect would typically cause a supernumerary appearance of short-lived small filament loops and associated events. Another trivial and important source of spuriousness occurs equally in 2D and 3D due to the possible imperfect periodicity of complex oscillatory media. Some regions may "skip a beat" resulting in the creation and sudden annihilation of defect pairs/small filaments. These objects are usually of short length and short lived. Finally, noise, from experimental observations or added to the simulation could also induce small scale structures that would be identified as defects/filaments. The diffusion would then promptly destroy spurious structures at these scales, making them short-lived as well. Generally speaking, all these effects tend to produce defect rates that have an additional linear dependence on the number of defects already present.

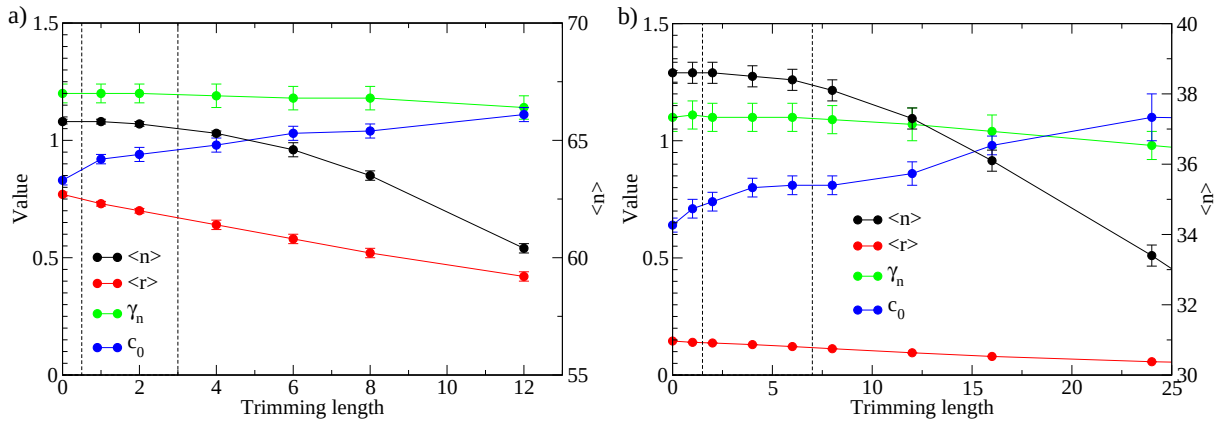

Figure 2.10: Various statistical measures of surface rates (for the modified Bär model used in Sections 3.3 and 4.2 at a) $e = 8.5$ and b) $e = 10.8$) plotted against the trimming length shows that, apart from the rates which are affected most, other measures are near constant or even plateauing past the removal of very small objects until the average number of defects starts to be affected. This offers a reasonable range of trimming over which the statistics are robust (between the two dashed lines). This is our criterion. All error bars represent one standard deviation.

These underlying causes suggest a simple solution since all the spurious objects are either very small, short lived or, more likely, both. We call *trimming* the removal of small filaments, and all their associated events, from the time series. These small filaments are indeed shown to be extremely transient, as evidenced by their large contribution to the total rates (e.g. in figure 2.10). However, many quantities like the average number of defects and the distribution shape ratio are extremely robust in the face of trimming of small filaments, which is an important fact tested here against trimming. However, trimming (or any other form of filtering) filaments with too much zeal starts to eat away at the robust objects, as evidenced by the rapid loss of average number of filaments in Figure 2.10 for thresholds above the second dashed line. This remains largely arbitrary otherwise, and the particular "sweet spot" (where the statistics vary very little) will generally depend on the system length scales. An appropriate choice of Δx and Δs (sampling interval) invariably improves the tracking algorithm's ability to detect the defect events accurately and thereby tends to reduce the average rates, also reducing the need for trimming and filtering. In the end, trimming is

a two-edged sword: while it appeared necessary in some cases due to some unavoidable spuriousness, it can also be used to force any data to say anything. It must therefore be used parsimoniously.

2.5 Experimental limitations

The methods described in this Chapter are most often used in an experimental context[12] i.e. that the defects are not defined, they are measured, even in "noise free" numerical simulations[13]. All measured quantities are subject to some form of experimental uncertainty intrinsic to the method. Many of these errors and biases can be mitigated by an appropriate filtering and by careful selection of the parameters of the simulations, as we have seen, and the same methods could be applied to situations where we actually have noisy signals and imperfect data. However, there is no way to escape the limitations of statistical fluctuations.

In our case of extensive STC, small finite systems may be dominated by boundary effects and their averages may fall short of extensivity. However, as the system size increases, the averages and rates have increasingly greater error for a given simulation length. This limitation is simply the result of the law of propagation of error. For an overall time series n composed of N presumably uncorrelated parts n_i and assuming that, due to the finite size and random fluctuations, each series has an error on the average $\Delta \langle n_i \rangle = \text{constant}$ and an error on the standard deviation $\Delta\sigma^2_{n_i} = \text{constant}$, we have

$$\Delta \langle n \rangle \propto \Delta\sigma^2_n \propto \sqrt{N} \propto \sqrt{V} \tag{2.39}$$

but if the series are instead compiled back to back to form a longer time series (of a smaller system), we have

$$\Delta \langle n \rangle \propto \Delta\sigma^2_n \propto \frac{1}{\sqrt{N}} \propto \frac{1}{\sqrt{T}} \tag{2.40}$$

[12]Numerical experiments are experiments just the same as laboratory ones as far as the methods to analyze the results are concerned.

[13]Noise-free here means that we are dealing with purely deterministic dynamical systems. Actual laboratory experiments are not noise-free because of the typical weak coupling of the experiment and measuring apparatus with the environment.

which means that to obtain estimate with roughly the same error we must increase the simulation length T in proportion to the volume V and we thus quickly reach prohibitive simulation sizes (because the volume of data to analyze increases in proportion to the volume of the system and the length of the simulation). In actuality, the situation is even worse and the simulations need to be much longer than what this argument would suggest because we are interested in quantities that are more sensitive to the fluctuations than the simple averages. For instance, we measured the rates of creation of new objects but the relative support of the distribution of the objects ($\sigma_n / \langle n \rangle$) grows smaller with larger averages and thus, with the same relative error, the fitted linear regression for the rates becomes more and more unreliable. In the limit $L \to \infty$, any linear relation can be fit to a point and the rate functional form becomes highly inaccurate. In the end, it seems that the only thing we can do at the moment is select a system size that is not too small, to avoid the systematic error due to finite size, and not too large to avoid the random error due to large fluctuations. Empirically, it seems that a linear size L around 10 times the wavelength of the pattern is close to this "sweet spot" with our current technology and methods.

Another factor critical in many of our cases is the time scale (and length scale) dilation that is observed when approaching certain transition lines. For example, the average rate of events tend toward zero as we approach certain instabilities[14]. This makes precise measurement more computationally costly close to these instabilities, and many of our simulations reached the boundary of our patience, extending to over two weeks to almost a month on a 2.8 GHz Xeon 5560 quad core processor (using a parallelized code running on the 4 cores) in the worse cases. This large variety of scale leads to an interesting problem which, had it been identified sooner, could have been implemented directly in our algorithms to sample the average frequency of events over a small sample and dynamically adjust the sampling rate such that one always has an average rate of roughly one event per frame. In retrospect, this, coupled with an adaptive stepper routine, could have tremendously reduced computation

[14]For example, this can be seen clearly in Figure 4.7.

time in some cases.

2.6 Other measures of defect turbulence

We have described our methods for detecting, identifying and clustering vortices and filaments. With this information, we can measure the rates of the various events with an unprecedented accuracy even in the presence of many concurrent events. However, there is no reason *a priori* to put an overemphasis on the rates of events alone. Other measures of STC may be more relevant to characterize the turbulent state or its transitions. There are a few measures that have been used in the past or that we attempted to use for the first time. Let's describe them and a few possible applications.

2.6.1 Pair correlation function

The pair, or anti-pair, correlation function serves as a estimator of the mobility of defects. The normalized pair correlation function for oppositely charged defects is defined as

$$h\left(|\Delta\mathbf{r}|\right) = \frac{\left\langle n_{+}\left(\mathbf{r},t\right) n_{-}\left(\mathbf{r}+\Delta\mathbf{r},t\right)\right\rangle_{\mathbf{r},t}}{\left\langle n(t)\right\rangle_{t}^{2}} - 1 \tag{2.41}$$

which is estimated by counting the number of positive defects in circular bands (depending on the detection method used, the bands may have to be discretized or not) of radius $|\Delta\mathbf{r}|$ around every negative defect. The shape factor of the distribution of defect pairs γ_n relates directly to the pair correlation function through the compressibility equation as shown in Ref. [78].

2.6.2 Defect loop size distribution

Multiple defect trajectories can be contiguously traced though collisions (defect events) into a single object that we call *defect spacetime loop clusters*. Huepe *et al.* [45] and Granzow and Riecke [81] characterized the spatial extension of 2D defect spacetime loop clusters by

measuring the maximal separation (x-span) that two vortices which can be linked unambiguously to a single original creation event and to a single final annihilation event had during any of the intervening time. This distribution was found to have a power law character in many cases and could therefore be a scale free characteristic of the DMT state. We shall take their notation to facilitate comparison. They characterized the cumulative frequency distribution (CFD) $P_{\mathrm{x}}(x) = \int_x^\infty p_{\mathrm{x}}(x')dx'$ where $p_{\mathrm{x}}(x)$ is the corresponding relative frequency distribution (RFD) also known as probability density function (PDF). In many cases, the CFD was found to scale as a power law $P_{\mathrm{x}}(x) \propto x^{-\beta}$ which implies that the PDF would scale as $p_{\mathrm{x}}(x) \propto x^{-(\beta+1)}$ in the same regime. Therefore, a critical exponent β shall always refer to the CFD whereas an exponent $\beta + 1$ refers to the PDF.

2.6.3 Defect loop cluster size distribution

Using the same spacetime loop clusters defined above, we can define the size of a cluster (n-span) as the number of creation (or annihilation) events that are involved in a single cluster. A pair of defects that self-annihilate therefore has n-span = 1. Likewise, a power law scaling was observed in many cases with PDF scaling as $p_{\mathrm{n}}(n) \propto n^{-(\alpha+1)}$ with critical exponent $\alpha + 1$.

This distribution can be easily generalized to a cluster of filaments as the number of filament generating events (creation, splitting, shedding) that can be linked contiguously to one another. However, due to the presence of filament loops inside the medium, the cluster size as measured from the surface defect will be different than the cluster size of the filaments. Nonetheless, the form of the distribution may still give an insight into the type of turbulence since a 2D turbulence dominated by vortices that self annihilate would probably result in filament turbulence where small loops form and collapse soon after. A similar power law behavior is then expected in fully developed filament turbulence.

2.6.4 Defect loop lifetime distribution

The third and last 2D defect statistic investigated is the spacetime loop cluster lifetime (t-span) distribution. It is analogous to the x-span distribution but involves measuring the total time span between the earliest and latest event in a cluster of defect trajectories. Likewise, one could think of measuring the lifetime of a single vortex trajectory, from its creation to its annihilation. Typically, it is found that the single defect lifetime distribution followed an exponentially decaying distribution whereas the lifetime of clusters follow a power law distribution, whose PDF scales as $p_{\mathrm{t}}(t) \propto t^{-(\gamma+1)}$ with critical exponent $\gamma + 1$.

This distribution can also be generalized to the filaments. Whereas the single filament lifetime is the time between any two filament events, the cluster lifetime is the time span between the first and last event of a cluster i.e. all the filament labels that have at some point touched one another. However, in this case also, it is unclear how the distributions of the lifetime of surface defects should relate to the distributions of lifetime of the filament. The only thing we can say for sure is that the lifetime of the surface defect (single or cluster) cannot possibly be greater than the lifetime of the filament, since events that appear on the surface are a subset of all possible filament events. This would imply that the distribution of lifetime of filament is always less steep or equal to the lifetime distribution of surface defects. To our knowledge, these relations have never been explored.

2.6.5 Filament length distribution

Maybe the closest equivalent to the defect spacetime loop size distribution for filament is the length distribution. Filaments that are many times longer than the linear system size have been found in our simulations. In the CGLE especially, we have found that long filaments distribute according to a bimodal power law where the very long filaments scaled as $p(l) \propto l^{-\kappa}$ up to an exponential cutoff.

2.6.6 Filament growth rate

An interesting measure is the growth rate of filaments. The growth rate of an isolated filament (or filament loop) has been used to characterize the tension of the filament — a filament which neither grows nor shrinks has no tension and is therefore stable. Positive tension shrinks the filament whereas negative tension makes it expand. In reality, thing are never that simple and the rate of growth depends on the curvature of the filament as well. However, in the case of turbulence, we can compare the expected tension to the effective tension as measured by the average rate of growth of the filaments, which have various curvatures and shapes. In general, this effective tension may differ from the mathematically defined tension of a filament [73, 74], which only applies to limiting cases of filament behavior. We found an interesting quantity by conditioning the average rate of growth to the length of the filament. On average, the total length of filaments is a steady quantity and we found that certain turbulent regimes tend to have small filaments growing and large filaments shrinking whereas some others have exactly the opposite behavior. This indicates a fundamental change in the mechanism of turbulence, which we can relate to the rate and to the dominant instability.

2.6.7 Filament twist

Finally, filament twist corresponds to the sum of the geometrical twist (twist of the spatial curve formed by the filament) and the field twist around a filament along its length (the rotation of the local field gradient with respect to the normal of the filament) [70, p. 276]. It has been shown that some instabilities caused by diffusion twist anisotropy are mediated by the formation of traveling twistons along the filaments i.e. coherent travelling regions of high filament twist. The filament motion is then driven to reduce the local twist causing elongation and collision of filaments [49, 50]. However, to observe these effects in a turbulent setting, we would need to generalize twist quantities to multiple filaments. Perhaps, this

could be done in a manner similar to how we previously defined the average growth rate of filaments. There is likely a minimum length of filament needed for twist to accumulate and a maximum amount of twist before it relaxes by changing its shape. These quantities, which we would capture by such a distribution, could be characteristic of the instability even in the turbulent regime. These questions are still very much open, though our method already provides the means for measuring such quantities.

2.7 Chapter summary

We reviewed the numerical methods with which one can identify, track, cluster, and evaluate a range of quantities and statistical measures pertaining to phase singularities in defect turbulence. We have developed many of these methods independently[15], solved many limitations and clarified our understanding in the process. The ultimate test of validity is that the various methods presented here all produced consistent results. For example, rates obtained with 3D detection of events in a case where the thickness of the medium tends toward zero would collapse on the rate measured using the 2D detection method. Likewise, the rates found using the 2D detection of events method would collapse on the rates as measured directly from the time series, in the limit where the sampling rate tends toward infinity. Furthermore, the measured rates were found to be consistent in the case of a bipartite random walker model where the events are defined instead of measured. In such a case, the expected rates can then be known *a priori*. This insured full consistency of all our methods.

[15] Even though it turned out some of these methods already existed. In particular, the bilinear interpolation method to locate defects was already used by Clayton in Ref. [90]. However, as far as we can tell, the clustering schemes presented here are new and unique. Specifically, our filament clustering method did not rely on a smoothing and overlap but instead used the distance between filaments to determine clustering.

Chapter 3

2-dimensional media

Many pattern forming systems can be aptly modeled as 2-dimensional RD systems, either because we restrict the investigation to surface observations, because they are sufficiently thin slabs, or because they are inherent surface processes. In the first case, it is not always clear that a 2D representation can faithfully reproduce all aspects of the 3D surface behavior, though many of the surface phenomena are qualitatively similar to 2D phenomena. For instance, many of the observed phenomena of spiral wave, wave propagation and breakup can be captured by 2D models of the heart dynamics even though the full 3D dynamics may be essential to account for other experimental observations [20]. In the case of inherent surface processes however, the reaction, or process, occurs only on a very thin layer hence the system is always best characterized using two extended dimensions. For example, electroconvection in liquid crystals [22], oxidation catalysis on platinum [93, 94], undulation chaos in inclined layer convection [42, 45] and bacterial culture growth [17, 18] are thought of as essentially 2D processes. However, many of these cases are gel reactors where the thickness of the thin medium may nevertheless be a significant fraction of the pattern length scale such that the "2D-ness" of the medium may not be *a priori* obvious. We will return to this question in Chapter 4.

Simulations of 2D pattern forming systems have shown a large variety of phenomena. Upon varying system parameters, spiral waves may destabilize and the resulting instabilities often lead to more complex coherent patterns or to spatiotemporally disorganized dynamics. Instabilities like the meander instabilities [95, 93] or the period-doubling instabilities [96, 97, 98, 99] can lead to core [100, 101] or far-field breakup [23], though not necessarily. When instabilities do lead to breakup, the resulting regime often preserves some remnant

features acquired through the instability that generated it. One famous example is synchronization defect line (SDL) turbulence [79, 72]. The period-doubling instability corresponds to a resonant Hopf bifurcation in the wave train leading to period-2 spirals which emit waves with doubled wavelength and temporal period [46, 72, 102]. In excitable media, such a change of periodicity is known as alternans, but occurs through a different process owing to the excitable dynamics [103, 104]. An additional feature of the period doubling instability is the occurrence of synchronization defect lines (SDLs) that extend from the spiral core and which accommodate the necessary mismatch of the phases of the oscillations that are emitted by the spiral core. This instability of the simple oscillatory behaviour doesn't necessarily lead to a breakup of the spiral. Even in a case with multiple non-stationary spiral defects, the spatiotemporal chaotic state doesn't necessarily lead to DMT and may instead be described as a "vortex liquid" [72]. In this state, the chaotic fluctuations are sustained by the creation/annihilation and motion of SDLs. However, when the local dynamics becomes itself chaotic, the random creation and annihilation of defect pairs become important and lead to a state of DMT. This case shows a clear example of STC transition from regular dynamics (simple oscillatory) to regular SDL (period doubled dynamics) to SDL turbulence (characterizable by the total SDL length) and finally to DMT (characterizable by the statistical properties of defects).

In this chapter, we will endeavor to explore various STC regimes of DMT, the behavior close to onset and, when applicable, the turbulence transitions therein. It is a very difficult problem because, unlike the thermodynamic equilibrium phase transitions where the behavior of the free energy dictates the type of transition (first order, second order, etc, and the critical scaling exponents), there are no obvious conserved quantities in our cases and no consensus on what characterizes these complex stationary states and the possible non-equilibrium transitions that appear in certain cases [27, p. 350]. Research on universal properties of state transitions in non-linear dynamics is very much ongoing. Here, we will

consider two types of observables: the defect creation and annihilation rates and the space-time defect loop statistics, which we introduced in section 2.6, and which appear to have certain scale free properties.

3.1 The complex Ginzburg-Landau equation

The complex Ginzburg-Landau equation (CGLE) is derived in the context of oscillatory media undergoing a supercritical Hopf bifurcation (type-III-o) [27, p. 196] and, as such, provides a normal form for any autonomous oscillations close to onset. As a new fundamental equation of physics, the CGLE is able to sustain a large variety of common patterns and is one of the most well-known and thoroughly described RD-like systems [27, p. 367] in 1-dimension. The simple instabilities of regular structures are well known in 2D but the STC states resulting from spiral breakup have only been investigated in a few studies [38, 105, 106, 81, 45] and the initial apparent universal agreement of the statistical properties of DMT in the CGLE with Gil *et al.*'s simple statistical model introduced in section 1.4 (henceforth also refereed to as the null model), and the applicability of that model to other systems and in experiments, has been eroded sufficiently from all sides. From one side, it has been shown that, even when the creation and annihilation rates of defects satisfied the simple rate model, their underlying fluctuations are not universal and can be vastly different depending on the particular regime and other details of the dynamics, varying from a purely random process to one with a high degree of correlation [35]. On another side, it has been shown that even the CGLE does not always satisfy the defect distributions predicted by the null model [45] (see Section 1.4 for the description of the null model), a fact that had apparently been overlooked for more than a decade, although the rate model can easily be extended to describe such deviations. Many experimental studies also concluded that the observed rates did not obey the null model rates [24, 45, 107]. While some deviations could be accounted for by trivial boundary effects [42] and the presence of noise [44], it became clear that a

new, more general and accurate, description of DMT is direly needed if only to organize the multitude of observations of DMT into a unified framework.

3.1.1 Description of the model

The CGLE describes the time evolution of the complex amplitude field $A(\vec{r}, t)$ according to

$$\partial_t A(\vec{r}, t) = A + (1 + ib)\nabla^2 A - (1 + ic)\left|A\right|^2 A \tag{3.1}$$

where b and c are real numbers. Its phase diagram, shown in Figure 3.1, is well known in 1D and 2D [106] though much less in 3D [108], but still significantly more than any other systems. The Benjamin-Feir (BF) instability in Figure 3.1 corresponds to the convective instability of long wavelength oscillations and is benign in this case. The region between the onset of DMT (due to a convective Eckhaus instability) and the absolute 2D Eckhaus instability (EI) corresponds to a region where a stable spiral state coexists with DMT. This bistability means that a stable spiral can be maintained up to the absolute EI if the control parameter is changed adiabatically [109], though this is extremely difficult in practice. At $b = 5.0$ and below $c_{\text{onset}} = -0.69$, we found empirically that the turbulent state could be maintained indefinitely (as long as we simulated), whereas for greater values of c, the stable spiral will re-invade the medium after a possibly extremely long transient and turbulence will be lost. This marks the onset of DMT in the CGLE. All numerical integrations in 2D have been performed on an $N \times N$ periodic lattice corresponding to an $L \times L$ square with a simple mid-point explicit method using a 5-point Laplacian with a maximum Δx and Δt of 1.0 and 0.005 respectively. Such a low Δt (with respect to what would be needed for the numerical stability of the solution) was necessary to resolve precisely the defect events due to the incredibly high activity of defects. The numerical results have also been tested for convergence for $\Delta x = 0.5$ and found to not vary significantly. The algorithms used for all simulations, as well as the typical initial conditions, are described in Appendix A. Figure 3.2 shows three representation of a snapshot of the solution at $(b, c) = (5.0, -0.7)$ with defects superimposed.

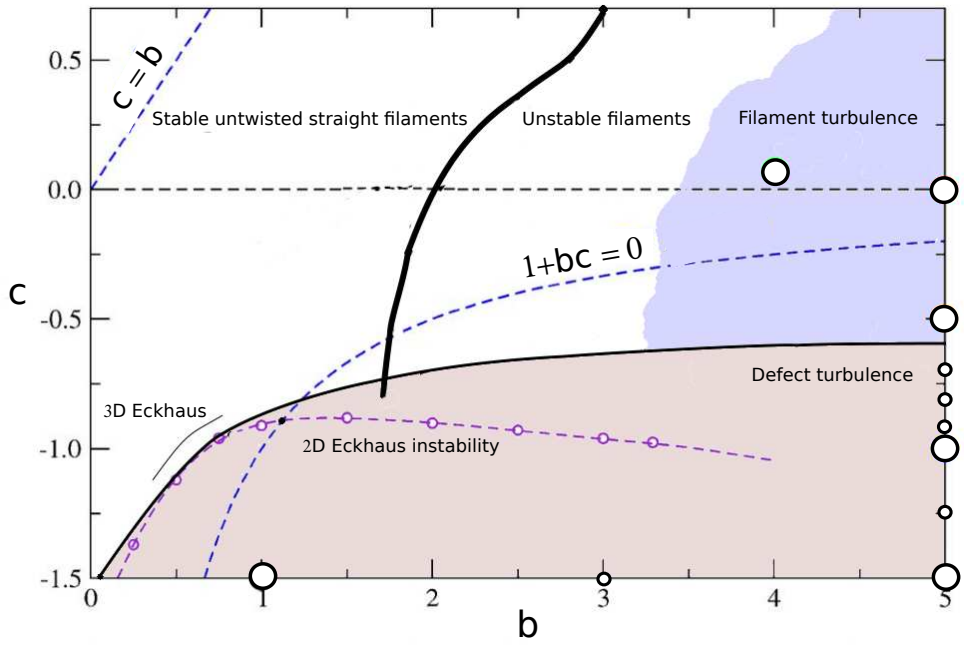

Figure 3.1: 2D and 3D phase diagram of the CGLE (Adapted from Ref. [108] in accordance with AIP's CC BY 3.0 licence). The thin black line represent the onset of defect turbulence in 2D and the Eckhaus instability marks the region where the plane wave emitted by the (unstable) spirals are absolutely unstable. The thick black line represent the instability line of straight untwisted filaments which will become important in the Chapter 4. This means that straight filaments to the right are unstable and the perturbation saturate to different structures e.g. helix, superhelix, etc. The instability lines are yet not exhaustive. For instance, it is not clear exactly where the onset of 3D filament turbulence lies which is why this region is left purposely vague. The shaded regions correspond to the region of amplitude turbulence (pale pink) and the suspected region of filament turbulence (pale blue). The small black circles mark the values we have used in our 2D simulations and the big black circle where we have simulated in 2D and 3D.

3.1.2 Defect statistics

The region of DMT in the phase diagram of Figure 3.1 has been dubbed amplitude turbulence (AT) due to the apparent passive role of defects — defects are not the center of well-defined local spiral structure, they are merely advected randomly from the fluctuation of the field [109]. However, the rates are nonetheless observationally different from the null

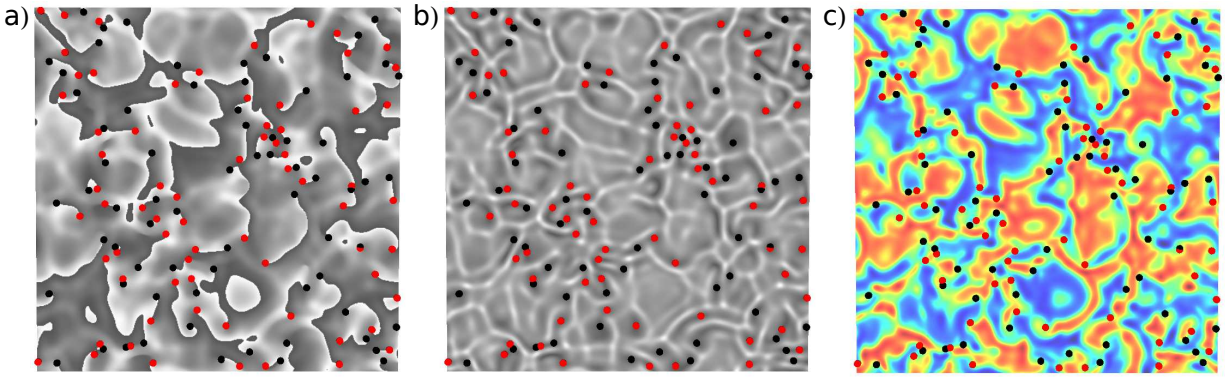

Figure 3.2: Three representations of a still frame of the defect turbulence close to onset at $(b, c) = (5.0, -0.7)$ with defects superimposed. The system size shown is $N = 512$ with $L = 256$. a) Phase $\phi(\vec{r}, t)$ of $A(\vec{r}, t) = R(\vec{r}, t)\mathrm{e}^{i\phi(\vec{r},t)}$. b) Amplitude $R(\vec{r}, t)$ and c) $\mathrm{Re}\,[A(\vec{r}, t)]$. There appears no clear structure around the defects in either representations. The defects were identified with the bilinear interpolation of isolines method discussed in Section 2.2.1.

model rates in an essential way: they acquire a significant linear contribution close to onset of the spiral instability as seen on Figure 3.3b. For instance, at $(b, c) = (5.0, -0.7)$ (sample frame with corresponding defects shown on Figure 3.2), we measured $\bar{c}_0 = 0.24 \pm 0.02$ and $\gamma_n = 1.68 \pm 0.06$. Very close to the transition, just above $c \approx c_{\mathrm{onset}}$, one can observe that spiral waves may re-form spontaneously in an initially random AT field and have a stabilizing effect on the global pattern, whereas the defects in the AT regime appear to have a destabilizing effect according to the form of the rates. In other words, from a turbulent initial condition above c_{onset}, a spiral glass state may form spontaneously after a long turbulent transient. Below c_{onset}, the transient may be too long and only the turbulent state was observed. The linear contribution to the creation rate appears to recede as we move farther away from the onset of 2D turbulence, as shown in Figure 3.3b. The variation appeared gradual across the 2D EI and some variability remains even after the onset of this instability. These results are consistent with the shape ratio γ_n of the distributions of defects observed in the CGLE made in Ref. [45] and further specify the deviations as resulting primarily from a linear plus constant creation rate of defects.

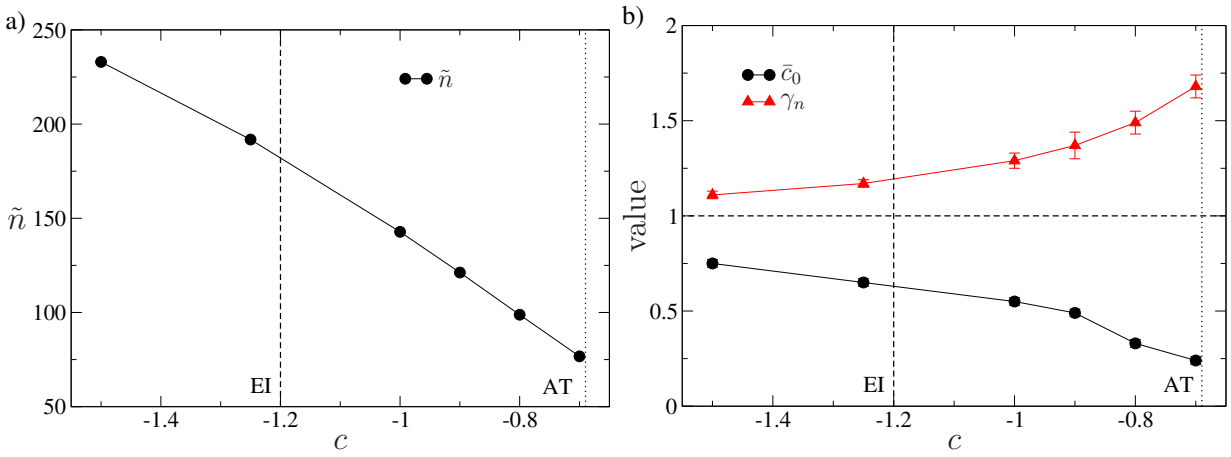

Figure 3.3: Average number of defects and rates in the CGLE. a) Normalized average density of defects $\tilde{n} = \langle n \rangle \times 256^2/L^2$ at $b = 5.0$ with varying c in a system of size $L = 256$ with periodic BCs. b) Shape factor γ_n of the distribution of defects and normalized constant creation rate component $\bar{c}_0$ over the same parameter regime. The horizontal dashed line indicates the expectation from the null model and the vertical line represent the onset of DMT (AT in this case) and the EI as shown in Figure 3.1.

3.1.3 Spacetime loop statistics

Figure 3.4 illustrates the typical spacetime loops cluster size (n-span) and lifetime (t-span) relative frequency distributions or probability density functions (PDFs). The t-span PDF scaling for long spacetime loops all appear to be close to $\gamma + 1 = 3.0$.[1] The n-span PDFs appear completely independent of the regimes which confirms and extends the observations of the quasi universality of the n-span scaling in Ref. [45]. The particular scaling of the n-span PDFs, which covers almost the whole range of n-span very accurately up to the cutoff (the boundary condition changes the behavior of the cutoff, but the scaling property remains), implies that a large fraction of defect pairs self-annihilate. Indeed, according to the estimation of the exponent of the PDF of cluster sizes, we expect that the relative fraction of defect loops with n-span = 1 is

$$\frac{n_1}{n_\infty} = \left(\sum_{n=1}^{\infty} n^{-2.6 \pm 0.1} \right)^{-1} \approx 0.77 \pm 0.02, \tag{3.2}$$

[1] $\gamma + 1$ was defined in Section 2.6.4 as the power law scaling of the tail of the PDF of t-spans of defects. There is no theory that predict these exponents [45] such that any apparent scaling is still purely empirical.

where $n_N = \sum_{n=1}^{N} p_{\mathrm{n}}(n)$ is the cumulative sum of n-span up to n-span = N. Therefore, roughly 77% of defects should annihilate with the same anti-defect partner. In fact, the relative frequency of n-span = 1 loops is even higher at around 85% in this case due to the "flaring up" of the measured n-span distribution at n-span = 1 as shown on Figure 3.4. Incidentally, these scaling laws can be reproduced fairly well by a simple model of bipartite random walkers that are created pairwise close together at a constant and uniform rate [81]. The collision of defects and anti-defects (within a certain radius) corresponds to an annihilation event and the populations of random walkers naturally settles around an average value. Such a model not only reproduces[2] the t-span and n-span distributions observed above, but also produce an annihilation rate which is proportional to the square of the number of walkers, as implied by the mean field approximation in the null model, to an extreme degree of accuracy (This is, again, an experimental agreement). The large amount of self-annihilation, which the mean field approximation could not have predicted, is then explained entirely by the defects not moving far apart upon creation (which is the opposite of what was assumed in the mean field theory!), making them very much more likely to annihilate immediately than to move far away, without resorting to an explanation that involves extraneous correlations. However, insofar as we know, such a random walker model only reproduces the null model's gross statistical features and does not explain the apparent universality of the scaling exponents found in the CGLE in this section.

3.1.4 Discussion

The results we have presented show the great variability of the statistical features of DMT in the CGLE. A master equation model of defects can still be applied to all cases, but we do not possess a more profound understanding than the author that came before us [38, 42, 24]

[2]The random walker model reproduces only the qualitative behavior i.e. the apparent power law. The values of the critical exponents appear to vary. In particular, the scaling of the n-span distribution has been evaluated at $\alpha+1 = 2.6$ while the scaling of the t-span appeared to vary between $2.4 \leq \gamma+1 \leq 2.6$ depending on the details of the construction of the model.

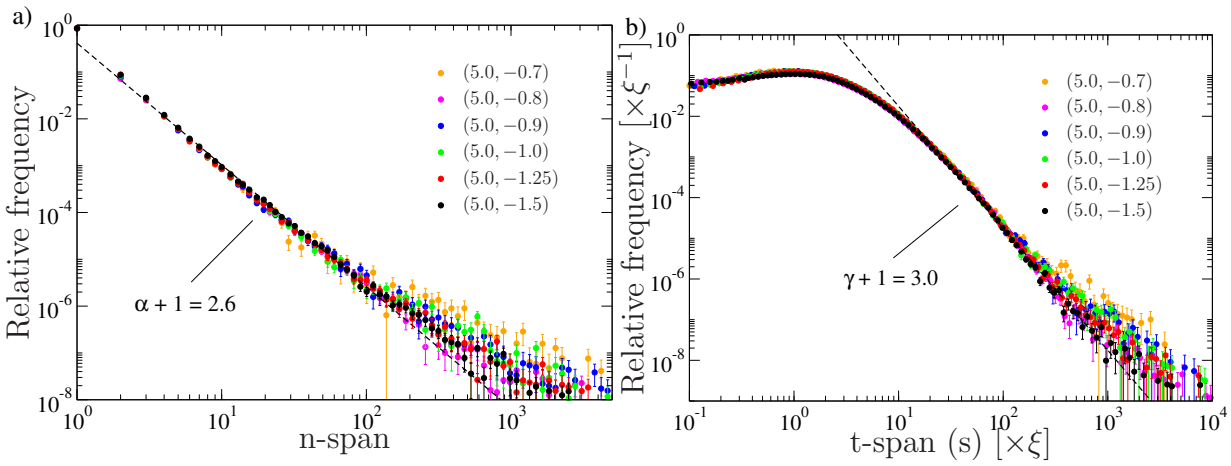

Figure 3.4: Spacetime defect loop distributions in the CGLE. Both the t-span and n-span appear very well conserved as the parameter is varied from onset ($c_{\text{onset}} \approx -0.69$) of AT to far into the AT regime ($c = -1.5$). The n-spans are shown "as is" but the t-spans have been rescaled to collapse by an empirical factor of $\xi = 1 + 2\,|\Delta c|$ where $\Delta c = c - c_{\text{onset}}$.

in regard to the connection between the states. In particular, why are the defect rates close to onset of DMT apparently marked by a self-enhancing term (linear creation rates) in this case? One possibility is that the defects have an intrinsic destabilizing effect on the field causing the multiplication of high phase gradients, and hence the further creation of new defect pairs. Far from onset, the random fluctuations of the field may be so strong that the destabilizing effect of spiral structures is small by comparison, hence recovering an almost constant creation rate. Pursuit of these hints would likely require a way to quantify the amount of instability in the field and a description that relates the statistical description of defects back to the field description.

However, even purely experimental insight can be useful. For instance, Ref. [110] shows a theoretical investigation of a CO oxidation on Pt(110) model[3] where defect rates were found to deviate significantly from those of the null model. The authors also clearly state that their results contrast with the defect statistics in the CGLE. However, their results cannot be said to deviate from the CGLE from the observation of deviations from the null

[3]Pt(110) is a certain surface configuration of a platinum crystal lattice [111].

model since the CGLE rates deviate from the null model rates in some cases already. In a related experimental study [24], the presence of strong short range correlations between defects has been linked to the large amount of self annihilated defects (n-span = 1). This self-annihilation of defects was then invoked to account for the different linear plus quadratic annihilation rate observed in this experiment — a population of self-annihilating defect *does* have a linear annihilation rate when conditioned on the number of such defects. However, our measurement of n-span in many regimes shows that this argument must be flawed because self-annihilating defects are always dominant by a large amount, even for a purely random process with quadratic annihilation rates. Indeed, we expect around 77% of defects that self annihilate in such a case, which is even higher than the roughly 50% reported in Ref. [110] in a model description of the previous experiment. Lower values of the relative frequency of n-span = 1 loops are not surprising if the defects detected were subject to some form of filtering. Therefore, hypotheses on the cause of defect rate correlations based on the defects alone can be misleading and we believe that the correlations cannot be understood without further information about the underlying patterns.

Another clarification we are trying to make here, which may have been obvious from the start[4], is that the null model is not a model of DMT in the CGLE, it was a model of DMT checked for validity in the CGLE [38]. The CGLE happens to have regimes that agree well with these simple rates, but it also has regimes that do not. The regimes that agree best all appear to be sufficiently far from onset of the spiral instability. Incidentally, this also means that a more in-depth study of the CGLE may be able to clarify the basic processes and relations between the field and defect dynamics that are behind these deviations, a fact that had been hitherto obscured by the absence of high resolution observations of DMT in simulations[5].

[4]It is only made obvious by high speed computations and highly accurate statistical measures. Without those, every detail and deviation from the null model fell within the error of the estimates.

[5]For instance, in a section on DMT in a recent textbook [70], we can only find the description of Gil *et al.*'s model of DMT in relation to DMT in the CGLE and a few lines mentioning the effect of boundaries and noise — as if the model had universal applicability in that case. The applicability of the null model to

3.2 The Peroxidase-Oxidase Model

A secondary Hopf bifurcation is a common occurrence in many homogeneously oscillating media, yet, the secondary frequency is often not in a 2:1 resonance with the first frequency — which would correspond to a period-doubling — but the dynamics is instead quasiperiodic and forms a torus in phase space as, for example, in the Belousov-Zhabotinsky reaction [112, 113] or in the electrodissolution of copper in an acidic chloride solution [114]. Quasiperiodicity has also been found in chemical reactions of biological relevance such as the peroxidase-oxidase reaction [115, 116, 117] and the glycolytic reaction [118, 119]. The dynamics of the peroxidase-oxidase reaction is of particular biological relevance since this enzymatic reaction plays a prominent role in the signaling pathway of white blood cells [120, 121]. One important aspect of quasiperiodicity is that it generically leads to chaotic behavior as formulated by the Ruelle-Takens-Newhouse theorem [122] and experimentally observed in the above chemical reactions. Furthermore, quasiperiodic behavior has been proposed to play an important role in the route leading to STC in the form of ventricular fibrillation in the heart [123].

Therefore, we set out to investigate a particular system, a simplified spatially extended peroxidase-oxidase (PO) model, since unlike the case of a primary Hopf bifurcation, there is no unique normal form for a secondary one that would provide for a more general workbench for the study of such a bifurcation[6]. The normal forms of a secondary Hopf bifurcation that we tested [124, 125, 126] were unable to generate stable spiral waves when the corresponding systems of ordinary differential equations were extended by addition of a diffusion term. Since the formation of spiral waves is a general feature in *real* oscillatory and excitable spatially extended media, our model ought to represent this fact. In particular, we were interested in knowing if we could observe a different turbulent regime like what was discovered

the CGLE had also been erroneously assumed by many other authors, ourselves included.

[6]It is important to realize that there is no general normal form for the torus bifurcation in spatially extended systems which would be analogous to the CGLE — the normal form of simple oscillatory media [106].

in the aforementioned period doubling case. However, we found that the secondary Hopf bifurcation almost immediately promoted a turbulent state analogous the defect turbulence observed in the CGLE. Indeed, this turbulent regime, as characterized by the rates, was indistinguishable from the rates far from onset in that model. However, many other measures yielded deviations from what would have been expected in this case. This further emphasized that the rates in defect turbulent regimes are not necessarily the only relevant indicator of the dynamics. In fact, even though they carry some information about the dynamics, it is fairly clear that they offer only an incomplete picture and that the behavior of the surrounding field and/or other properties of the defects also carry some information.

3.2.1 Description of the model

We consider the two-dimensional reaction-diffusion medium described by the following equations

$$\begin{aligned}
\partial_t A &= k_7 - k_1 ABX - k_3 ABY - k_{-7} A + D\nabla^2 A, \\
\partial_t B &= k_8 - k_1 ABX - k_3 ABY + D\nabla^2 B, \\
\partial_t X &= k_6 + k_1 ABX + 2k_3 ABY - 2k_2 X^2 - k_4 X + D\nabla^2 X, \\
\partial_t Y &= 2k_2 X^2 - k_3 ABY - k_5 Y + D\nabla^2 Y,
\end{aligned} \tag{3.3}$$

where $A(\vec{r},t)$, $B(\vec{r},t)$, $X(\vec{r},t)$ and $Y(\vec{r},t)$ are the time-varying concentration fields of the various reactants in the peroxidase-oxidase reaction as modeled in Ref. [127] based on mass action kinetics. Other more realistic and detailed models for this reaction have also been proposed, e.g. Refs. [116, 128, 117], but we focus here on the former because of its numerical simplicity. Since it is used as a paradigmatic model, we do not intend to set the parameters to physically plausible values but only to emphasize the quasiperiodic features of the bifurcation (e.g. large amplitude difference and regularity a.k.a. a "fat" torus). Nevertheless, A and B represent the dissolved O_2 and NADH concentrations, respectively, while X and Y are reaction intermediates [115]. The parameters k_i are rate coefficients that contain the

concentrations of the pool species that are fixed to maintain the system out of equilibrium and D is the diffusion constant. For simplicity, we assume it to be the same for all four chemicals. The reaction dynamics by itself crucially depends on the values of the k_i's. In Ref. [115], quasiperiodic behavior was found over a range of parameter values similar to what has been observed experimentally. Here, we chose $k_2 = 1250$, $k_3 = 0.046875$, $k_4 = 20$, $k_5 = 1.104$, $k_6 = 0.004$, $k_7 = 0.8$ and $k_{-7} = 0.1175$. Since k_8 depends on the (constant) inflow of one of the chemical reactants (NADH), it can be easily adjusted in an experiment. Similarly, k_1 is thought to correspond to the enzyme concentration which also can be controlled experimentally. Figure 3.5a shows the phase diagram of the reaction dynamics in the k_1–k_8 plane. Indeed, the dynamics shows quasiperiodic behavior as indicated by the torus attractor in phase space (Figure 3.5b). In order to ensure a well-developed torus in the reaction dynamics, we chose $k_1 = 0.13$ and use $k_8 = \lambda$ as our control parameter in the following. The diffusion constant, largely arbitrary, was set to $D = 1$ and the system size was chosen as a square region of side-length $L = 400$ with a spatial interval $\Delta x = 2$ unless stated otherwise.

Eq. (3.3) was numerically integrated using a simple forward Euler scheme with a 9-point Laplacian. The time interval $\Delta t = 0.005$ was chosen for stability reasons and necessity due to the stiffness of the dynamics. Varying λ over the interval $[0.48, 0.58]$ as shown in Figure 3.5a, we investigate the existence and stability of spiral waves. The bifurcation diagram for the reaction dynamics suggests that values of λ in the simply oscillatory regime should yield regular spiral waves. Indeed, for $\lambda = 0.480$, single spiral waves are stable in a medium with no-flux boundary conditions as seen in Figure 3.6a. Taking this spiral wave concentration profile as the initial condition, λ was gradually incremented and a long equilibration time was allowed for the dynamics to reach the new system state at each new value of λ. We observe that a stable spiral pattern can be maintained up to $\lambda \approx 0.505$. For higher values of λ, the single spiral pattern becomes unstable [7] and the medium shows DMT behavior as

[7] The spiral core does not show any pronounced motion at the transition point indicating that the breakup

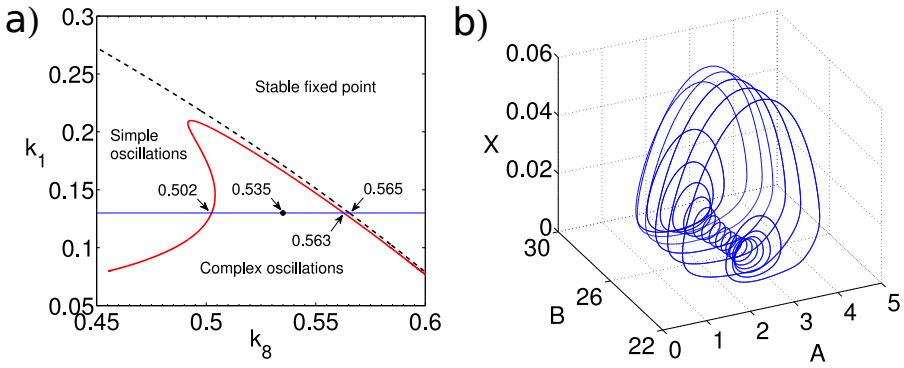

Figure 3.5: a) Bifurcation diagram of the reaction dynamics ($D = 0$) given in Eq. 3.3 obtained using the continuation software AUTO [129]. The dashed line corresponds to the first Hopf bifurcation while the solid line corresponds to the second Hopf bifurcation. In the following, $k_8 = \lambda$ is varied along the horizontal line from the simple oscillatory region on the left to the complex oscillatory region which is dominated by intertwined periodic and quasiperiodic regimes reminiscent of Arnold tongues [122] but also seems to contain some values in the interval $0.55 < \lambda < 0.562$ with a significantly positive maximal Lyapunov exponent (of the order of $10^{-3} \pm 10^{-6}$). The precise values for the bifurcation of the reaction dynamics are indicated along the line. b) Typical toroidal attractor in the complex oscillatory regime at $\lambda = 0.535$.

indicated by the continuous creation and annihilation of additional spiral cores [8].

A snapshot of the DMT dynamics is shown in Figure 3.6d for $\lambda = 0.535$. Note that the dynamics is also characterized by short-ranged spatial correlations — see Figure 3.6c — which is another hallmark of DMT [35]. In the turbulent regime, the local dynamics is still strongly dominated by the frequencies of the homogeneous system — see Figure 3.6b. The turbulent dynamics persists until $\lambda \approx 0.562$. For larger values of λ, the local dynamics converges toward a fixed point and any trace of spatiotemporal turbulence rapidly dies out [9].

The topological phase defects were identified and tracked using the method developed in

is due to a far-field instability, i.e., the wave train becomes unstable.

[8]Close to this transition ($0.505 < \lambda < 0.520$), a careful analysis of the time series of the total number of spiral cores shows that the turbulent dynamics typically has very long transients and may eventually settle on a frozen multispiral state i.e. no DMT.

[9]Note that in the regime of defect-mediated turbulence the initial conditions do not play a significant role as long as they are sufficiently far away from the homogeneous state. For initial conditions close to the homogeneous state, we find that the dynamics will converge toward homogeneous quasiperiodic oscillations. Thus, the medium is bistable.

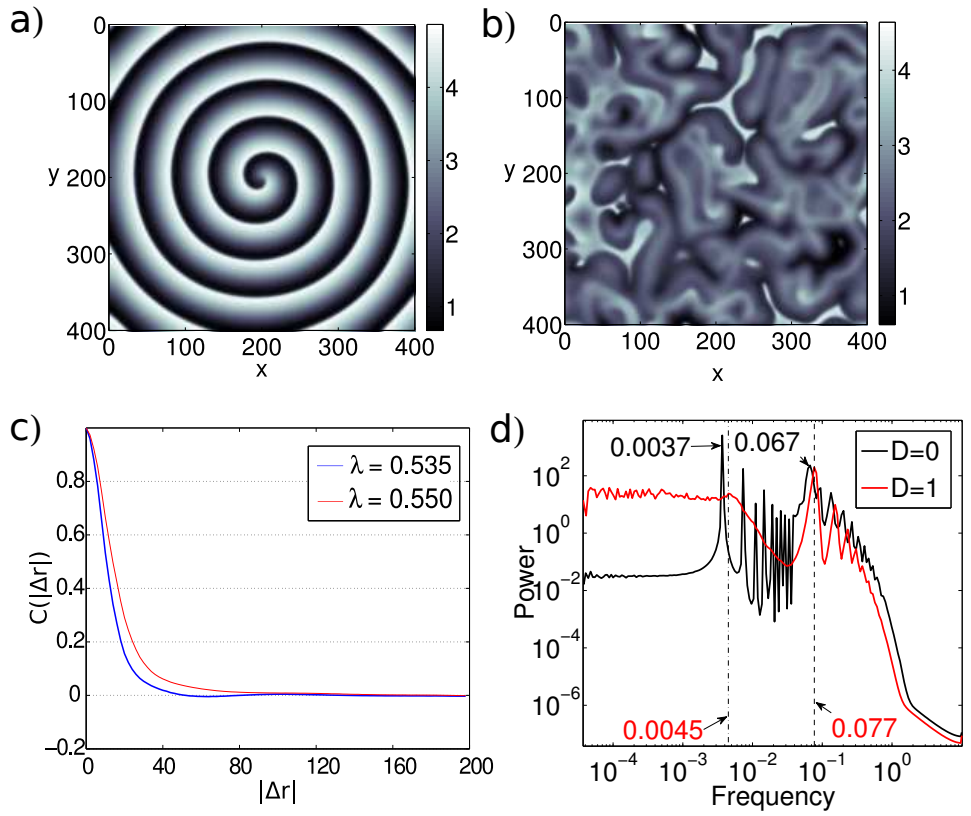

Figure 3.6: a) Spiral pattern as seen in $A(\vec{r},t)$ for $\lambda = 0.480$ where the dynamics is simply oscillatory. b) $A(\vec{r},t)$ in the turbulent regime for $\lambda = 0.535$ with periodic boundary conditions. c) Correlation function of $C(|\Delta\vec{r}|)$ of the A-field given in Eq. (3.3) at two values of the bifurcation parameter. d) Power spectrum of the time series $A(t)$ for the reaction dynamics ($D = 0$) and for a single point of the spatially extended system ($D = 1$) at $\lambda = 0.535$. The two periods — indicating quasiperiodic behavior — are easily identifiable in both power spectra. Note that the dominating peak for the spatially extended system is the spiral frequency corresponding to a period $T_{\text{spiral}} = 13$. The second period is $T_2 = 220$.

chapter 2 with phase defined as

$$\phi(\vec{r},t) = \tan^{-1}\left(\frac{\partial_t X(\vec{r},t)}{\partial_t A(\vec{r},t)}\right). \tag{3.4}$$

Detailed numerical simulations and inspections proved that this definition of a phase is indeed very efficient and accurate. However, note that due to the imperfection of the phase (the possibility of not having a homomorphism over a small angle) typically arising as a discretization effect, spurious defect pairs of opposite topological charge can occasionally be detected. They are short-lived and generally directly adjacent to one another on the discrete

lattice[10]. Therefore, a numerical remedy to this problem is to remove all defect pairs of opposite topological charge which are detected within a small radius of each other. This will have no effect on the genuine creation events since these will separate and still appear in the time series. We have verified numerically that this procedure does not affect any of our statistical results by considering different values of Δx (e.g. by halfing Δx and doubling the number of nodes).

3.2.2 Defect statistics

Figure 3.7 shows the result of the application of the defect detection algorithm for a small spacetime region for a selected number of defects. There are at least three common behaviors for the defect dynamics: 1) Fast meandering and creation/annihilation recurrences of defect pairs corresponding to $T_{\text{spiral}} \approx 13$ predominantly located at shock lines (trajectories #1 — recurrence indicated with arrows). 2) Longer lived bounded pairs forming small loops over a maximum of a few spiral rotations such as loop #2. 3) Free defects persisting over a long time scale ($> T_2$) such as trajectory #3 and potentially forming very large loops over the whole system size. Our results for a specific value of λ are presented in Figure 3.8 which — within the statistical and systematic uncertainty of the estimates — agree well with the behavior described by the null model of DMT. Different values of λ give similar results although the average number of defects sustained by the medium can vary drastically. In particular, the number of defect pairs tends to be vanishingly small as λ reaches the secondary Hopf bifurcation on the right along the line in Figure 3.5.

To characterize the DMT state further, one can consider higher-order statistics. It has already been pointed out that spatially extended media with different local dynamics can exhibit quite different correlations in the time series of the number of defect pairs $n(t)$ despite obeying the same squared poissonian distribution of the number of defect pairs [35].

[10]Note that our latter, preferred, detection method described in chapter 2 made defects free of the lattice of the simulation. However, this sort of phase definition issue can still be a problem and one has to be very careful either way.

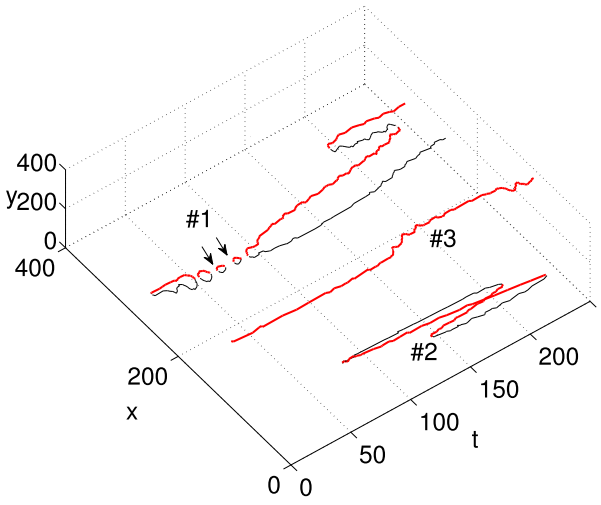

Figure 3.7: Space-time view of the defects in the peroxidase-oxidase model for $\lambda = 0.535$. Only a few selected trajectories are shown for clarity. In contrast to what the projection might suggest, the motion is *not* confined to the x-direction. The time length of this sample is a bit longer than the longest period of the dynamics $T_2 = 220$ (see Figure 3.6b). The colors correspond to different topological charges (-1 in thick red, $+1$ in thin black).

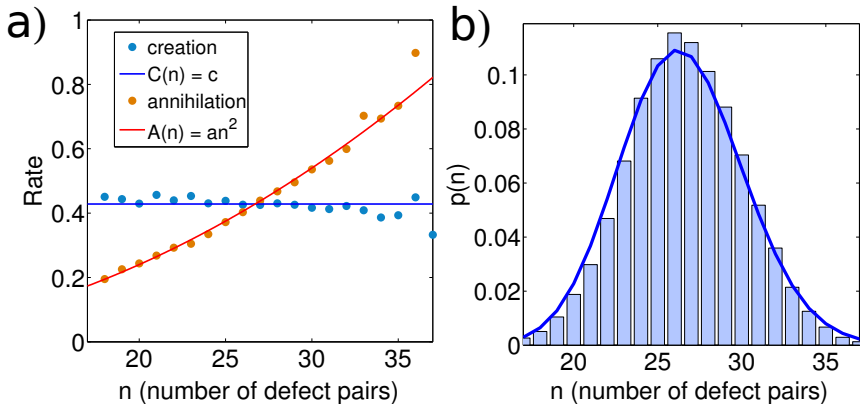

Figure 3.8: First order statistics of the defects at $\lambda = 0.535$. a) Creation (in blue) and annihilation rates (in red). Best fitting of the data reveals a creation constant $c \approx 0.42$ and an annihilation constant $a \approx 6.0 \times 10^{-4}$ for an average number of defects of $\langle n \rangle = \sqrt{c/a} \approx 26$. b) Relative frequency of the number of defects shown together with the squared poissonian distribution that one would obtain using the best fits obtained in (a).

In our case, Figure 3.9a shows that the power spectrum of $n(t)$ has a Lorentzian shape apart from a small deviation peak at a frequency that coincides with the spiral frequency f_{spiral}.

This characteristic frequency of creation/annihilation recurrences can be directly observed in Figure 3.7 and was fairly frequent in our simulations. The fact that the overall shape is Lorentzian implies that the *remaining* correlations in $n(t)$ can't be distinguished from those of a simple stochastic process where the fluctuations in the number of defect pairs arise from independent random events.

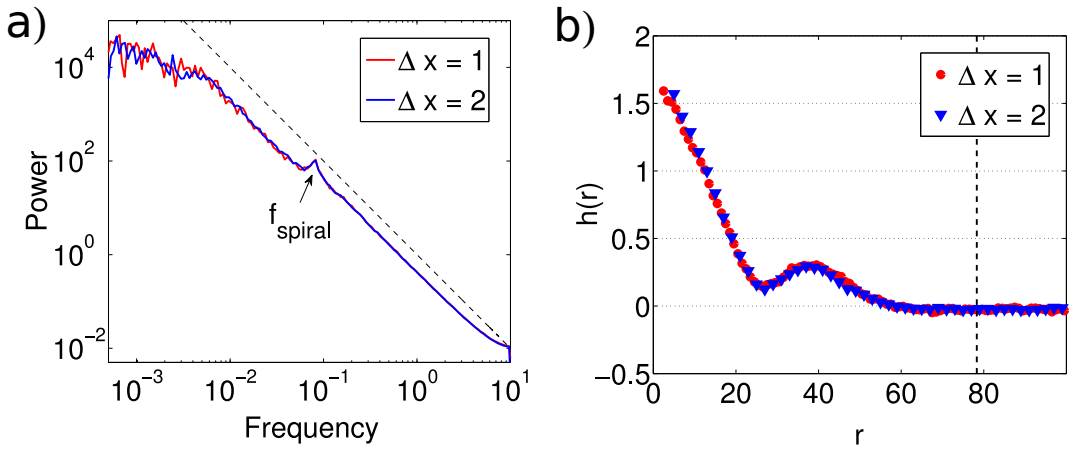

Figure 3.9: a) Power spectrum of the time series of the defects which scales as f^{-2} as indicated by the dashed line. The "anomalous" frequency peak at $f = 0.077$ corresponds to the spiral frequency. b) Pair correlation function of the defects at $\lambda = 0.535$ for system size $L = 400$ and different Δx. The black dashed vertical line indicate the characteristic length $r_0 = \sqrt{L^2/\langle n \rangle} \approx 78$ of the system.

This does, however, not imply that the motion of a single defect is independent of the motion of other defects. To demonstrate this, we calculated the normalized pair correlation function for oppositely charged defects, which is defined in section 2.6.1. Figure 3.9b shows that in the defect mediated turbulent regime, the pair correlation function has two pronounced peaks. In contrast to other models such as those studied in Refs. [78, 35], the peak at smaller distances dominates indicating that defects of opposite topological charge often stay close to one another. This is the case for the short-lived defect pairs which are periodically generated. The peak at larger distances corresponds to weakly bound pairs which are not periodically generated and, thus, indicates a certain degree of non-trivial correlations in the defect dynamics. We observe that the exact ratio of these two types of bound pairs

varies with λ leading to varying peak sizes in the pair correlation function. In particular, numerical results suggest that the short distance peak increases monotonically as we move away from the bifurcation point, at least up to $\lambda = 0.550$.

3.2.3 Spacetime loop statistics

Following the approach of characterizing spacetime defect loop statistics introduced previously, we study two statistical characteristics of the loops: the lifetime (t-span) and the cluster size (n-span) of spacetime defect loops. For example, in Fig 3.7, loop #2 contains 2 visible pairs of trajectories and its t-span is roughly 175. Only the loops that were created and closed during the simulation were counted in the statistics. Hence, we only considered complete defects loops. The normalized relative frequency distributions or probability density functions (PDFs) $p_{\mathrm{t}}(t)$ and $p_{\mathrm{n}}(n)$ of the t-span and n-span, respectively, for $\lambda = 0.535$ are presented in Figure 3.10.

The most striking feature of the PDF of the t-span is that some intermediate t-spans are much less likely than other. Incidentally, the t-spans that are less likely to occur correspond to integer multiples of the period of the spiral in the medium. As observed in Figure 3.7, one spiral period separates the creation of one of the small loops to the creation of the next, leaving the effective time length of these loops to roughly half the spiral period. This is simply another aspect of the recurrence observed in the power spectrum in Figure 3.9a. For longer t-spans, the PDF of the t-span decays as a power law with critical exponent $\gamma + 1 \approx 3.0$. While such power-law decay has been reported in various models and in an experiment of undulation chaos [45, table 1], the exponent is relatively high in the range of reported values but consistent with our value measured in AT for the CGLE in section 3.1.3.

The PDF of the n-span, on the other hand, seems to yield a simple power law scaling with exponent $\alpha + 1 \approx 2.6$. The agreement with other values of $\alpha + 1$ found in different systems and regimes is quite remarkable. The strongly bound defect pairs involved in the recurrence phenomenon, and any artifactual defects, most likely all have n-span = 1 and,

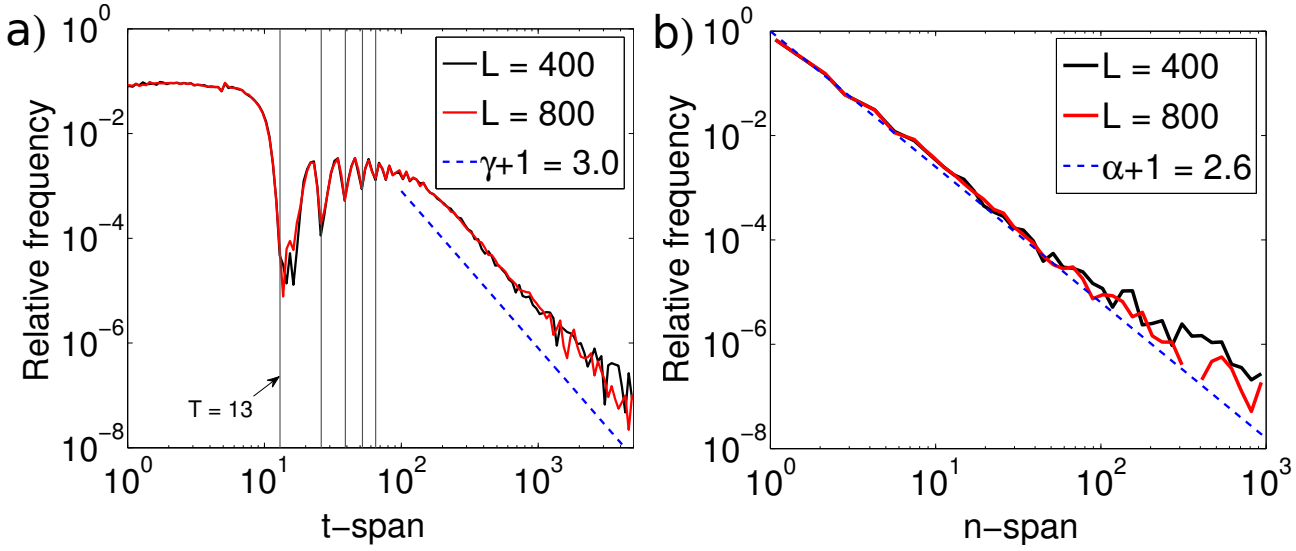

Figure 3.10: Statistics of defect trajectories. a) Relative frequency distribution of the time span of the loop in the peroxidase model for two sizes of the system. The fundamental period of the attractor T_{spiral} as well as the four successive multiples are displayed. For large time spans the distribution follows a power law with an exponent $\gamma + 1 \approx 3.0$. b) Relative frequency distribution of the number of defect trajectories per loop. The distribution scales with an exponent $\alpha + 1 \approx 2.6$. The deviations at large arguments are due to poor statistics.

as a result, these short time scale loops cannot really influence the scaling of the n-span distribution as a whole — in fact, in our results, they are consistent with the scaling i.e. that even n-span = 1 appears captured by the power law. The PDF of the n-span also allows us to estimate the likelihood of an annihilation event in which the partners were also created together. We find that about two-thirds of all annihilation events are of this type for $\lambda = 0.535$. This is consistent with the power law scaling of Eq. 3.2 and with the existence of a large number of bound pairs as quantified by the pair correlation function — see Section 3.2.2 for a discussion.

3.2.4 Discussion

We have shown that a system with a local *non-resonant* secondary period can promote a state of DMT. While all first order statistics of defects are similar to those of DMT regimes

in simple oscillatory media far from onset, almost all second order statistics investigated showed significant, non generic, deviations. More surprisingly, the shorter period of the local attractor seems to play a critical role in the time span of the defect loops, an effect which has not been reported until now. Our findings indicate that while certain characteristics of the dynamics of the defects can be idiosyncratic, other may be linked to specific, potentially generic, characteristics of the local attractor. This may be tested experimentally on systems like the peroxidase-oxidase reaction whose local dynamics is quasi-periodic in certain parameter regimes.

One thing that, in hindsight, appears to be missing in this analysis is a characterization of the turbulence as the control parameter is moved closer to onset (of the spiral instability and closer to the Hopf bifurcation). The main problem was that, at the time, we were also trying to assess our methodology and the statistics close to onset were too scarce to yield any reasonable results due to the typical spatial dilation of the dynamics close to onset of oscillations. Therefore, we abandoned the idea of a detailed characterization of these regimes. On the other hand, the rate statistics that we observed in the peroxidase model were typical (though not defining) of DMT regimes and a thorough analysis close to onset of the supercritical Hopf bifurcation in the peroxidase model is likely to simply show more of the same. In any case, the identical defect n-span distribution scaling and comparable scaling exponent of the tail of the lifetime (time-span) distribution seem to argue that there isn't a fundamental difference between the defect dynamics in simple oscillatory media far from onset and this quasiperiodic medium as far as the statistical measures of the defects are concerned — both DMT are maintained by a process that essentially depends on the local amount of instability in the field [38] such that the defects are merely passive objects.

3.3 The modified Bär model

DMT is, of course, not limited to oscillatory media. However, there are no normal forms of excitable oscillations because the amplitude formalism needed for such a description cannot apply in a case where the main attractor (the rest state in these cases) is stable. Nevertheless, there are models which have established themselves as paradigmatic models of excitable media (without being universal in any sort of way) due to their fundamental simplicity and the wealth of phenomena they reproduced. The Bär model, introduced as a simplified model of the CO oxidation of Pt(110), is such a model [130]. Here, we consider a modification of the Bär model that has certain desirable properties in three dimensions which will become important in Chapter 4.

3.3.1 Description of the model

In the following, we consider a slightly modified version of the Bär model [130], a Fitzhugh-Nagumo type model which is a paradigmatic model for fast activator/slow inhibitor excitable media. It is described by the system of coupled PDEs given by

$$\begin{aligned} \partial_t u &= \frac{1}{\varepsilon} u(1-u)\left[u - \frac{v+b}{a}\right] + D_u \nabla^2 u \\ \partial_t v &= f(u) - v + D_v \nabla^2 v \end{aligned} \tag{3.5}$$

with

$$f(u) = \begin{cases} 0, & u < \frac{1}{3} \\ 1 - \frac{27}{4} u(u-1)^2, & \frac{1}{3} \leq u \leq 1 \\ 1, & u > 1 \end{cases} \tag{3.6}$$

where u corresponds to the activator, v is the inhibitor species, D_u and D_v are the respective diffusion constants and a, b and ε are parameters. This form of $f(u)$, compared to $f(u) = u$ in the Barkley model [131], results in a delayed inhibition which produces new instabilities leading to spatiotemporal chaos in 1D and 2D. We defined $e \equiv \varepsilon^{-1}$ as the relative timescale between fast activation and the slow inhibition which can be roughly interpreted as the

excitability of the medium [130]. While in the original Bär model $D_u = 1$ and $D_v = 0$, here we consider the case $D_u = D_v = 1$. All numerical integrations in 2D have been performed on an $N \times N$ lattice corresponding to an $L \times L$ square with a simple mid-point explicit method using a 5-point Laplacian with a maximum Δx and Δt of 0.4 and 0.01 respectively. The numerical solutions have also been tested for convergence for $\Delta x \to 0$ and $\Delta t \to 0$.

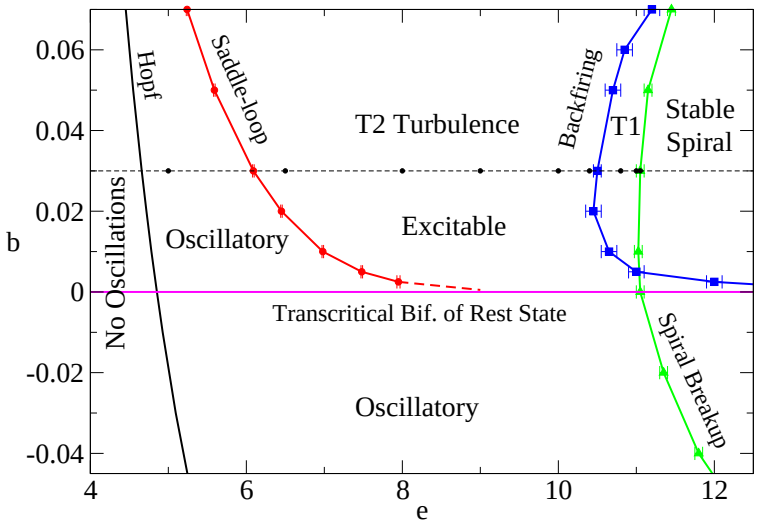

Figure 3.11: 2D bifurcation diagram of the modified Bär model for $D_v = D_u = 1$ and $a = 0.84$. The Hopf and transcritical bifurcation lines were computed analytically, the saddle-loop line was computed numerically whereas all the other lines have been estimated from simulations of 1D (backfiring) and 2D (spiral breakup) systems. The dashed line with dots highlights the main set of simulations discussed in this paper.

The phase diagram for the parameter regimes of interest is shown in Figure 3.11. Unlike the original Bär model, no meandering is observed before the onset of spiral breakup and, consequently, the region of spiral instability is greatly reduced (see Ref. [130] to compare the region of stability in the Bär model). The initial spiral instability is difficult to classify in the core/far-field dichotomy because, while the initial breakup occurs relatively close to the core and propagates outward, the core itself is stable up to and slightly after the onset of turbulence until it is perturbed by the encroaching turbulence. Nevertheless, since the instability of the emitted waves seems to be induced by their high curvature close to the core, we should clasify it as a core instability. The backfiring bifurcation occurs soon after

onset of spiral breakup in the excitable regime. There is nonetheless a narrow band, labeled T1 in accordance with the definition in Ref. [130], where spirals are unstable and traveling pulses are stable. At lower e value, a stable limit cycle is formed through a saddle-loop bifurcation which is then lost in a Hopf bifurcation. A change in the rest state stability turns the excitable dynamics into an oscillatory one for $b < 0$. The backfiring regime (T2), once excited, is functionally very similar to the oscillatory regime and can re-excite previously excited regions without re-entry. In the following, we chose to set $b = 0.03$ and vary e as our control parameter.

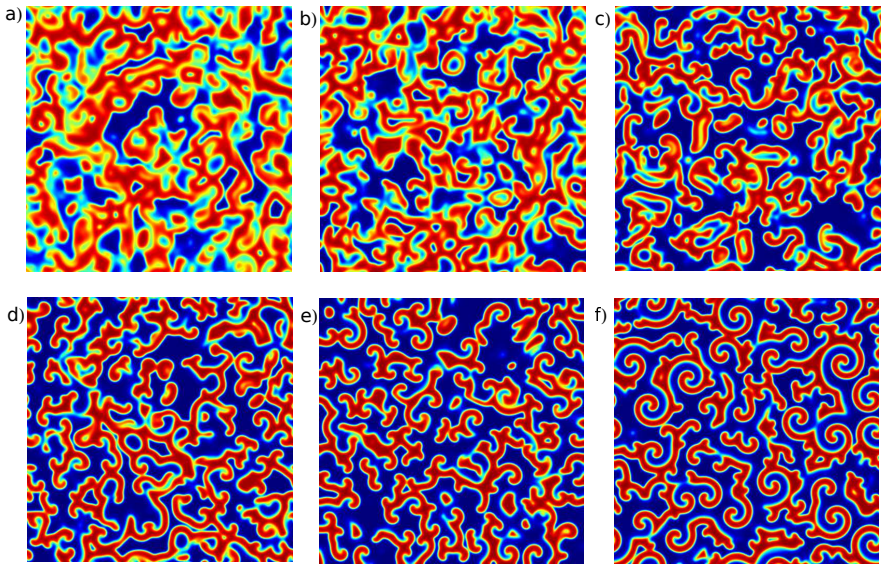

Figure 3.12: Snapshots of the turbulent pattern of the u-field in the modified Bär model. From a) to f): $e = 8.0$, $e = 9.0$, $e = 10.0$, $e = 10.4$, $e = 10.8$ and $e = 11.0$. While local structure are clearly present at $e = 11.0$, very little local organization remains past $e = 10.0$ and the pattern is reminiscent of the CGLE's in the AT regime (Figure 3.2). All frames correspond to a system size $L = 204.8$ with periodic boundary conditions and all snapshots were taken far into the steady turbulent regime.

Perhaps coincidentally, it is still possible to find a suitable regime where the stability of waves and spirals undergo a sequence similar to the one studied in Ref. [78] where a 2D spiral first becomes unstable followed by the backfiring instability of plane waves. We found that this sequence was best observed by setting $a = 0.84$, $b = 0.03$ and varying e. Coming from large values of e, we find that the stable spiral becomes unstable at $e_{\mathrm{bu}} = 11.05$ whereas the

backfiring of traveling pulses occurs at $e_{\mathrm{bf}} = 10.45$. Figure 3.12 shows a series of snapshots of the turbulent pattern along this trajectory in parameter space.

3.3.2 Defect statistics

Figure 3.13 shows defect-related averages and a synthesis of the statistical measures in the turbulent regimes as the control parameter e is varied. Phenomenologically, the same sequence of events as reported in Ref. [78] is observed. However, we notice that the ratio $\gamma_n = 2\sigma/\langle n \rangle$ starts to deviate on the left of the backfiring bifurcation, whereas it started to deviate on the right of that same bifurcation in the Bär model (as seen on Figure 3.15). This brings back into question the role of the backfiring bifurcation in the qualitative change of turbulence mechanism since we cannot seem to correlate the two precisely. Finally, we made direct observations of the creation and annihilation rates which indicate that, contrary to the previous deviations in the CGLE, the deviations of γ_n, which are smaller than unity, are caused, at least in part, by a self-inhibition process of the creation rate close to onset of the spiral instability i.e. the creation rate has a negative slope. This is consistent with the analogy of the vortex liquid state [78] where the local structures are very stable such that, once established, they effectively organize and stabilize the surrounding field. In accord with this interpretation, we also observe that the reduction of this self-inhibition and the eventual turbulence transition (tt line) corresponds with the local breakup of the pattern and progressive disappearance of local spirals in Figure 3.12.

3.3.3 Spacetime loop statistics

The n-span and t-span PDF of spacetime defect loops (Figure 3.14) also show some interesting characteristics. Like for the peroxidase model, the t-span of defect loops are all influenced by the periodicity of the pattern i.e. some short t-spans are relatively less likely than others in accordance with the excitation period. However, like in the previous cases, the long t-span loops appear to scale with a power law behavior with a critical exponent

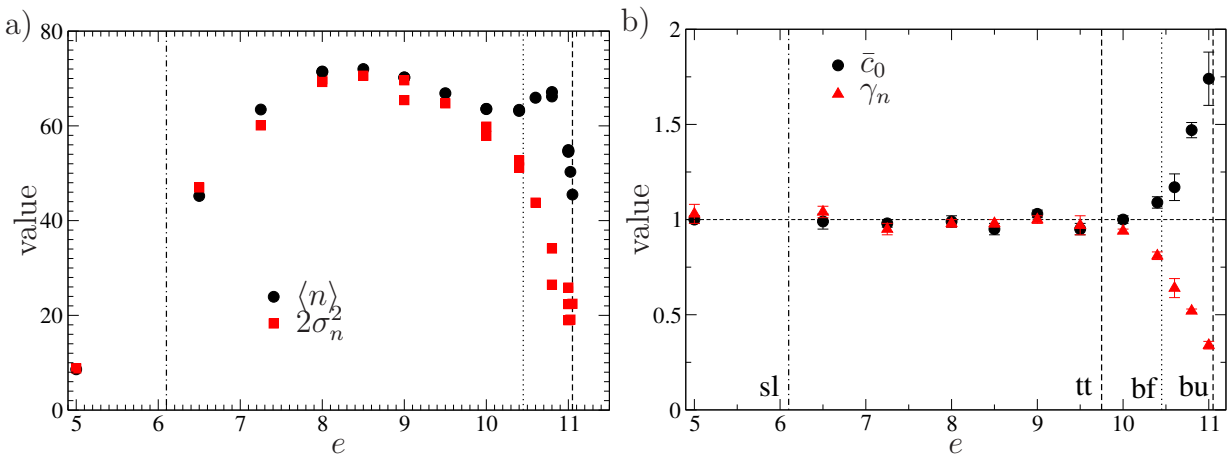

Figure 3.13: Averages and statistical measures in the defect turbulent regime of the modified Bär model. a) Average number of defects and variance (times 2) of the time series of defects in a system size with $L = 204.8$. The turbulent regime appears supercritically from the left near the Hopf bifurcation, but subcritically from the right — corresponding to the core instability of spiral waves. b) The behavior of the statistical measures appears to separate two regions of parameter space at the *tt* line.

around $\gamma + 1 = 3.0$, which is comparable to the values observed previously and in Ref. [45]. However, we can also notice that the t-spans for $e \geq 10.0$ started to have more frequent very long lived defect loops than the expected power law would otherwise suggest. This finite size effect is reinforced the closer one gets to the onset of spiral breakup and no obvious scaling appeared. For its part, the PDF of n-span appears again to be well approximated by a power law with critical exponent $\alpha + 1 = 2.6$ at every parameter regime where sufficient data had been accumulated for its estimation. Incidentally, this is the first observation of spacetime defect loop statistics in excitable media to our knowledge, and the fact that their scaling, at least in one regime, is in every respect comparable to oscillatory media shows the close connection between the phenomenon of DMT in these different media.

3.3.4 Discussion

The modified Bär model offers us a unique platform for the study of excitable wave turbulence phenomena. We have observed two qualitatively different states separated by a turbulence

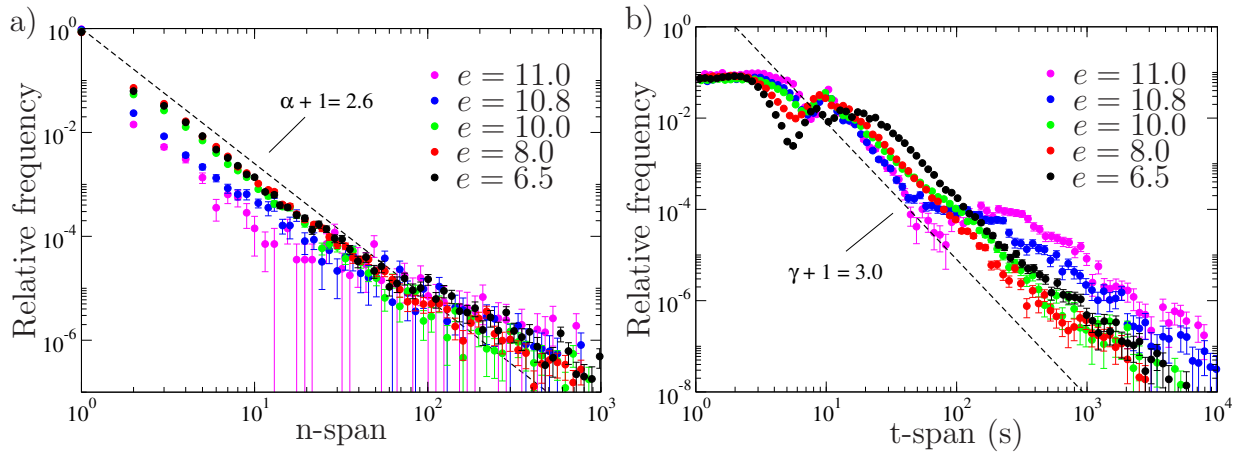

Figure 3.14: Spacetime defect loop statistics in the modified Bär model. The statistics close to onset of the spiral breakup for $e > 10.0$ do not appear to scale nicely like in the other regimes, forming a higher relative frequency of very long loops that "wrap" around the periodic system. This behavior is non-generic and falls under the category of finite-size effects. Surprisingly, even in the excitable regime closer to the Hopf bifurcation, the distributions scale in the same way as in the previous oscillatory media. The lifetime of defect loops also shows the oscillation in relative frequency for small loops observed in the PO model, which again produces troughs at multiples of the medium's dominant frequency. All dashed power laws serve to guide the eye in comparing with Figure 3.4.

transition. On one side of this transition, the defect rate statistics are well reproduced by null model of DMT with $\bar{c}_0 = 1.0$ and $\gamma_n = 1.0$. Of particular interest, we found that the scaling exponent of n-span in that regime was $\alpha + 1 = 2.6$, in agreement with all other regimes discussed so far in oscillatory media. On the other side of the transition, the defect creation rate gained a hitherto unique self-stabilizing form, resulting in a narrower distribution of defects, which was more and more important the closer one gets to the spiral instability. New simulations of the unmodified Bär model (Figure 3.15) and previous results [78] revealed two similar turbulent regimes. However, two important differences appeared. Firstly, no hysteresis was observed in the modified Bär model, whereas hysteresis can clearly be observed in the original Bär model. For instance, for $a = 0.84$ and $b = 0.07$ and varying e, both spiral and turbulent behavior are stable in the face of small fluctuations (say random noise of a certain magnitude) between $e_{\text{bu}} = 14.38$ and $e = 14.75$ with no-flux boundary conditions. Only turbulence exists for $e_{\text{bu}} < 14.38$ and a single spiral eventually

re-invades the medium for $e > 14.75$. This is shown in Figure 3.15, where the turbulence statistics can be measured on the right of the breakup (bu) line. Secondly, the original Bär model, with non-diffusive inhibitor species, appears to produce a more complicated behavior for the defect rates as e is varied. While there are again self-inhibitory defect correlations ($\bar{c}_0 > 1$) in the creation events close to the onset of spiral breakup, these correlations rapidly change to self-enhancing ($\bar{c}_0 < 1$) for $e < 13.5$. This tendency then gradually diminishes toward a state with $\bar{c}_0 \approx 1.0$ as the Hopf bifurcation is approached. On the other hand, the shape ratio of the distribution appears nearly constant at $\gamma_n \approx 0.90$ everywhere below $e = 11$ and appeared to characterize an even more stabilizing process ($\gamma_n < 0.90$) above that value. This emphasizes that the change in the defect event correlations, which determines whether the overall process is stabilizing or destabilizing, can often not be captured by the creation rate alone. In this case, both the creation and annihilation rates conspire to produce a smoothly varying distribution of defects.

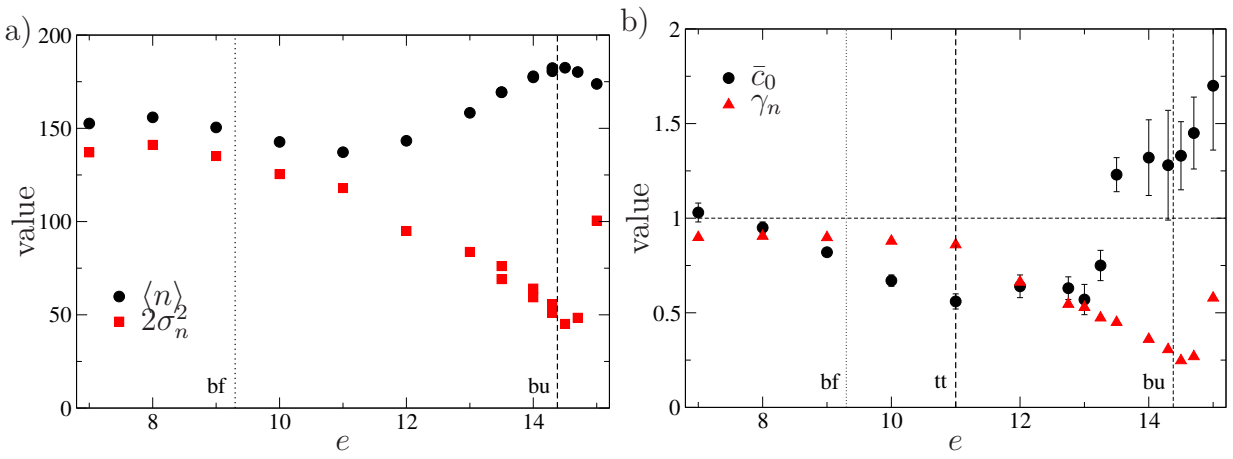

Figure 3.15: a) Averages and b) statistical measures in the defect turbulent regime of the Bär model in a system size $L = 204.8$ with periodic boundary conditions. The *tt* line marks the separation of two turbulent regimes according to the qualitative behavior of γ_n.

If we compare these two latter cases of core instability with the previous cases of far-field instability in the CGLE, there appear two main differences. First is the destabilizing effect of the defects for the far-field instability *vs.* their stabilizing effect in the case of the

core instability. Second is the apparent correspondence of these effects with the presence or absence of local spiral patterns. The stabilizing (destabilizing) processes sometimes take effect through a self-inhibiting (self-enhancing) creation rate and sometimes through a different than quadratic annihilation rate, but always resulting in a narrowing (widening) of the defect distributions[11]. It is still unclear how general these observations are. However, we conjecture that the absence of local spiral pattern is not essential for the destabilizing effect. In particular, section 4.3.3 will provide an example of an excitable medium with a far-field instability where local spiral patterns are still observed in the turbulent regime. Yet, this regime shows a slight self-enhancing creation rate with $\bar{c}_0 = 0.84 \pm 0.08$ but a near squared poissonian distribution with $\gamma_n = 1.02 \pm 0.12$. However, all other systems and regimes investigated in section 4.3 support the first observation. While this argues in favor for a weak version of IDDMT, i.e. a division along the line of core and far-field instability driven turbulence, the next chapter will show that this apparent division gets a lot more blurry in three dimensions.

Finally, it also appears that the nature of the instability ceases to play an important role when the breakdown of local order is complete, as observed in the case of AT in the CGLE far from onset of spiral breakup, in the peroxidase model, and after the backfiring instability in the modified Bär model. The complete breakdown of order thereby appears to be characterized by the observation of the simple null model rates ($\bar{c}_0 = 1$, $\gamma_n = 1.0$) which correspond to completely passive and uncorrelated defects, and in this sense, to fully developed defect turbulence. This does not mean that all regimes far from onset of a spiral breakup must necessarily correspond to fully developed turbulence: "Far from onset" is a qualitative and arbitrary way to characterize the distance from a certain instability line, but the fully developed turbulent regime is a region of phase space which must depend on the whole phase space and all other instabilities present. The regime of the Bär model after the

[11]Narrowing (widening) is relative to what would be expected from a random process as described by the null model.

turbulence transition in Figure 3.15 illustrates this: even though the statistics deviate from that of the null model, the pattern appears random and without local spiral structures.

3.4 Chapter summary

We explored many characteristic features of 2-dimensional DMT in various models. We observed that many of the statistical measures seemed to vary smoothly across the bifurcation and instability of simple structures (like the Eckhaus instability of wavetrains at the wavelength emitted by the spiral in the CGLE, or the backfiring instability of pulses in the Bär model). There appears nonetheless qualitatively distinguishable regimes of DMT in some cases. We showed one example where the defects appear to have a destabilizing effect close to onset, enhancing the creation of more defects, and one where they appear to have the exact opposite effect, inhibiting the creation of new defects. In both cases, this only occurred close to onset of the spiral instability, which were of the far-field and core breakup type respectivelly, and disappeared far from onset. Likewise, the loss of these correlations seemed to coincide with the breakdown of local order in the field, although it is very hard to quantify in the case of the CGLE, where the pattern already appeared random (AT). All results presented in this chapter are based on new simulations of the respective systems and go beyond the precision at which these values had been evaluated (if at all) before.

Chapter 4

3-dimensional media

In 3-dimensional media, entirely new and unique instabilities appear and thus new mechanisms of DMT become available as well. For example, the negative line tension (NLT) instability of scroll waves is a purely 3D effect [73] associated with the onset of Winfree turbulence (WT), a special case of autowave turbulence or DMT [51, 75, 132, 133]. The NLT instability has received considerable attention as a possible candidate for inducing ventricular fibrillation (VF), which leads to sudden cardiac death — the leading cause of death in the industrialized world [47]. Yet, the question of the underlying cause or, more likely, causes of VF remains open. This is, in part, due to the experimental difficulties in obtaining clean and complete 3D data in realistic conditions [134], which could distinguish between NLT and other instabilities (2D and 3D), or other mechanisms entirely [103, 20], that could reasonably trigger the onset of VF.

One additional difficulty in the case of the heart is that experimental observations of the specific dynamics are constrained to the surface [134, 21, 55]. Technical difficulties aside, many physical systems including the heart's ventricles have a geometry such that their dynamics can neither be captured by a purely 2D medium or a fully 3D medium (in the infinite size limit) but they lie at the boundary between 2D and 3D. Phenomenological comparison of DMT in these situations requires a common observable. This leads to the general challenge to determine whether the surface dynamics of a given system allows one to distinguish between different types of DMT and their generating mechanisms.

As a first step to tackle this challenge, Davidsen *et al.* [43] derived a statistical model from numerical observations of WT and showed that the creation rate of surface defects as a function of the number of surface defects yielded a hitherto unique form. The specific

functional form, it was argued, was necessarily different from those generated by known 2D mechanisms due to the fundamentally different process of filament breakup in the turbulent state mainly involving the collision of filaments with the surface. This was further substantiated by studies of oscillatory media close to the Hopf bifurcation, which are described by the complex Ginzburg-Landau equation (CGLE) [82]. In the latter study, it was also found, for at least one specific regime of DMT, that there were no qualitative differences in the statistical properties of surface defects of a 3D medium compared to the defects of a true 2D medium.

In this central chapter, we will focus on the phenomenon of defect turbulence in 3-dimensional media. In particular, we will again take an empirical approach to show how the dimensionality affects the observables of DMT on the surface with new instabilities (of filaments) and with instabilities that already exist in two or lower dimensions. For a paradigmatic model of excitable media yielding extensive DMT, we provide convincing evidence that depending on the specific parameter regime the dimensionality of the medium by itself can have a profound influence on the statistical properties of DMT. Comparison with other models indicates that this behavior is not model specific. In addition, we show that the total creation rate of surface defects as a function of the number of defects is insufficient to fully determine the underlying mechanism for DMT, since the surface statistics generated by the mechanism in one regime are virtually indistinguishable from those generated close to onset of a NLT-like instability. This is despite the fact that the mechanisms are demonstrably different as we show by a decomposition of the creation rates into different contributions and with direct measurement of filament growth rates.

The chapter is divided into three sections. First, we shall review and describe more thoroughly the statistical features of WT in the Barkley model and filament turbulence in the CGLE under the lens of the methods developed in Chapter 2. Then we shall consider the modified Bär model to show a new surprising effect at the onset of spiral breakup in an

excitable regime. This effect, which we call dimension dependent defect turbulence (DDDT), does not appear to exist close to a Hopf bifurcation. In the third section, we will provide further evidence that DDDT is ubiquitous and present in oscillatory, excitable and bistable media.

4.1 Unique 3D defect turbulence mechanisms

There are only a few known genuinely 3-dimensional instabilities of scroll waves but they have received increased attention since it has been suggested that the instability involved in the degeneration of benign tachycardia to deadly VF may involve a 3D mechanism [51]. Of particular interest is the NLT of scroll waves which has been described formally in a simplified context [73, 74] and found to be present in regimes of low [135] and high [136] excitability in a realistic model of cardiac action potential [53]. In effect, this instability implies that any perturbed straight or curved filament will grow (and often wrinkle) and, assuming no other factor balance the growth, lead to WT, where endless growth is only eventually balanced by the interaction between filaments and the boundary of the medium.

4.1.1 Negative line tension instability in the Barkley Model

We introduce the Barkley model [137] here because it is one of the simplest models to show the NLT instability of scroll waves and we used this model to test our method and expand published results. This model is a precursor of the Bär model and it is described by the same system of equations as Eq. 3.5 with $f(u) = u$. The diffusion constants $D_u = 1$ and $D_v = 0$ induce meandering in the spiral tip trajectory which depends on the system's parameters. However, spirals do not break up in two dimensions and DMT exists only in 3D as a result of the growth of filaments after the onset of the NLT instability. Incidentally, spiral meandering in 2D has been linked to NLT in 3D [55, p. 9] and the Barkley model offers a case in point. In the following, the parameter values were set to $a = 1.1$, $b = 0.19$ and $e = 0.02$ corresponding

to the regime of NLT close to onset. A phase diagram of the Barkley model can be found in Ref. [138] and a further closeup of the region of interest can be found in Ref. [83]. The onset of NLT occurs around $b = 0.175$ and lower values show a regime of weak positive line tension (PLT) and hence, filament loops collapse and straight filaments are stable. The numerical integrations have been performed using a simple mid-point explicit method with a 7-point Laplacian on a cubic lattice with $N = 250$, $L = 100$ and $\Delta t = 0.005$. Owing to the relatively slow spiral dynamics, we used a sampling interval of $\Delta s = 0.1$ which means that only one frame every twenty was analysed for the purpose of tracking filaments.

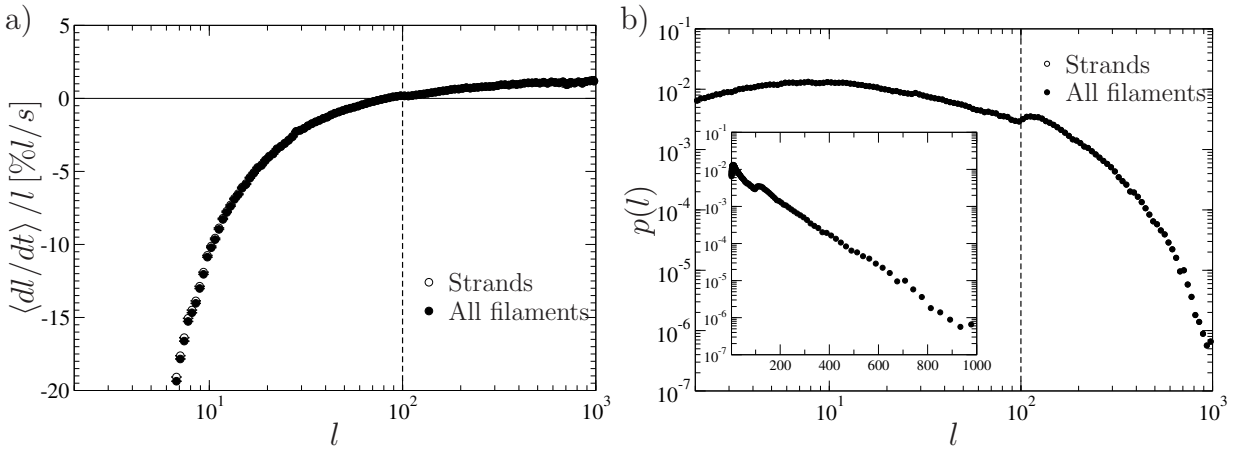

Figure 4.1: a) Average growth rate of filaments in the NLT regime of the Barkley model. Small filaments typically shrink as they are "pushed" out of the system and long filaments typically grow. b) The filament length distribution appears to decay exponentially with a peak at around the linear size of the system, indicating a slight tendency of straight filaments to span the system. The vertical dashed line indicates the linear size of the system in both graphs. Note that this graph only presents the average growth rate and that the standard deviation of the growth rate is also liable to be dependent on the length of the filament and on the specifics of the regime. However, the latter proved too cumbersome to present here.

The constant filament growth induced by NLT can be directly observed as a statistical average in Figure 4.1a, which shows a graph of the average percentage rate of growth of the filaments as a function of their length. In spite of the NLT, the measured rate of growth doesn't show that all filaments grow on average — which is expected because the average growth must necessarily be zero for a stationary distribution of filaments. Therefore, the

important feature of the average growth is *which* filaments grow on average. In this case, the long filaments have an average rate of growth proportional to their length, at around 1.25 percent of their length per second of simulation. To satisfy the constant average length of filaments, certain filaments have to shrink. The only option is for filaments to break[1] as they collide with the boundary and leave the medium as they are pushed away due to the apparent low compressibility of the filaments. In this process, small broken filaments effectively become smaller and smaller, which accounts for the shrinking of small filaments. Another possibility would be the self collision of filaments forming loops that eventually collapse due to high curvature. However, the relative absence of loops suggests that this is not an important mechanism here. The overall average growth rate appears well approximated by $\langle dl/dt \rangle (l) \approx -g_0 + g_1 l$ with $g_0 \approx 108$ and $g_1 \approx 1.25$ for all filaments with $l > 10$. Finally, the distribution of filament length appears to be decaying exponentially with an average length of filament at around $\langle l \rangle \approx 95$.[2] A small peak in the length distribution also occurs near the system size indicating that the system may still be relatively small compared to the dynamical scale provided by the filaments such that the filaments tend to orient slightly to span the system i.e. that the system is effectivelly slightly anisotropic.

Figure 4.2 shows our surface rate decompositions developed in Section 2.3.3 which supports the previous analysis. Unlike many other cases, it is observed that only one mode of creation (splitting) dominates the entire creation of new surface defect pairs. We measured the overall creation rate at $\bar{c}_0 = -0.11 \pm 0.08$, which is very close to a purely linear form ($\bar{c}_0 = 0$), and a extremely wide distribution of defects with $\gamma_n = 4.6 \pm 1.3$, much wider than anything we have observed so far for mechanisms in 2D media. These statistical averages and the direct observation of the creation modes confirm the observations of Davidsen *et al.* [43] as well as the applicability of their model of statistically independent filaments in the

[1]Note that the filament growth rate is only evaluated on filaments that are detected as pure continuation from one frame to the next.

[2]If the previous description of growth rates applied exactly, we would expect $\langle l \rangle = g_0/g_1 \approx 86$, which is about 10% smaller than the actual value.

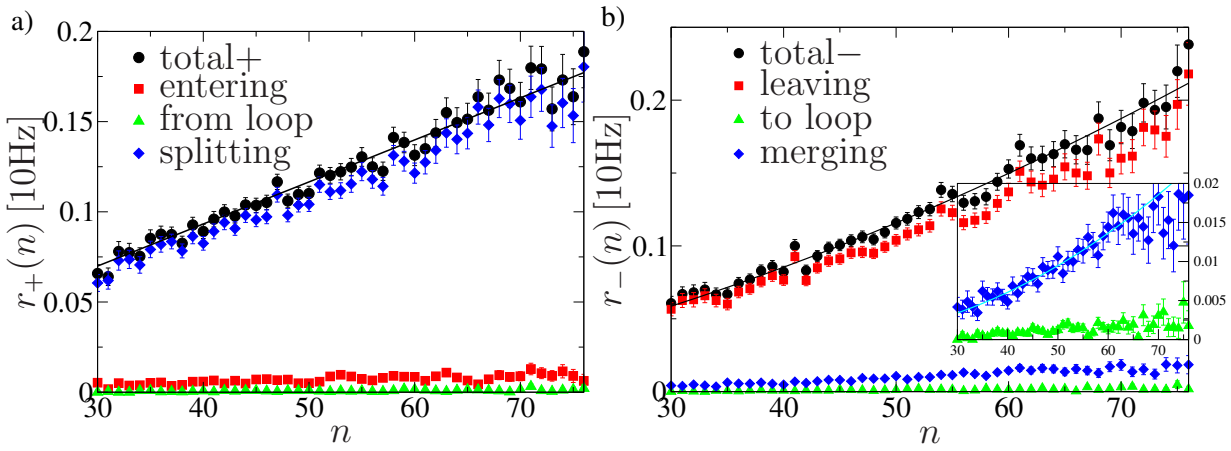

Figure 4.2: Rate estimates for the Barkley model in the NLT-induced WT regime. a) Rate of events that contribute to the surface creation rate and b) to the surface annihilation rate. The fit of the creation rate yields $r_+(n) = (243 \pm 7) \times 10^{-5} n - (5 \pm 4) \times 10^{-3}$ i.e. a purely linear relation. Notice in the inset that, though relatively small, the rate of merging of filaments follows an n^2 law very accurately. This allows us to specify a linear plus quadratic dependency for the total annihilation rate based on the two dominant processes that contribute to it. Also, it may be important to notice that albeit low, the entering rates (creation of surface defects far from existing filaments) are only expected to be vanishingly small close to onset.

limiting case close to onset.

This case also seems to support the hypothesis of IDDMT in the sense that, even though WT is a saturated pattern far from the state where the linear instability of scroll waves is mathematically defined, the linear instability still plays a significant role in the mechanism of turbulence because there are still local, weakly interacting, scroll wave structures for which the instability applies. In the present case, the NLT of the filament causes it to extend without bound, leading to collisions with itself, other filaments or the boundary. This is purely a consequence of the local behavior determined at onset. Indeed, we find that close to onset, virtually all filaments are created through this process, as opposed to turbulence generated by a different mechanism which would show in the other modes of the decomposition of rates and in the statistics of filament loops (e.g. as found in section 4.2.3). This instability likely becomes less dominant once the local spiral structures for which it applies are destroyed either from nonlinear behavior (which are not present close to onset)

or from the onset of other instabilities.

4.1.2 Finite wavelength instability in the CGLE and beyond

Purely 3-dimensional instabilities are not only found in excitable media. A large region of parameter space of the CGLE presented in Figure 3.1 corresponds to unstable filaments but strictly stable spirals in 2D. The following numerical integrations of Eq. 3.1 were performed using a mid-point explicit method with a 7-point Laplacian on a cubic lattice with $N = 250$ and $L = 250$ with $\Delta t = 0.005$ and sampling interval between $\Delta s = 0.005$ and $\Delta s = 0.05$ depending on the case.

Scroll waves in the CGLE can destabilize and yield a regime reminiscent of NLT-induced

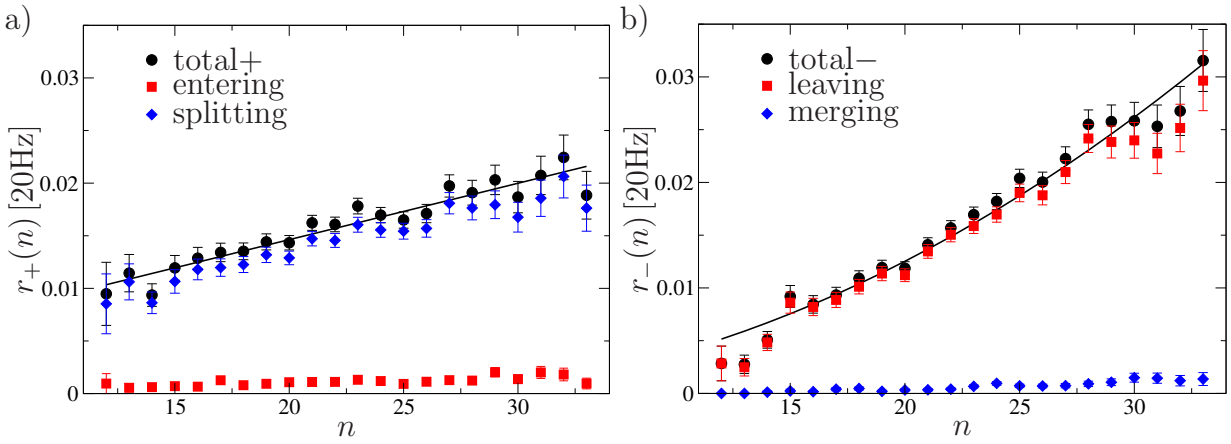

Figure 4.3: CGLE in a regime of NLT-like turbulence at $(b, c) = (4.0, 0.1)$. Like in the case of the NLT in the Barkley model, almost all new filaments are created through collision with the boundary and annihilated by leaving the medium through the boundary. $\bar{c}_0$ is estimated at 0.15 ± 0.08 which is again very close to purely linear. However, the distribution of defects is much narrower than for the case of the Barkley model with $\gamma_n = 1.54 \pm 0.26$, mainly due to the different annihilation rates. Again, the annihilation rate seems best approximated by a linear plus quadratic function.

WT [82] through a finite-wavelength instability [139, p. 11][3]. The parameter regime corresponding to this purely 3D turbulence and coarse instability lines are shown in Figure 3.1. Note that the onset of turbulence does not coincide with the onset of the scroll wave instabil-

[3]We are also told, on p. 11 in the same paper, that filament tension in the CGLE is in fact always positive.

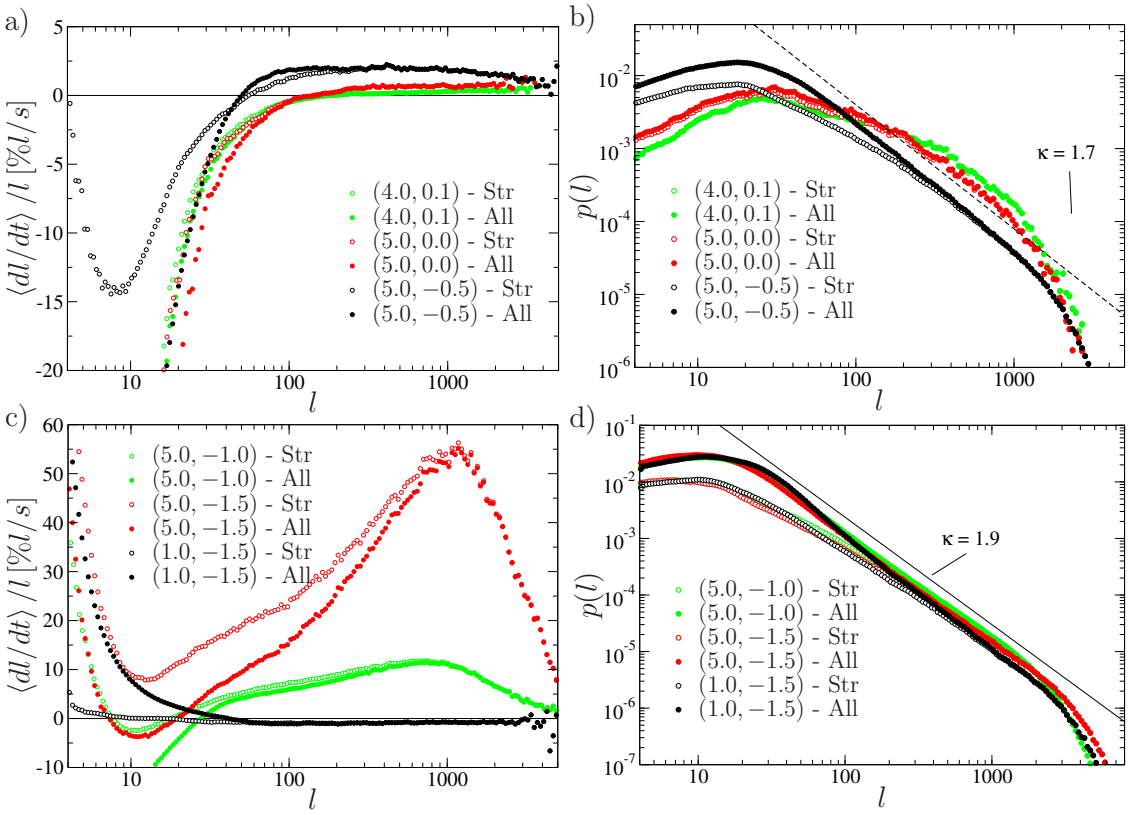

Figure 4.4: Average filament growth rates and filament length distribution in the CGLE. a-b) In the filament turbulence regime where 2D spirals are stable. c-d) In the AT regime of concurrent 2D and 3D DMT. "Str" stands for the filament strands i.e. filaments that intersect the surface of the medium. There is a transition in behavior between growing and shrinking long filaments somewhere in the AT regime, though the precise value of the transition is yet unresolved. It is highly dubious that the growth rates at $(b, c) = (5.0, -1.5)$ are quantitatively reliable due to the extreme overall rate of events which considerably affects our ability to evaluate the growth rate. However, other measures are unaffected. In the filament length distributions, the relative frequencies of filaments are scaled by the relative fraction of that filament type over all filaments i.e. $\int_0^\infty p_x(l)dl = \frac{\langle n_x \rangle}{\langle n_{\text{all}} \rangle}$ where x stands for loops, strands, or all filaments.

ity [106]. Here, scroll waves lose stability subcritically to a stable helical solution [140, 108] which, in turn, loses stability to a superhelix and eventually to sustained 3D DMT. Here again, near the onset of 3D DMT at $(b, c) = (4.0, 0.1)$, the overall creation rate can be almost entirely accounted for by the perpetual elongation and collision of existing filaments (Figure 4.3). Figure 4.4a observationally confirms that the average growth rate of filaments is dominated by the growth of long filaments and the relative absence of filament loops. This draws the parallel with the NLT instability in excitable media, as the same turbulence mechanism seems to apply in every respect. However, while remaining in the purely 3D turbulence regime, this picture of "pure" filament-elongation-driven turbulence starts to deviate significantly farther from onset. At $(b, c) = (5.0, 0.0)$, which is the NLT-like regime studied in Ref. [82], the average growth rate indicates that the filaments are more active and this correspond to the appearance of a significant number of pure creation events as well as a small fraction of filament loops. Furthermore, about one third of these loops are created far from any other filaments whereas loops could only be created from the self-collision of filaments before (the remaining two thirds). This trend continues to $(b, c) = (5.0, -0.5)$ and beyond in the amplitude turbulence (AT) regime at $(5.0, -1.0)$ and $(5.0, -1.5)$ where the filament growth distribution now appears to be very complex (it is likely that the growth rate of large filaments is quantitatively spurious due to the higher rate of events), but still surprisingly characterized by growing long filaments (Figure 4.4b). However, note that this behavior is completely different from what would be observed in the AT regime at $(b, c) = (1.0, -1.5)$ studied in Ref. [82] and whose long filaments now shrink and small filaments grow. Therefore, there must be a new type of transition where the reversal of the growth rate between short and long filaments occurs in the range $1.0 < b < 5.0$. However, we have not resolved this transition and it is the subject of conjecture whether this change corresponds to the instability of scroll waves inside this AT regime which, incidentally, occurs in the same region.

Apart from the regime very close to onset of the filament instability, where the length distribution of filaments is close to exponential, the length distributions in the CGLE (Figure 4.4b and d) appear to follow a power law behavior with an exponential cutoff after the initial peak at short length. The power law regime of the overall distributions is divided into short filaments dominated by the loop scaling and long filaments dominated by the strand scaling. The long strands scaled roughly between $l^{-1.7}$ and $l^{-1.9}$ depending on the regime whereas the loops scaled at around $l^{-2.8}$ (not shown). The loops always scaled with a greater negative exponent, which accounts for the "kinked" scaling of the overall distributions. Systems of different sizes have been tested and shown to extend (or reduce) the location of the cutoff, but not the scaling. Again, the apparent scaling is not a proof of power laws, but warrants further study.

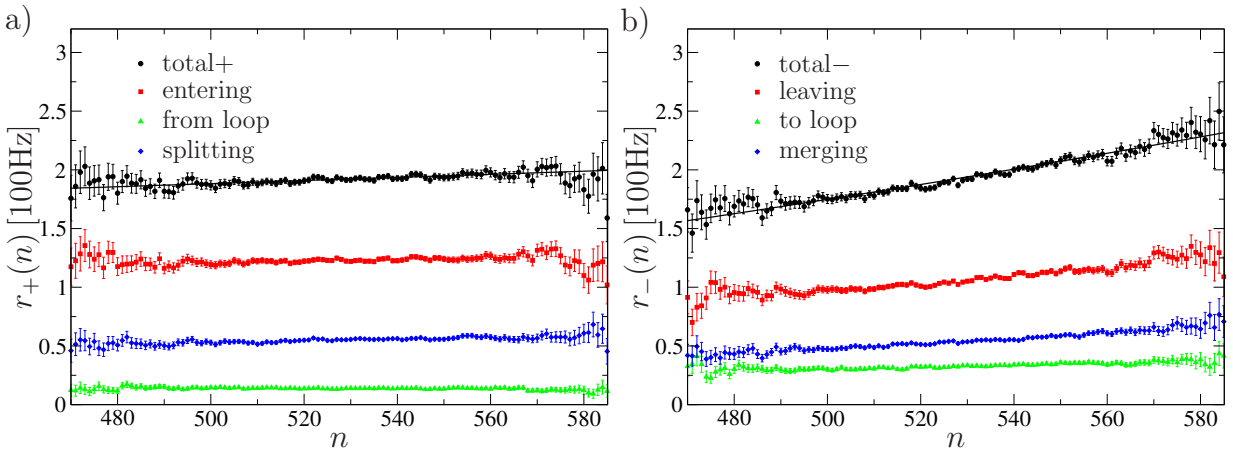

Figure 4.5: Typical decomposition of surface rates based on the filament detection method in the CGLE at $(b, c) = (5.0, -1.0)$. All regimes of concurrent 2D and 3D DMT had the same overall decomposition, though not necessarily the same dependency for each component on the total number of surface defects. In this case, the creation rate best fit yields $\bar{c}_0^{3D} = 0.59 \pm 0.03$ with $\gamma_n^{3D} = 1.42 \pm 0.08$. The overall annihilation rate seemed to follow a linear plus quadratic dependence on the number of defects.

Now returning to rate decompositions, we mentioned the gradual increase in the contribution from the pure creation component of both loop and strands, i.e. that filaments are now created far from existing filaments, as we move along the same path from NLT-like at

$(b, c) = (4.0, 0.1)$ to AT at $(b, c) = (5.0, -1.5)$. Figure 4.5 shows the creation and annihilation rate decompositions at $(b, c) = (5.0, -1.0)$ after the onset of the AT regime. The entering mode is dominant but collision of filaments also accounts for an important fraction of surface events. The best fit of the overall creation rates was evaluated at $\bar{c}_0^{3D} = 0.59 \pm 0.03$ with an overall distribution of surface defects with $\gamma_n^{3D} = 1.42 \pm 0.08$. Apart from the different functional form of the rates, this is essentially the same decomposition that would be observed in any other AT regime.

4.1.3 Discussion

At first sight, the behavior close to onset of DMT in 2D appears strangely similar to the surface behavior in 3D. A comparison of the 2D and 3D surface creation and annihilation rates at $b = 5.0$ with varying c is shown in Figure 4.6. The appearance of the destabilizing rate correlations in 2D close to $c_{\text{onset}} = -0.69$ appeared to be mirrored by a similar process for the 3D surface rates. However, the 3D data is still extremely scarce and the latest 3D simulations very close to the onset of 2D DMT seem to yield a significant discrepancy between 2D and 3D surface statistics, which would warrant further investigation[4].

Below c_{onset} in the AT regime, it appears as though filaments, being advected[5] from the fluctuation of the field like the defects in 2D, also only play a passive role i.e. they do not organize the medium. For instance, at $(b, c) = (5.0, -1.0)$ which we investigated in greater detail, the shape factors of the corresponding distributions were estimated to be

[4]The biggest difficulty with this kind of empirical study is that, the closer you look at the phenomenon, the more differences appear. At first, AT in the CGLE was assumed to be completely characterized by the null model as confirmed by the coarsest measurements. Now, the presence of event correlations, as described in Chapter 3, is unmistakable but we cannot yet distinguish between 2D and 3D surface measurements in many cases in the AT regime. It is not hard to imagine that this apparent indistinguishability is only due to the coarseness of our results (even if they are the most accurate observations to date) yet again. Therefore, we consider these negative results (indistinguishability) necessarily weaker than the positive distinguishability of regimes that will follow in Section 4.2.2.

[5]Advected, in this context, refers to the creation of defect pairs from the random fluctuations of the field as opposed to wavebreak.

$\gamma_n^{2D} = 1.31 \pm 0.05$ and $\gamma_n^{3D} = 1.42 \pm 0.08$ which is a discrepancy within error[6] and it is impossible to tell from surface measurements whether the system under study was really 2D or 3D. Likewise, in Ref. [82], it was surmised that there were no essential difference between the 3D surface rates and 2D rates in a AT regime at $(b, c) = (1.0, -1.5)$ where the rates tend toward $\bar{c}_0 = 1.0$ and $\gamma_n = 1.0$. Our results suggest that this continues to apply even when the rates do not follow the null model's and it can be conjectured that this remains valid in all regimes of the CGLE.

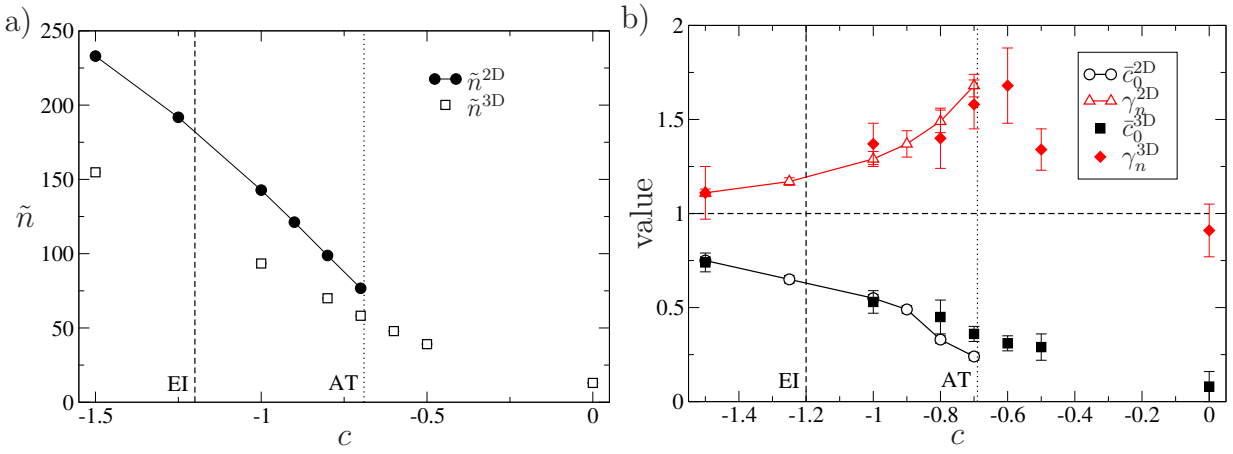

Figure 4.6: a) Comparison of the normalized average densities of surface defects $\tilde{n} = \langle n \rangle \times 256^2/A$, where A is the total surface area of the medium where the defects are counted, between 2D and 3D systems at $b = 5.0$. Note that, in the regime where it can be compared, the 3D densities are lower by a constant factor of 0.66 ± 0.02. b) Shape factor γ_n of the distribution of defects and normalized constant creation rate component $\bar{c}_0$ over the same parameter regime. The horizontal dashed line indicates the expectation from the null model.

While the distributions of defects and rates appear indistinguishable from their 2D counterparts, the average density of defects between 2D and 3D simulations varies dramatically. Figure 4.6a shows a comparison of the normalized average densities of defects which can be interpreted as the number of defects in a system of size $L = 256$. We find that, in the regimes where we could compare the 2D and 3D densities, the ratio of densities was always

[6]One must also consider the systematic error due to the boundary condition. We have found that, in general, the distribution ratio tend to be systematically overestimated for smaller system sizes with no-flux BCs and converge when $L \to \infty$. The periodic BCs that were used for 2D simulations converge much faster to the asymptotic value.

nearly constant at $\tilde{n}^{3D}/\tilde{n}^{2D} = 0.66 \pm 0.02$. We will consider an explanation of this behavior based on the random nature of the filaments in next section.

Finally, our detailed statistical analysis of the NLT regime in the Barkley model and the finite wavelength instability at onset of filament turbulence in the CGLE confirms that both turbulent regimes are maintained by the same mechanism as characterized by the rates $\bar{c}_0 \approx 0$, distribution of defects $\gamma_n > 1.0$ and growth rates of long filaments $\langle dl/dt \rangle \propto l$. Although this may have appeared obvious at first, it became less obvious with time as we realized that there were alternative mechanisms that would produce the same surface measurements. Let us turn to a model that presents such an alternative.

4.2 Turbulence transition in the modified Bär model of excitable media

4.2.1 Model and simulations

Here, we use again the modified Bär model introduced in Section 3.3.1. All numerical integrations have been performed on an $N \times N \times N_z$ lattice corresponding to an $L \times L \times L_z$ box with our usual simple mid-point explicit method with a maximum Δx and Δt of 0.4 and 0.01 respectively. The numerical results have also been tested for convergence for $\Delta x = 0.2$ and $\Delta t = 0.005$ whenever possible.

4.2.2 Results

We characterized the average number density of vortices and surface defects as a function of the system size, thickness and control parameter as shown in Figure 4.7. The density of vortices is very close to the apparent asymptotic limit for system sizes with $L > 200$ for no-flux boundary conditions (periodic boundary condition averages converged to the same value). In 3D, it appears that the average number of surface defects saturates for systems as small as $L \approx 80$. Yet, as Figure 4.7b shows, the average rate is still increasing slowly even up to the maximum system size we were able to study. Nonetheless, the approaching

saturation of the densities indicates that the surface turbulence appears to be extensive in both 2D and 3D.

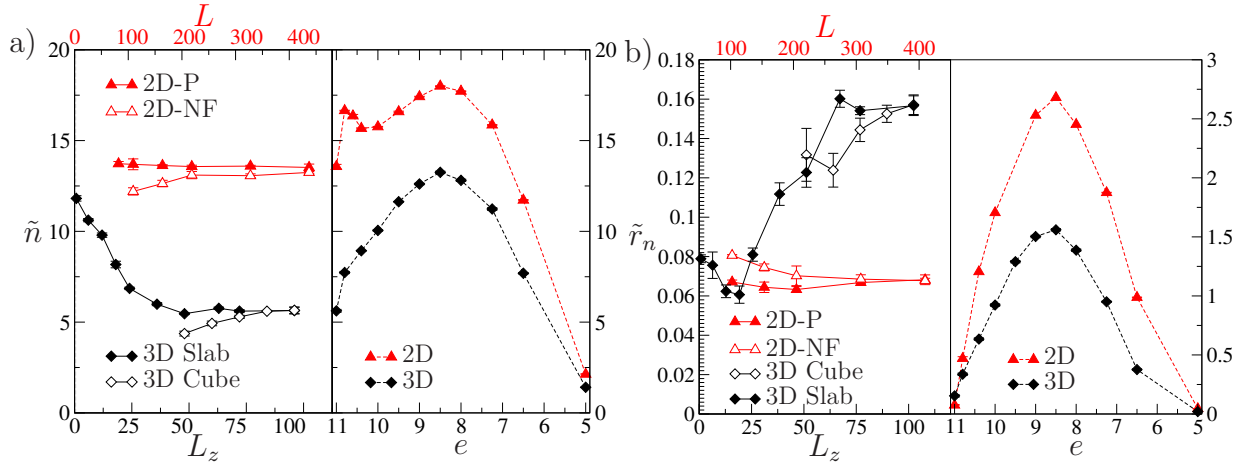

Figure 4.7: a) Scaled average vortex and surface defect densities $\tilde{n} = \langle n \rangle \times A_\perp / A$ with $A_\perp = 102^2$ as a function of the system's size at $e = 11.0$ (left panel) and as a function of the control parameter e for $L = 204$ in 2D and $L_z = 76.4$ in 3D (right panel). 2D (3D) systems size are characterized by L (L_z). In all cases, A is the total surface of the medium $A = 2L^2 + 4LL_z$ where $L_z = L$ for the 3D-cube cases and $L_z = 0$ for the 2D cases. 2D systems are all L-squares with periodic (P) or no-flux (NF) boundary conditions whereas there are two sets of 3D systems: L-cubes, and slabs of fixed cross section $A_\perp$ and varying thickness L_z. Note that the slabs interpolate between the 2D system with no-flux boundary conditions and the 3D cube. b) Scaled average defect rate density $\tilde{r}_n = \langle r \rangle_n \times A_\perp / A$ for the same systems as in a).

It is not so surprising that the number and rates densities vary wildly between different parameter regimes, as shown on the secondary axis of Figure 4.7. However, the same plots also show that the saturated surface densities vary between 2D and 3D simulations and it appears that all 3D regimes surface defect densities are lower than their 2D counterpart. Specifically, the ratio of densities between 2D and 3D surface defects appears to be nearly constant at $\tilde{n}^{3D}/\tilde{n}^{2D} \approx 0.69 \pm 0.03$ over most of the T2 regime ($e < 9.0$). Roughly the same ratio was observed to hold in an amplitude turbulence regime of the CGLE in section 4.1.3 ($\approx 0.66 \pm 0.02$) and in the T2 regime of un-modified Bär model ($\approx 0.71 \pm 0.03$). These observations can likely be accounted for by the volume occupied by filaments inside the medium occluding the surface of the medium. Assuming a rigid cross section around each

defect, a tilt of a filament "cylinder" should stretch the surface defect cross section by a factor $1/\cos\theta$ where θ is the angle between the tangent of the filament and the normal of the surface such that the number density contributed by such a filament becomes $\tilde{n}(\theta) = \tilde{n}^{2D}\cos(\theta)$. Therefore, for a uniform distribution of filament directions, one has $\tilde{n}^{3D} \equiv \langle \tilde{n}(\theta) \rangle_\theta \approx 0.64\tilde{n}^{2D}$, which would explain the change in surface density by a purely geometrical argument.

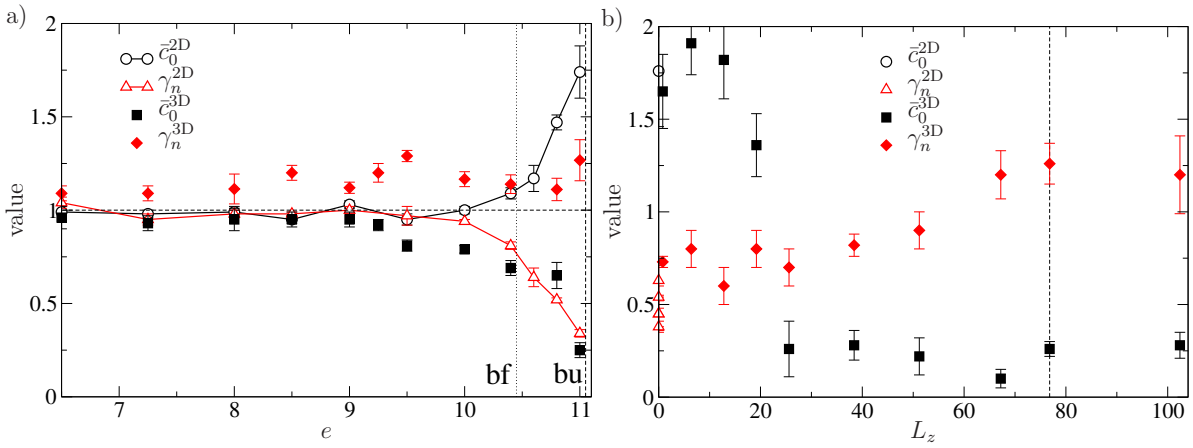

Figure 4.8: Turbulence statistics with a) varying control parameter e for a set of 2D systems ($L = 204.6$ with periodic BCs) and thick 3D slabs (cross section $A_\perp = 102^2$ and thickness $L_z = 76.4$, corresponding to the dashed line in b)), and b) varying thickness L_z of the medium at $e = 11.0$. The rightmost dashed line in a) indicates the spiral breakup (bu). Notice how the ratio and constant component seem to collapse on the left side of the backfiring instability (bf) for $e < 9.0$. The observed deviations from $\gamma_n^{3D} = 1$ are likely accounted by the finite size effect in the 3D simulation since 2D systems with the same cross section surface showed qualitatively the same deviations. Consequently, the no-flux boundary conditions have a considerable influence on γ_n for the thin, and relatively small, 3D systems. The sequence of 2D systems (down triangles), which corresponds to system size $L = 102$, 153.2, 204.4, 306.8 and 409.2, respectively, from top to bottom in b), reconciles the value observed at $e = 11.0$ in a).

In spite of the large variation in number and rate densities with e, the creation and annihilation rates of defects and surface defects sometimes take on specific functional forms within certain regimes. We characterized the creation rate and shape factor of the distribution of surface defects in Figure 4.8. Close to the onset of spiral breakup, the 2D creation rates show a self-inhibition trend i.e. the slope of the creation rate is negative corresponding to $\bar{c}_0 > 1$. On the other hand, the 3D surface rates show a self-creation tendency with a positive slope,

i.e., $\bar{c}_0 < 1$. Similarly, γ_n changes its behavior in direct relation. Both observations indicate a transition in the behavior between 2D and 3D surface defect turbulence and we chose to refer to regimes showing this transition as dimension-dependent defect turbulence (DDDT). One would think that the 3D behavior is easily explained by the fact that filaments now extend, bend and collide with the surface generating an additional contribution to the total creation rate with a linear dependency on the number of existing strands, or through the collision of loops with the surface. However, a closer analysis of the rate contributions from different types of events using the classification discussed in section 2.3 reveals that the self-creation doesn't emerge from such a single new "type" of event. Instead, we observe a complete reorganization of the turbulent state such that even the pure creation far from existing filaments (entering) component, as shown on Fig 4.10b, has a positive linear contribution that didn't exist in 2D. This demonstrates that, even with the same primary instability (due to the special nature of the system chosen), the phenomena of spatiotemporal turbulence in 2D and 3D can be very different – different time (rates) and spatial (density) scales and different mechanisms with presumably different dynamical complexity.

However, we also observe that this is not necessarily the case since, as we move away from the initial spiral instability (and, incidentally, get closer to the Hopf bifurcation), the 2D and 3D surface rates essentially collapse onto one another in Figure 4.8 for $e < 9.0$. In this case, γ_n and $\bar{c}_0$ are both equal to one within uncertainties for both 2D and 3D statistics and they match the null model of DMT. Such a case of (qualitatively) dimension-independent DMT has already been observed in the regime of amplitude turbulence in the CGLE [82] and in section 4.1.3. There remains, however, the quantitative difference in the average densities that we discussed above.

Finally, Figure 4.8b shows that the transition in the creation rate between 2D and 3D behavior close to the onset of DMT occurs rather sharply around $L_z \approx 20$, which is roughly of the order of the spiral wavelength in this regime. On the other hand, the shape ratio of the

distribution appears to vary much more slowly over the same range and appears to saturate only above $L_z \approx 70$. The presence of at least two critical thicknesses was anticipated from simple reasoning as the onset (loss of synchronization in the z-direction) and saturation of 3D behavior into "fully developed 3D turbulence" [141].

4.2.3 Discussion

It has been shown that, in cases such as the one we consider here where all species diffuse at the same rate, the stability of the straight scroll wave can never be worse than that of the 2D spiral [141]. Therefore, the change in turbulent statistics close to onset cannot be accounted for by a change in the linear instability of the straight scroll wave. On the other hand, the presence of growing filaments in the 3D medium and a positive linear dependence of the total creation rate in the DDDT regime suggest a behavior similar to the WT that is observed as a result of NLT instability. However, as we discussed before, the distinction

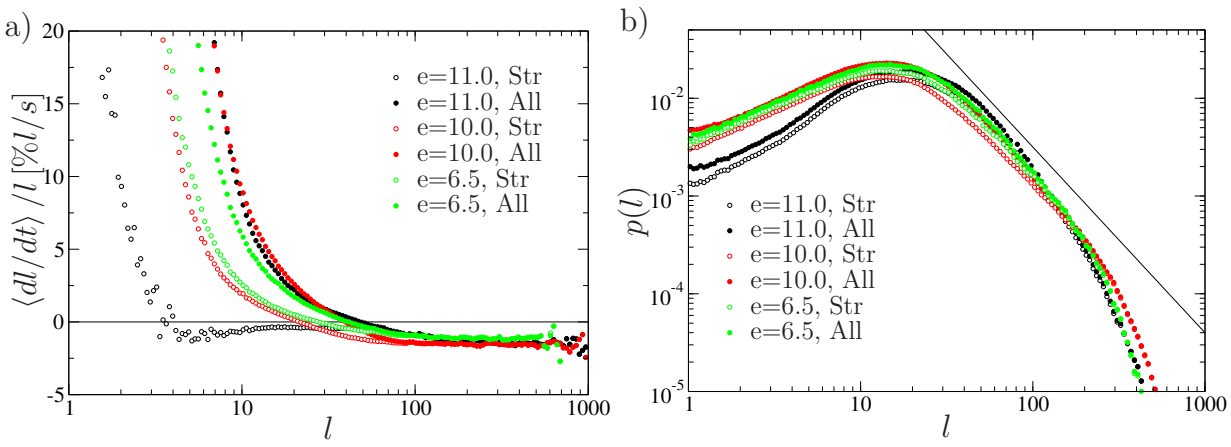

Figure 4.9: Average growth rate and length distributions of filament in the modified Bär model. Unlike NLT in the Barkley mode, here, small filaments grow and long filament shrink on average. While the distribution appears closer to exponentially decaying at $e = 11.0$, the other regimes may yield a power law decay, but the cutoff occurs too early due to the relatively small system size. The solid line shows a scaling of $p(l) \propto l^{-1.9}$ for comparison.

between filament growth driven turbulence and other mechanisms is that different filaments are responsible for the overall growth. Our previous observation of NLT in the Barkley model

and in the CGLE confirmed that long filaments grew on average whereas, in some of the AT regime and in this case (Figure 4.9), small filaments grow and long filaments shrink. This is one of the distinguishing elements of this mechanism of turbulence vs. NLT-induced WT.

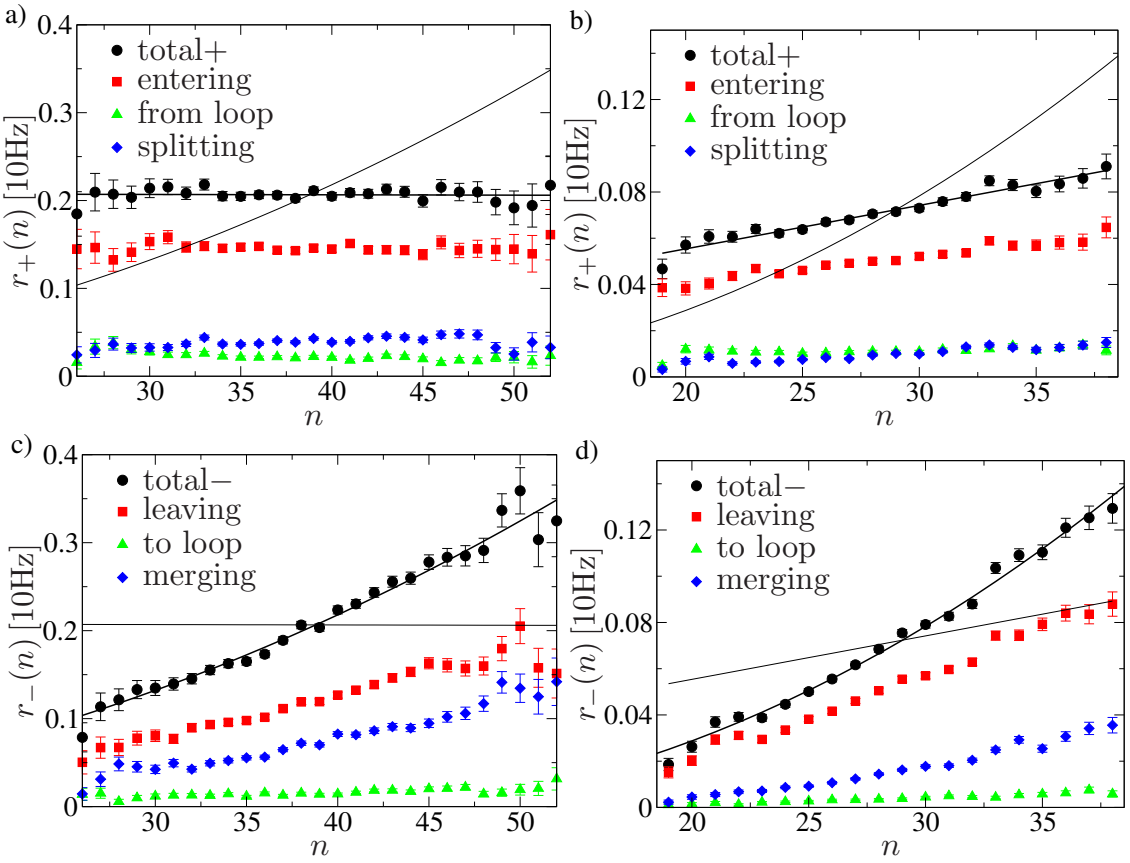

Figure 4.10: a) Decomposition of the surface defect creation rate based on the filament analysis far from onset at $e = 6.5$ and b) close to onset $e = 11.0$ with c-d) the corresponding annihilation rate decompositions. The creation and annihilation rate fits are shown as solid lines and are superimposed on both graphs to facilitate comparison. The annihilation rates in both cases seem to follow a linear plus quadratic relation.

Our filament tracking method also offers us more insight into the turbulence mechanism than what is readily available from surface measurements alone. Indeed, the creation of surface defects or strands actually occurs predominantly from conduction blocks in the bulk of the medium — corresponding to the generation of strands from rings and entering of strands — instead of from the elongation of the strands and collisions with the surface (splitting) as is the case for WT [142]. This is clearly demonstrated by comparing the decomposition of

the total creation rate into the different contributions: As shown in Figure 4.10b, there are significant contributions from all types of events for DDDT while only the filament splitting contribution is significant for a NLT-induced turbulent regime as discussed in Section 4.1. Also, if we only consider the relative contributions of each event type, we see that the decomposition is more or less the same in both regimes of the modified Bär model shown in Figure 4.10, which is also comparable to what can be observed in most regimes of amplitude turbulence in the CGLE (see figure 4.5 for an example). These observations suggest that the 2D spiral instability remains the driving factor of the turbulence in 3D in the modified Bär model in the DDDT regime.

In terms of the rates of surface defects, it must be noted that a pure 3D mechanism (like NLT) or the 3D turbulence mechanism close to onset presented here is not the only way by which the creation rate can acquire a linear contribution. For instance, Qiao *et al.* [107] presented rate estimates for the 2D Belousov-Zhabotinsky (BZ) reaction where both the creation and annihilation rates had an additional linear contribution, producing a widening of the distribution of vortices like we observe here for surface defects in the DDDT regime ($\gamma_n > 1$). However, the presence of many short-lived vortices in the experiments could indicate, though, that defects were not correctly identified, which in turn can lead to a spurious linear creation rate. Be that as it may, we have confirmed in Section 3.1.2 that even some regimes of the CGLE in 2D show deviations from the squared poissonian distribution of vortices [45] and we found that this is due to an additional linear contribution to the creation rates. Therefore, contrary to a previous conjecture [43], we cannot take a linear contribution to the creation rate of surface defects as a *prima facie* sign of a 3D breakup mechanism or instability and it is impossible to distinguish 2D from 3D breakup mechanisms on the basis of the surface creation rates alone. Yet, the decomposition of filament rates into different components sheds some additional light on the mechanism of turbulence, which seems to distinguish between turbulence arising from the pure filament instability NLT,

spiral breakup (assuming we are close enough to onset) and passive defect turbulence where defects behave as random independent entities, significantly extending earlier results [43]. It is important to realize though that the transition between the two latter cases does not have to be sharp as in the case of the modified Bär model, where the transition in behavior between DDDT and no-DDDT regimes occurs gradually.

4.3 Turbulence transition in other models and regimes

4.3.1 Core meandering instability in the Bär model

We first observed DDDT in the Bär model, as shown in figure 4.11, whose DMT regime results from the meandering-induced core breakup of spiral waves at $e_{\text{core}} \approx 14.38$ (shown in Figure 1.4a) above which meandering spirals are stable. The best linear fit for the creation rates of Figure 4.11a at $e = 13.5$ were estimated at $\bar{c}_0^{\text{2D}} = 1.23 \pm 0.09$ and $\bar{c}_0^{\text{3D}} = 0.15 \pm 0.06$. The corresponding distributions were also significantly different between 2D and 3D with $\gamma_n^{\text{2D}} \approx 0.45 \pm 0.04$ and $\gamma_n^{\text{3D}} \approx 1.04 \pm 0.07$. Unlike the modified Bär model, we cannot exclude the possibility of a concurrent 3D mechanism to account for the change in observed surface rate statistics, which was the main driving factor behind the investigation of the modified Bär model in the central exposition of this chapter. Nonetheless, the decomposition of the surface rates based on the filament identification method shown on Figure 4.11b suggests that the mechanism is very similar to the one observed in the modified Bär model, with all rate components contributing an amount comparable to what has been observed in that case and in AT in the CGLE.

There are, however, two main differences from the modified Bär model. First is the presence of hysteresis near the onset of the spiral instability. In this case, it is manifested by the coexistence of stable spiral and stable DMT. Second is that the 3D surface creation rate appeared to become purely linear ($\bar{c}_0^{\text{3D}} \approx 0$) close to the limit of stable DMT at $e = 14.5$ while, of course, the 2D rates in the same regime remained nearly constant ($\bar{c}_0^{\text{2D}} \approx 1$). This

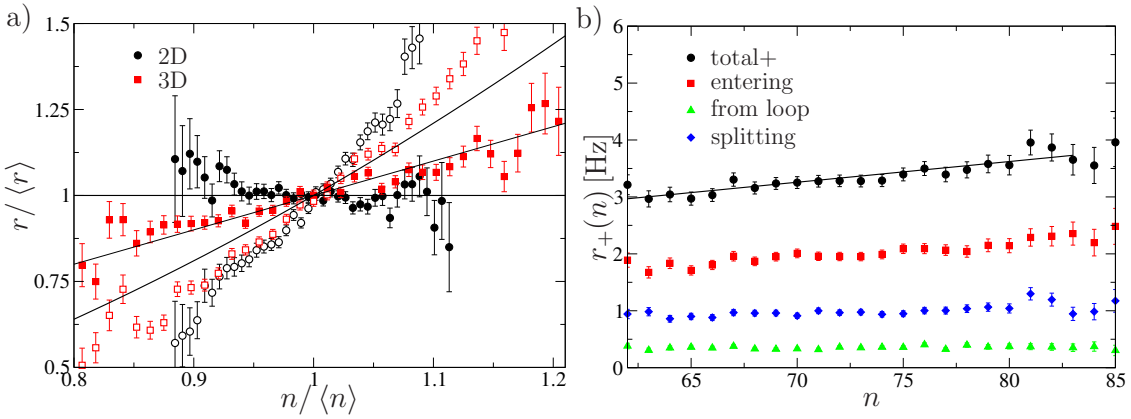

Figure 4.11: Bär model after the onset of the core instability at $e = 13.5$. a) Superposition of the normalized creation (full symbol) and annihilation (open symbol) rates of defects in 2D (circle) and surface defects in 3D (square). Like in the modified Bär model, the creation rates of defects in 2D simulations is significantly different from the corresponding 3D surface defects rates. In all the following figures, the solid lines are not the fit but idealized functional forms for the rates ($r = 1$, $r = n$ and $r = n^2$ in obvious order) to guide the eye in comparing the rates. b) The decomposition of the surface creation rates based on the filament tracking analysis shows the contributions from the various events types to the total surface creation rate in 3D. Here, all event types contribute even though the overall rate is almost purely linear.

is, insofar as we know, the only case where we have observed a purely linear creation rate with a, presumably, 2D mechanism. It is significant because a purely linear creation rate implies the existence of an absorbing state ($r_+(0) = 0$) which results in turbulence death i.e. the spontaneous termination of the turbulent state. In practice, even when this is the case, DMT can be sustained for an extremely long duration (thousands of oscillations and more) and, given a large enough system, its termination may never be observed. However, spontaneous termination of turbulence is a definite possibility for smaller systems and we have observed it in certain thin layers in that regime. In these cases, the 2D turbulence set by the initial conditions would convert into "real" 3D turbulence only to spontaneously die soon after. This may have important implications for VF and the control of VF in the heart, which will be discussed later.

4.3.2 Oscillatory regime of the modified Bär model

In the central section of this chapter, we have focused on the excitable regime of the modified Bär model. Now, let us briefly consider the case of the spiral breakup in the oscillatory regime ($b < 0$). We found that for $a = 0.84$ and $b = -0.045$, spiral breakup occurred at $e \approx 12.0$ (greater e values correspond to stable spirals). The instability is again difficult to classify. It occurs relatively close to the non-meandering core and the disturbances primarily travel outward while leaving the core itself intact during the initial breakup. Nevertheless, it appears closer to the core breakup phenomenology. Figure 4.12 shows the rates of the turbulent regime after onset at $e = 11.5$.

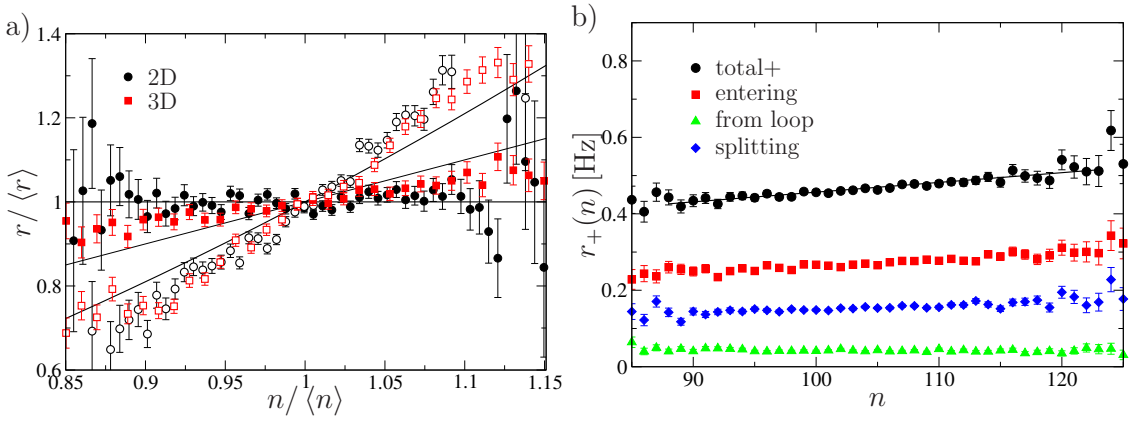

Figure 4.12: Modified Bär model in the oscillatory regime. a) Superposition of the normalized creation and annihilation rates of defects in 2D and surface defects in 3D (see Figure 4.11 for the interpretation of the symbols and curves). Like in the excitable regime close to onset of spiral turbulence, we observe that the rate of creation of defects in 2D and 3D surface defects is significantly different. b) The decomposition of the surface rates based on the filament tracking analysis shows the contributions from the various events, which is very similar to the contribution in the other regimes of the Bär and modified Bär models and in the AT regimes of the CGLE.

Using the same procedure as before, the best linear fits of the normalized creation rates in Figure 4.12a where found to be $\bar{c}_0^{2D} = 0.95 \pm 0.06$ and $\bar{c}_0^{3D} = 0.42 \pm 0.06$, indicating again that there is a significant but small linear contribution to the 3D surface rates that was absent in 2D. The shape ratio of the distribution of defects yielded $\gamma_n^{2D} = 0.58 \pm 0.04$ and

$\gamma_n^{3D} = 1.7 \pm 0.5$, the latter having a very large uncertainty, which is one of the common effects of the widening of the distribution: Large fluctuations make it harder to evaluate the statistical measures and longer simulation times are often required. Nevertheless, this falls within the expected behavior of DDDT. This observation is important because it shows that oscillatory regimes can also exhibit a similar dimensionality transition that we couldn't find in the CGLE. We shall show in the following that DDDT is not limited to the Bär and modified Bär model.

4.3.3 Alternans instability in the Karma model of action potential

We considered the onset of DMT as a result of the alternans instability of propagating wave trains emited by a spiral in the Karma model of excitable cardiac tissue. In some regimes, the spirals emit periodic waves with uniform action potential duration (APD). However, an unusually steep restitution curve (APD *vs.* preceding diastolic interval i.e. duration between two pulse maxima) has been shown to cause the waves emitted to undergo a period doubling bifurcation where subsequent APDs oscillate between short and long APD[103]. This may in turn degenerate into more complex APD oscillations and to spiral breakup and turbulence. Even though the Karma model is a highly simplified model (as are all models), it is much more faithful to real cardiac action potentials than the Bär model and its parameters correspond directly to common observables of cardiac dynamics. The Karma model is described by the following system of equations [143]

$$\begin{aligned} \partial_t E &= \gamma \nabla^2 E + \tau_E^{-1} \left(-E + \left[E^* - \mathcal{D}(n) \right] h(E) \right) \\ \partial_t n &= \tau_n^{-1} \left(\mathcal{R}(n) \theta(E - E_n) - \left[1 - \theta(E - E_n) \right] n \right) \end{aligned} \tag{4.1}$$

where $\theta(x)$ is the Heaviside function, and

$$\begin{aligned} h(E) &= \left[1 - \tanh(E - E_h) \right] \frac{E^2}{2} \\ \mathcal{R}(n) &= \frac{1 - \left[1 - \mathrm{e}^{-R_e} \right] n}{1 - \mathrm{e}^{-R_e}} \\ \mathcal{D}(n) &= n^M \end{aligned} \tag{4.2}$$

E represents a dimensionless transmembrane voltage which is largely dependent on the ionic conductance of the membrane and n represents a slow current gate variable. We used the following set of parameters: $M = 4.0$, $E^* = 1.5415$, $E_h = 3.0$, $E_n = 1.0$, $\tau_E = 2.5$ ms, $\tau_n = 50$ ms, $\gamma = 0.0011$ cm^2/ms and R_e, which controls the properties of the restitution curve [143], was used as the control parameter. The spiral breakup occurred as far-field (shown on Figure 1.4b) at $R_e = 1.16$ below which spirals were stable. We set $\Delta x = 0.04$ cm and $\Delta t = 0.1$ ms in our simulations and the system is sampled every 4 ms. The Karma model is an extremely stiff system of equations, as are all realistic and quasi-realistic models of cardiac AP, which makes the accumulation of sufficient data for the statistical measures more difficult than usual. We used the E field evaluated at $E_0 = 1.5$ and the $\partial_t E$ field evaluated at 0 to estimate the position of the defects with our isoline method (Section 2.2.1).

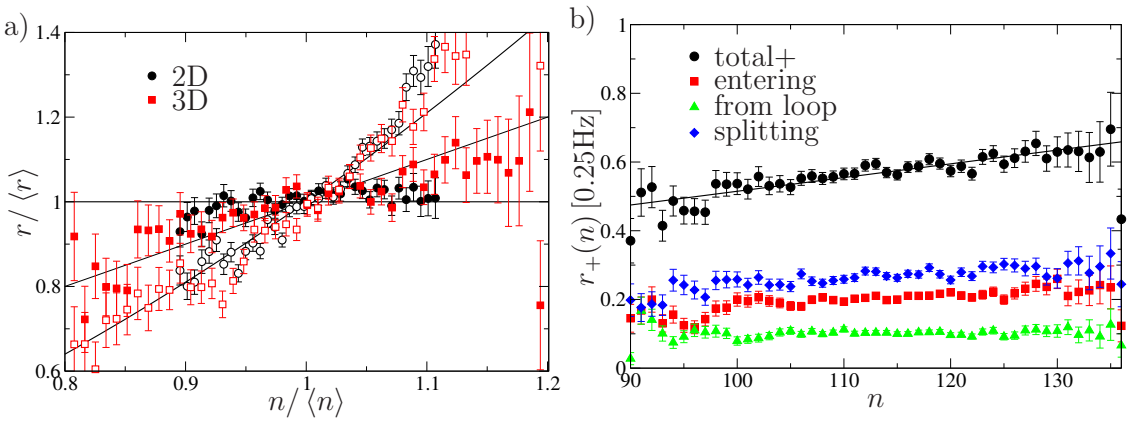

Figure 4.13: a) Normalized 2D and 3D surface creation and annihilation rates for a regime close to onset of an alternan spiral instability in the Karma model (see Figure 4.11 for the interpretation of the symbols and curves). There is a lot of noise but the tendency appears to be in line with what we have come to expect close to a spiral breakup instability. b) The 3D surface rate decomposition. All modes appear to contribute in this case, as was the case in the Bär model. However, the splitting component is larger than in the previous cases, which is reminiscent of what would be observed some distance away from onset of an NLT instability. We cannot exclude the possibility of the concurrence of multiple mechanisms.

We therefore produced a single data set at $R_e = 1.20$ after the onset of an alternan instability. Again, we observed a qualitative change in behavior between 2D and 3D surface

(see Figure 4.13) as has been observed in the Bär model close the the spiral instability. However, the discrepancy between 2D and 3D is much more subtle and, while this at least indicates that DDDT is likely to be present, a more detailed analysis would be required to assess the behavior as the instability is approached. In particular, the best linear fit for the creation rates were evaluated at $\bar{c}_0^{2\mathrm{D}} = 0.84 \pm 0.08$ and $\bar{c}^{3\mathrm{D}} = 0.22 \pm 0.08$, which is a significant deviation. On the other hand, the shape ratios of the distributions were evaluated at $\gamma_n^{2\mathrm{D}} = 1.02 \pm 0.12$ and $\gamma_n^{3\mathrm{D}} = 1.21 \pm 0.11$ which is very close, though in line with the general trend where $\gamma_n^{3\mathrm{D}} > \gamma_n^{2\mathrm{D}}$ for DDDT. While this does not prove the presence of DDDT in real cardiac medium, this certainly increases the likelihood of the applicability of DDDT for model of the heart dynamics and warrants further study. We shall discuss some of the consequences that this entails in the conclusion section.

4.3.4 Ising-Bloch transverse instability in a bistable medium

Finally, we also considered a model with a transversal instability of plane waves. The objective here was to contrast the DMT statistics resulting from this rather unique mechanism of breakup with the most common longitudinal instability of waves, which are defined in one spatially extended dimension, and the NLT-like instabilities, which are defined in three spatially extended dimensions. A transversal instability is defined in exactly two spatially extended dimensions which seems to provide an interesting classification of instabilities beyond the core/far-field dichotomy, which only applies for longitudinal instabilities. To test a transversal instability, we used the following FitzHugh-Nagumo (prototype of almost all activator/inhibitor model) type model

$$\begin{aligned} \partial_t u &= u - u^3 - v + \nabla^2 u \\ \partial_t v &= \varepsilon\,(u - a_0 - a_1 v) + \delta \nabla^2 v \end{aligned} \tag{4.3}$$

where the parameters a_0, a_1, ε and δ were set to -0.1, 2.0, 0.014 and 2.8 respectively [144]. This correspond to a regime after onset of a transversal instability of the domain wall between

the two resting states concurrent to an Ising-Bloch bifurcation of the front propagation (an "Ising" front propagating in one direction becomes a pair of "Bloch" fronts propagating in opposite directions). The tranverse instability of the front provides the initial symmetry breaking of the straight fronts which become counterpropagating Bloch fronts resulting in a new mechanism for the spontaneous creation of topological defects (the singular points that separate the counterpropagating fronts) [144]. Curiously enough, even though this state is not preceded by stable spirals, the topological defects still organize the medium around spiral-like fronts which yields a DMT state reminiscent of those that we have observed in excitable and oscillatory regimes so far. The discretization intervals were set to $\Delta t = 0.2$, $\Delta x = 2.0$. Finally, the defects were identified as the intersections of the isolines $u = 0$ and $v = 0$.

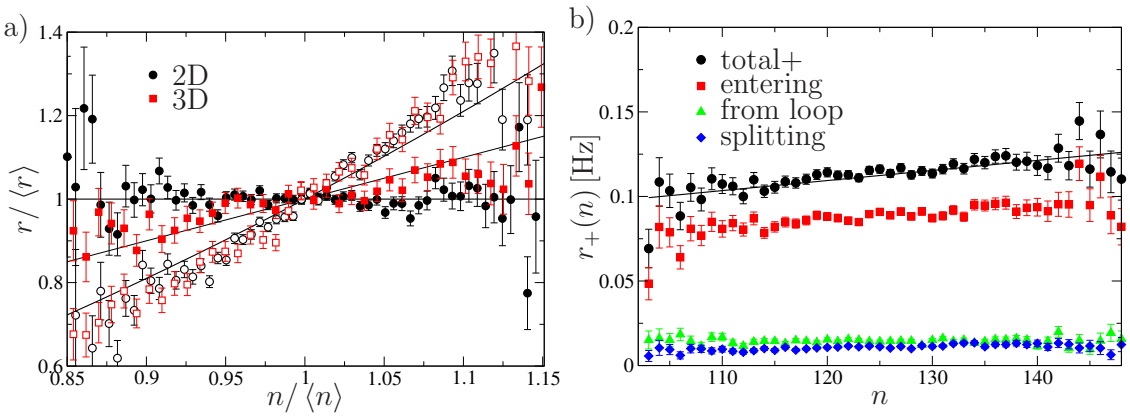

Figure 4.14: a) Normalized 2D and 3D surface creation and annihilation rates for a regime close to onset of a tranversal Ising-Bloch instability (see Figure 4.11 for the interpretation of the symbols and curves). b) Decomposition of the 3D surface rates based on the filament detection method. The entering mode is dominant which is a fairly unique feature of this mechanism (recall that in the NLT turbulent regime, it was the splitting mode that was dominant).

Figure 4.14 demonstrates a clear DDDT phenomenon i.e. a change in the creation rate function form from near constant in 2D to near linear in 3D. The best linear fit of the creation rates in Figure 4.14a are $\bar{c}_0^{2D} = 0.91 \pm 0.07$ and $\bar{c}_0^{3D} = 0.36 \pm 0.06$ yielding a significant difference. The change of turbulence is also easily assessed though the shape ratio

of the distribution of surface defects with $\gamma_n^{2D} = 0.77 \pm 0.06$ and $\gamma_n^{3D} = 1.07 \pm 0.12$. Unlike the other regimes however, a very large fraction of the creation events in 3D is attributable to the entering mode in Figure 4.14b, which makes this mechanism of breakup rather unique in that respect. It may be that these filaments lack the mobility of those in the previous regimes and therefore are less likely to collide whereas the creation of new defects (entering) is systematically driven by the emission of new fronts (which are unstable) by the existing spiral-like cores. While this creates more question than answers (we don't know how generic this behavior is or the reason behind the difference in the dominant modes of creation), it serves to put into sharp relief the large variety of rates in DMT regimes resulting from different instabilities.

4.3.5 Discussion

We observed a similar DDDT behavior among many systems in turbulent regimes following various instabilities in excitable, oscillatory and bistable media. We conjecture that such dimension dependent mechanisms of turbulence are ubiquitous. In a different study, Clayton [59] measured the average filament event counts in various regimes of a simplified 3-variable ionic model of cardiac tissue kinetics and found a significant amount of both birth (creation and entering in our notation) and division (splitting and shedding) of filaments in all regimes. While not providing direct evidence of DDDT, the presence of multiple conduction blocks, i.e. creation of new filaments far from existing ones, inside the medium suggests a mechanism of turbulence that is either not purely 3-dimensional or far from onset. This again emphasizes the potential relevance of the DDDT mechanisms, and that of characterizing correctly the turbulent dynamics that results, in the context of VF.

Returning to the idea of IDDMT, all the previous observations fall under the classification scheme presented in Table 4.1. The DDDT behavior observed for all instability types implies that the apparent identification scheme in 2D collapses in 3D or quasi-3D contexts. These dimension-dependent mechanisms of turbulence are nonetheless different from those

Type of breakup		$\bar{c}_0^{2D}$	γ_n^{2D}	$\bar{c}_0^{3D}$	γ_n^{3D}	Section references
Far-field	(1D)	any	any	$\leq \bar{c}_0^{2D}$	$\geq \gamma_n^{2D}$	Sections 4.1.3, 4.3.2 and 4.3.3.
Core	(1D)	≥ 1	< 1	$\leq \bar{c}_0^{2D}$	$\geq \gamma_n^{2D}$	Sections 4.2.2 and 4.3.1.
Transverse	(2D)	≤ 1	< 1	$\leq \bar{c}_0^{2D}$	$\geq \gamma_n^{2D}$	Section 4.3.4.
Filament	(3D)	—	—	≈ 0	> 1	Section 4.1.

Table 4.1: Tentative classification of the breakup mechanism based on their turbulence statistics close to onset. "Any" indicates that the measured values were in a wide range depending on the particular system and regime for that type of instability, and that we couldn't identify any apparent regularity. The results for the transverse instability are also particularly ambiguous and would require further corroboration. One of the limiting factors in testing these hypotheses is the lack of accurate values of these observables in the literature.

produced by a pure 3D instability like the NLT, which exists in a region where 2D spirals are stable and yields qualitatively different *filament statistics*, though they may virtually have the same *surface statistics*.

It is not yet clear what the general conditions for the presence of DDDT are. However, there seem to be only two common features to all regimes we have observed. First is that all the cases of DDDT we have observed corresponded to regimes that were, in some sense, far from the onset of oscillations. This is marked in our investigation of the Bär and modified Bär models where, as we progress closer to the Hopf bifurcation, DDDT disappears first, then the excitable dynamics is replaced by an oscillatory one up to the Hopf bifurcation. The excitable dynamics are, in this sense, always far from the onset of oscillations which may account for the apparent ubiquity of DDDT in these systems. Furthermore, while this may appear coincidental, the fact that we weren't able to observe DDDT in the CGLE tends to support this hypothesis. The second common feature is the presence of well-defined local spiral structures amidst the turbulence. Once these local structures are broken sufficiently and the pattern appears to be random, the defects become passively advected from the chaotic dynamics of the fields and so, it appears, the dimensionality of the medium ceases to matter (from the point of view of surface observables). It is the case for most of the T2 regime in the Bär and modified Bär models (see Figure 3.12) as well as in the AT regime in the CGLE (see Figure 3.2). Although this does not offer an explanation of the phenomenon, this

suggests a simple way to test for suitable DDDT regimes based on simple 2D observations.

4.4 Chapter summary

We have made many new observations of DMT and concluded that the 2D and 3D surface turbulence are often statistically different even when the (linear) instability at onset are the same. In the case of the modified Bär model close to onset, the defects in 2D media appeared to have a stabilizing effect whereas the surface defects in 3D media appeared to have a destabilizing (self-enhancing) effect. Yet, other regimes showed indistinguishable 2D/3D surface defect turbulence. Our results illustrate the limitations of simplified 2D models in representing complex 3D phenomena. This is particularly relevant in the case of ventricular fibrillation in the heart where the importance of the thickness is contentious. Even if a relevant breakup mechanism was 2D in nature, the thickness and geometry of the medium may still play an important role in determining the statistics and complexity of the turbulent state and, as such, is essential to our understanding of the system as a whole. It would be interesting to see if DDDT can be observed in an experimental system such as the BZ reaction, where simple filament motions have been measured in 3D using various tomographic techniques [76, 77, 145]. The question whether DDDT can be linked to certain instabilities or breakup mechanisms remains a challenge for the future but might have further important implications in diverse settings such as optical systems [146], superfluid turbulence [147] — including Bose-Einstein condensates [148] — and cosmology [149] as well as the morphogenesis of slime mold [16].

Chapter 5

Conclusion

In a seminal paper [51], Winfree posited that VF was an essentially 3D phenomenon on account of both 2D simulations and thin slab experiments only yielding normal re-entry. This form of turbulence has been named autowave turbulence to distinguish it from hydrodynamic turbulence but the term fell into disuse. In general however, both 2D and 3D wave turbulence may co-exist and Biktashev [75] surmised that "Autowave turbulence [...] is essentially a three-dimensional behavior, qualitatively different from whatever may happen in the same system in two dimensions", and that "It would be interesting to compare properties of these different [2D] instabilities and chaos generated by them, to see if the 3-D autowave turbulence is also much more complicated than the 2-D one." We believe that we have done that here for the first time by exploring some aspects of the qualitative and quantitative DMT states resulting from various instabilities in 2D and 3D media. We conclude that the dimensionality of the medium provides the possibility for more complex excitation patterns as described by the wider distribution of defects relative to 2D. This has important implications for real media and simulations alike.

5.1 Summary of the new results

Let us briefly review what are the new results and technical progress we have made in our investigation of the phenomenon of defect turbulence.

In Chapter 2, we have developed new and original methods for detecting defect events in 2D and 3D that didn't suffer from many of the drawbacks or limitations of previous methods. All the methods have been shown to yield consistent results in a suitable limit and in a case where the statistical features are known *a priori*. We have also shown experimentally that

a rate estimator based on randomly independent defect events converged to the appropriate limit faster and makes more sense intuitively for large spatially extended systems. When the rate of events is small (much smaller than one per frame analyzed), it makes no difference what estimator is used. This is a significant improvement over the previous method because it allows measurement of rates in large systems.

In Chapter 3, we have confirmed that deviations from the null model's rate functional form can be found in the CGLE. We have measured directly that the deviations resulted primarily from a constant plus linear creation rate and found that the deviations were strongest close to onset of DMT before the onset of the absolute instability. In a spatially extended biochemical model system, we have shown that a secondary Hopf bifurcation of the local dynamics induced a DMT state qualitatively similar to what could be observed in the CGLE far from onset. Nonetheless, many observables showed idiosyncrasies. In the Bär and modified Bär models of excitable dynamics, the defects close to onset of a spiral instability had a stabilizing effect which seems to be related to the presence of local spiral structures. Furthermore, we have shown that the onset of the backfiring instability, an instability of the traveling wave train, corresponds roughly to the onset of turbulence whose statistical feature are indistinguishable from AT in the CGLE as described by the null model. Incidentally, this also corresponds in both cases to an extremely turbulent wave pattern with no local spiral structures. Finally, we have shown that all the 2D models above had similar spacetime defect loop statistics scaling for long defect loops close to the Hopf bifurcation. However, non-scaling distributions appeared close to onset of the spiral instability in the modified Bär model.

In Chapter 4, we have seen that two purely 3D turbulent regimes in oscillatory and excitable media close to the onset of the filament instabilities have comparable statistics, as characterized by the rate decompositions and the growth rate distributions. Therefore, both regimes support a similar instability-driven mechanism of turbulence which was shown

to have idiosyncratic surface observables close to onset, but can deviate substantially from the onset behavior even in the same regime. The regimes of AT in the CGLE were shown to have the same 2D and 3D surface defect statistics, which can be different from the null model's. This indicates that the surface turbulence mechanism, and by extension the 3D mechanism, is in all likelihood the same as the 2D turbulence mechanism and that the filaments, like the defects in AT, behave as passive objects. On the other hand, simulations of the modified Bär model close to onset of the spiral instability indicate a change between 2D and 3D mechanisms of turbulence. Whereas 2D defects had a stabilizing effect, 3D surface defects have a self-enhancing (destabilizing) effect. This transition disappears far from onset, along with the local patterns, and the null model of defects is recovered. Furthermore, the transition cannot be accounted for by a purely 3D linear instability due to the special nature of the modified Bär model. Finally, we have compared the 2D and 3D surface rates (as well as other measures on which we have put less emphasis) close to the onset of various instabilities in many paradigmatic systems. We have found that a change in mechanism between 2D and 3D was ubiquitous and that certain instabilities produced idiosyncratic rate decompositions, while others were virtually indistinguishable from the previous mechanisms.

The previous set of observations between 2D and 3D surface turbulence can be written concisely as

$$c_0^{3\mathrm{D}} \leq c_0^{2\mathrm{D}} \quad \text{and} \quad \gamma_n^{3\mathrm{D}} \geq \gamma_n^{2\mathrm{D}} \tag{5.1}$$

where both inequalities are independent and with the equality applying close to onset of a Hopf bifurcation, but not necessarily exclusively. The second observation is that the null model of DMT

$$c_0^{2\mathrm{D}} \to 1.0 \quad \text{and} \quad \gamma_n^{2\mathrm{D}} \to 1.0, \tag{5.2}$$

which we have equated to fully developed defect turbulence, is only recovered in certain cases far from onset, independently of the first observation. Amplitude turbulence, also named strong turbulence, in the CGLE is not always fully developed in this sense.

We do not have a theory to test against these findings, or to help us order them to extract the significant part. However, these results have some important implications for potential theories and practical applications as well.

5.2 Applications

5.2.1 Identifying instabilities

How do the previous findings reflect on the question of the distinguishability of turbulent states maintained by different mechanisms? First from the perspective of the rates, even if *certain* instabilities result in different forms with evident strong correlations close to onset, there does not seem to exist a one-to-one correspondence between the instability, nor the type of instability (core, far-field, transverse, or purely 3D), and specific characteristics of the surface rates. For instance, the surface linear rates that are produced as a result of a purely 3D instability of scroll waves, which may have appeared unique at first [43, 82], are now clearly possible for 2D mechanisms as well, as was the case of the destabilizing effect found in the CGLE. Furthermore, our observations of DDDT imply that many 2D mechanisms produce linear surface creation rates in a 3D medium. Therefore, in spite of an apparent weak version of IDDMT and taking into account the variability and the difficulty to characterize the annihilation rate in a meaningful fashion, identification of mechanisms from surface measurements appears impossible.

On the other hand, the rate decompositions seem to reveal some interesting features that would distinguish pure 3D instabilities from the very broad range of 2D instabilities — which, whether core, far-field or transverse, always create new defects some distance away from existing ones (conduction blocks). However, the distinction is not clear cut, and the precise relative values of each creation mode always depend on the distance to the instability. For instance the strand splitting component is the only significant channel for the WT regime in the Barkley model, and in the CGLE, only close to onset of the filament instability. Far

from onset, the other creation modes become more and more dominant such that, far enough away, but still in the same regime, no deduction can positively be made *a posteriori* on the generating instability. The filament growth rates also showed some interesting behavior but their utility is so far limited to a characterization of potential model parameters.

5.2.2 Relevance to heart dynamics

The main point of interest to the heart community is whether or not the instability leading to VF is of 3D nature. There are, of course, many more types of instabilities that are possible in cardiac tissue than those we have investigated here in our simplified systems and geometries. However, there remains a clear distinction between instabilities that are two dimensional in nature (like instabilities due to inhomogeneities in conduction velocity) and those that require three dimensions (like instabilities due to intramural rotation of the fibers a.k.a. rotational anisotropy). Contrary to a previous assessment by Davidsen *et al.* [43], we have shown that there is no apparent unique link between a linear creation rate of surface defects and the 3D nature of the generating instability. Therefore, even if we were able to somehow gather significant statistical surface data of a fibrillating heart and observed a linear dependency of the creation rate, it would not necessarily imply a 3D mechanism. Furthermore, we also have argued above that even complete information about the filament statistics would likely not resolve this question because of the "close to onset" requirement, which may be difficult to control in a diagnostic setting.

Nonetheless, there is a significant observation in the experimental studies of the heart dynamics during fibrillation which is that the defects (or filaments) *do* organize the activation patterns in the sense that there are active local structures (spirals or rotors) [19, 134]. Such was also the case in every model and regime where we observed DDDT, excitable media or not. Therefore, whether the mechanism of breakup is 2-dimensional or 3-dimensional (or both), the relevant dynamical state will likely have to be 3-dimensional. This justifies the general direction of research moving toward 3D models of the heart.

This has important consequences because, even if the mechanism is 2-dimensional and that, say, a thin 2D layer shows sustained DMT, it may very well be that a suitably 3D ventricle in the same "parameter" regime would show sudden recovery from VF. This is a surprising result. The reason is that if the 2D DMT regime corresponds to DDDT, transforming the 3D surface creation rate to a more linear functional form, the new 3D dynamics may now include an absorbing state $r_+(0) = 0$ which corresponds to the termination of VF. Furthermore, reducing the effective volume of the system, with drugs that increase the wavelength of the spirals, would make the visit to this absorbing state more likely which may provide an effective way to return to normal excitation without defibrillation. This is an example of why, while the mechanisms that lead to turbulence are important, the statistical description of the resulting states are also important and essential for a full understanding of the system and the mechanisms of control of turbulence.

Many other factors would need to be investigated more thoroughly to reach a better understanding on how to interpret the statistical features of turbulence in a real-world system like the heart. A first step would be to relax certain simplifications we have held during this thesis. Clearly, the tissue homogeneity, isotropy and the simple geometry we have employed should be the first to go. Another important aspect of the heart is the mechanical coupling: Excitations trigger contractions which deform the medium which in turn affect wave propagation. While some of these factors have been investigated in a number of studies and they were found to either promote new instabilities [50, 20, 150, 151] or to coarsely influence the number of surface defects [152, 59, 153], we have yet to see an analysis that take a statistical view of the turbulent state as we have done here.

Appendix A

Numerical integration, boundary conditions and anisotropic diffusion

In this section, we will discuss briefly the numerical integration scheme and develop in detail the diffusion kernels in a situation where the diffusion is anisotropic but otherwise homogeneous[1] and where we only know the diffusion coefficients along some orthogonal directions, generally different than those of our coordinate system.

A.1 Integration scheme

The simplest forward Euler integration scheme is often used in the studies of nonlinear dissipative ordinary differential equation (e.g. [79, 35, 154, 136, 82] and many others all used an explicit finite difference (first-order) integration scheme.). The reason is that, even though it would sacrifice a great deal of precision of the solution, we are only interested in a typical solution and the inherent dissipation insures it remains in such a regime i.e. that the trajectories remain on the attractor but the particular trajectory on the attractor (small scale features) can be fairly different than the actual one. The same kind of idea applies to partial differential equations. The most important consideration for such a scheme is the stability of the solution which, for the forward integration of a reaction-diffusion system, is given by the well-known criterion [155, p. 1044]

$$\frac{D\Delta t}{\Delta x^2} \leq \frac{1}{2d}, \tag{A.1}$$

where d is the dimensionality of the system. As it turns out, in our procedure, we either use first-order or second-order (midpoint method) forward integration. The reason for using

[1] We only used the isotropic case in this thesis, but the anisotropic case is more general and allows us to clarify the meaning of the so-called 9-point Laplacian we used in [36]

a higher order scheme is that in some particular cases, first-order integration would yield some unusual features at the scale we were most interested in e.g. squarish spiral waves. This phenomenon can be alleviated by using a larger kernel known as the 9-point Laplacian. However, we noticed it can be alleviated more naturally by using the standard 5-point Laplacian with a higher order integration routine, and that second order was sufficient. Figure A.1 shows the rates of convergence of the estimated error on the solution with finer discretizations. We find an exponent of 1.55 for the scaling of the estimated error as a function of the spatial discretization. The estimated error decreases even faster with an exponent of 2.13 as Δt is varied with constant Δx.

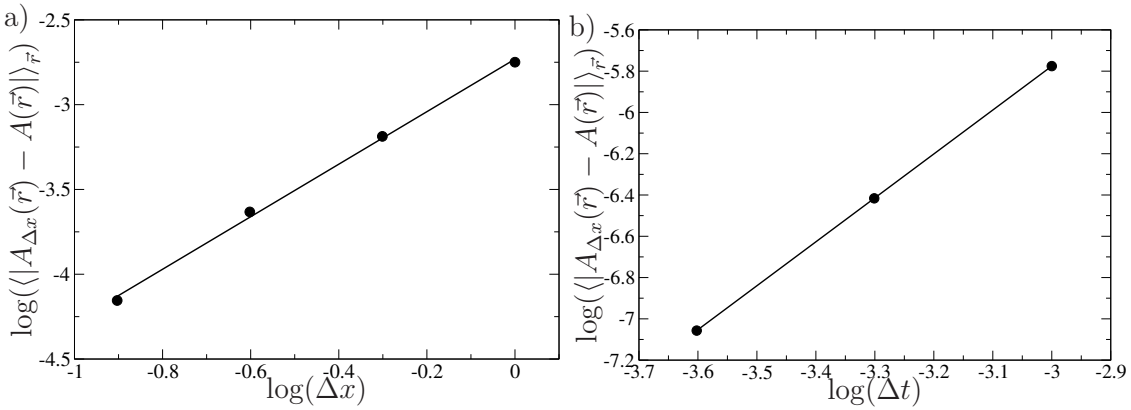

Figure A.1: Rate of convergence of the solution of the CGLE with the second order explicit Euler integration method. a) With a spatial discretization Δx. The best fit yields a rate of 1.55. b) The same procedure yields a convergence rate of 2.13 with decreasing Δt.

Whether one choose a first or a second order integration scheme (or any order for that matter), the basic operation is always how to perform a single forward step. Discretizing the continuous fields such that $x_i = x_0 + i\Delta x$, $y_j = y_0 + j\Delta y$, $t = \tau\Delta t$ and $A^{\tau}_{i,j} \equiv A(x_i, y_j, t)$, one discrete integration step is simply

$$\frac{A^{\tau+1}_{i,j} - A^{\tau}_{i,j}}{\Delta t} = \vec{K}_{i,j}\left[A^{\tau}_{i,j}\right] + \vec{R}\left[A^{\tau}_{i,j}\right], \tag{A.2}$$

where $\vec{K}_{i,j}[\cdot]$ are the kernels (an estimator of the diffusion term) whose forms depend on the boundary conditions. We decribe how to evaluate them in the next section.

A.2 Anisotropic kernel

We consider the general diffusion operator of the form

$$\vec{\nabla} \cdot (\hat{D}\vec{\nabla}) \tag{A.3}$$

where

$$\hat{D} = \begin{pmatrix} D_{xx} & D_{xy} \\ D_{yx} & D_{yy} \end{pmatrix} \tag{A.4}$$

and

$$\begin{aligned} D_{xx} &= D_{\parallel}\cos^2\theta + D_{\perp}\sin^2\theta \\ D_{yy} &= D_{\parallel}\sin^2\theta + D_{\perp}\cos^2\theta \\ D_{xy} &= D_{yx} = (D_{\parallel} - D_{\perp})\cos\theta\sin\theta. \end{aligned} \tag{A.5}$$

Expanding Eq. A.3, we get

$$\vec{\nabla} \cdot (\hat{D}\vec{\nabla}) = D_{xx}\partial_x^2 + D_{yy}\partial_y^2 + 2D_{xy}\partial_x\partial_y. \tag{A.6}$$

Now we evaluate these three partial differential operators based on the Taylor expansion of a field A

$$\begin{aligned} A(x_{i+k}, y_{j+l}) &= \sum_{m,n=0}^{\infty} \frac{(x_{i+k} - x_i)^m (y_{j+l} - y_j)^n}{m!n!} \partial_x^m \partial_y^n A(x,y)|_{x_i,y_j} \\ A_{i+k,j+l} &= A_{i,j} + k\Delta x \partial_x A_{i,j} + l\Delta y \partial_y A_{i,j} \\ &+ \frac{1}{2}\left(k^2\Delta x^2 \partial_x^2 A_{i,j} + l^2 \Delta y^2 \partial_y^2 A_{i,j} + 2kl\Delta x\Delta y \partial_x\partial_y A_{i,j}\right) + O(3) \end{aligned} \tag{A.7}$$

where $k\Delta x = x_{i+k} - x_i$ and $l\Delta y = y_{j+l} - y_j$. All that remains is to take the proper combinations to extract the three second differential operators

$$\begin{aligned} \Delta x^2 \partial_x^2 A_{i,j} &= A_{i+1,j} + A_{i-1,j} - 2A_{i,j} \\ \Delta y^2 \partial_y^2 A_{i,j} &= A_{i,j+1} + A_{i,j-1} - 2A_{i,j} \\ \Delta x\Delta y \partial_x\partial_y A_{i,j} &= \frac{1}{4}\left(A_{i+1,j+1} + A_{i-1,j-1} - A_{i-1,j+1} - A_{i+1,j-1}\right). \end{aligned} \tag{A.8}$$

Plugging these estimators into Eq. A.6 and absorbing the delta into the diffusion coefficients $D_{xx} \leftarrow D_{xx}/\Delta x^2$, we obtain the desired diffusion kernel

$$\begin{aligned} K_{i,j} &= D_{xx}\left(A_{i+1,j} + A_{i-1,j} - 2A_{i,j}\right) + D_{yy}\left(A_{i,j+1} + A_{i,j-1} - 2A_{i,j}\right) \\ &+ \frac{D_{xy}}{2}\left(A_{i+1,j+1} + A_{i-1,j-1} - A_{i-1,j+1} - A_{i+1,j-1}\right). \end{aligned} \tag{A.9}$$

The second task is to evaluate the kernel with different boundary conditions. Periodic is trivial, let's consider "no-flux" in detail.

A.3 No flux boundary conditions

In numerical simulations, the position indexes $i \in [0, M[$ and $j \in [0, N[$ are bounded and the previous kernel needs to be modified at the boundaries. The no-flux boundary condition is easily expressed as

$$F = \hat{n} \cdot \hat{D} \nabla A = 0 \tag{A.10}$$

where $\hat{n}$ is the normal vector at the boundary. Let's consider the upper boundary in the x-direction where $\hat{n} = (1, 0)$. We have

$$D_{xx}\partial_x + D_{xy}\partial_y = 0. \tag{A.11}$$

The centered first-order derivatives (which is also incidentally the average of the left and right derivatives) are

$$\begin{aligned} \Delta x \partial_x A_{i,j} &= \frac{1}{2}(A_{i+1,j} - A_{i-1,j}) \\ \Delta y \partial_y A_{i,j} &= \frac{1}{2}(A_{i,j+1} - A_{i,j-1}). \end{aligned} \tag{A.12}$$

Using also the forward derivative at the boundary itself and absorbing the Δs in the diffusion coefficients, we find at $i = M - 1$ that the flux is

$$F = D_{xx}(A_{M,j} - A_{M-1,j}) + \frac{D_{xy}}{2}(A_{M,j+1} - A_{M,j-1}) = 0$$

and we find that

$$A_{M,j} = A_{M-1,j} - \frac{D_{xy}}{2D_{xx}}(A_{M,j+1} - A_{M,j-1}). \tag{A.13}$$

Putting it all together, we find

$$\begin{aligned} K_{M-1,j} &= D_{xx}\partial_x^2 A_{M-1,j} + D_{yy}\partial_y^2 A_{M-1,j} + 2D_{xy}\partial_x\partial_y A_{M-1,j} \\ &= D_{xx}\left(A_{M-2,j} - A_{M-1,j} - \frac{D_{xy}}{2D_{xx}}(A_{M,j+1} - A_{M,j-1})\right) \\ &\quad + D_{yy}\left(A_{M-1,j+1} + A_{M-1,j-1} - 2A_{M-1,j}\right) \\ &\quad + \frac{D_{xy}}{2}\left(A_{M,j+1} - A_{M,j-1} + A_{M-2,j-1} - A_{M-2,j+1}\right) \\ &= D_{xx}\left(A_{M-2,j} - A_{M-1,j}\right) + D_{yy}\left(A_{M-1,j+1} + A_{M-1,j-1} - 2A_{M-1,j}\right) \\ &\quad + \frac{D_{xy}}{2}\left(A_{M-2,j+1} - A_{M-2,j-1}\right) \end{aligned} \tag{A.14}$$

which is equivalent to the general kernel (Eq. A.9) with the following substitutions

$$\begin{aligned} A_{M,j} &\rightarrow A_{M-1,j} \\ A_{M,j+1} &\rightarrow 0 \\ A_{M,j-1} &\rightarrow 0 \end{aligned} \tag{A.15}$$

since $A_{M,j+1}$ and $A_{M,j-1}$ are otherwise arbitrary and only have to cancel here. For the lower boundary kernel, we use the same method with $\hat{n} = (-1, 0)$ and we find that the replacement

$$\begin{aligned} A_{-1,j} &\rightarrow A_{0,j} \\ A_{-1,j+1} &\rightarrow 0 \\ A_{-1,j-1} &\rightarrow 0 \end{aligned} \tag{A.16}$$

would produce no flux at that boundary and so on for the other boundaries.

A.4 Clarification regarding the 9-point Laplacian

In the previous section, we derived *a* 9-point Laplacian operator for the general case of anisotropic diffusion. However, it is customary to reserve the name "9-point Laplacian" to

a different estimator of the isotropic Laplacian. From the Taylor expansion of the A-field (Eq. A.7), we can derive an alternative discretized Laplacian operator at once using the following combination

$$\begin{aligned}
\frac{1}{2}\left(\Delta x^2\partial_x^2 A + \Delta y^2\partial_y^2 A\right) &= A_{i+1,j+1} - A_{i,j} - \Delta x\partial_x A - \Delta y\partial_y A - \Delta x\Delta y\partial_x\partial_y A + O(3) \\
&= A_{i-1,j-1} - A_{i,j} + \Delta x\partial_x A + \Delta y\partial_y A - \Delta x\Delta y\partial_x\partial_y A + O(3) \\
&= A_{i-1,j+1} - A_{i,j} + \Delta x\partial_x A - \Delta y\partial_y A + \Delta x\Delta y\partial_x\partial_y A + O(3) \\
&= A_{i+1,j-1} - A_{i,j} - \Delta x\partial_x A + \Delta y\partial_y A + \Delta x\Delta y\partial_x\partial_y A + O(3) \\
\hline
2\left(\Delta x^2\partial_x^2 A + \Delta y^2\partial_y^2 A\right) &= A_{i+1,j+1} + A_{i-1,j-1} + A_{i-1,j+1} + A_{i+1,j-1} - 4A_{i,j}.
\end{aligned}$$

Assuming $\Delta x = \Delta y$ and averaging with $\Delta x^2\nabla^2 = A_{i+1,j} + A_{i-1,j} + A_{i,j+1} + A_{i,j-1} - 4A_{i,j}$ we find the 9-point Laplacian

$$\begin{aligned}
4\Delta x^2\nabla^2 A &= -12A_{i,j} + 2\left(A_{i+1,j} + A_{i-1,j} + A_{i,j+1} + A_{i,j-1}\right) \\
&+ \left(A_{i+1,j+1} + A_{i-1,j-1} + A_{i-1,j+1} + A_{i+1,j-1}\right). \qquad \text{(A.17)}
\end{aligned}$$

Of course, this procedure could be extended to higher order. However, it is not clear to this author how this can be generalized for anisotropic diffusion. And there lies the distinction, the customary "9-point" Laplacian is the average value of two second-order-accurate estimators of the isotropic diffusion operator whereas the 9-point Laplacian we derived explicitly in Section A.2 is a unique second-order-accurate estimator of the anisotropic diffusion operator.

A.5 Setting up the initial conditions

Setting up the initial state of the system is crucial since most systems investigated show multistability. The trivial case is with the homogeneous state which may remain forever homogeneous and uninteresting. Hence we need to set a non-trivial initial state. Also, it is sometimes useful to know how to set a particular state to test the stability or the initial behavior of that state, since it may be difficult or impossible to reach it as a result of the

normal activity of the system. A typical example is a filament ring. Filament rings form naturally during filament turbulence. However, their characteristic rate of growth may be difficult to assess in the presence of the perturbation caused by the rest of the turbulent medium. For such a case, it is preferable to set the ring state manually and free of other neighboring structures.

A.5.1 For oscillatory media

Spiral waves are easily set up in oscillatory media. If one knows approximately the wavelength of the pattern, one can use an exact spiral or wavetrain pattern directly and adjust the amplitude, phase and center at will. The system would then usually adapt pretty easily to its natural oscillation, which might be very different from the initial pattern. Large discontinuities in the value of the field are generally acceptable. In many cases where one wants to generate a single spiral, it is sufficient to produce a correct phase ordering in 4 quadrants ($\phi_1 \to \phi_2 \to \phi_3 \to \phi_4$) to start a flow and a spiral would form naturally out of the central singularity. The values of the phases are determined by the time ordering of an isolated oscillation and hence gives the direction of rotation. The same quadrant method can be used to generate more complex structures like multiple spiral states.

A.5.2 For excitable media

Excitable media are characterized by the stability of a fixed point (the rest state). Unlike oscillatory media, setting up a phase singularity with the quadrant method would instead rapidly result in a return to the rest state after all the initial nonlinear waves have collided or traveled through the system and no spiral would be created. The solution is to use the directionality of the propagating wave fronts to our advantage. The general RD equation can be modified to

$$\partial_t A(\vec{r},t) = \vec{\nabla} \cdot D\vec{\nabla} A + f(A) + I(\vec{r},t) \tag{A.18}$$

where $I(\vec{r}, t)$ is a localized stimulus current applied locally in the medium. We also often need to return a part of the medium to the rest state. Even though this can be induced by exciting that part of the medium, it is often easier and more efficient in simulations to simply set $A(\vec{r}, t)$ to the rest state directly.

Spirals in excitable media are easily produced by first creating a plane wave that propagates in one direction (say $\hat{x}$) with a current applied close to $x = 0$ along the whole y-axis and then by resetting half of the medium in the orthogonal direction when the pulse has reached the center of the medium. This produces a broken wave front which immediately start to curl and re-exite the region that has been reset, producing a complete spiral wave after a few periods.

Bibliography

[1] Merriam-Webster. *Merriam-Webster's Collegiate Dictionary, 11th Edition thumb-notched with Win/Mac CD-ROM and Online Subscription*. Merriam-Webster, 2003.

[2] S. Strogatz. *Nonlinear Dynamics And Chaos: With Applications To Physics, Biology, Chemistry, And Engineering*. Studies in Nonlinearity. Westview Press, 2001.

[3] I. Shimada and T. Nagashima. A numerical approach to ergodic problem of dissipative dynamical systems. *Prog. Theo. Phys.*, 61(6), 1979.

[4] J. P. Eckmann and D. Ruelle. Ergodic theory of chaos and strange attractors. *Rev. Mod. Phys.*, 57(3):617–656, 1985.

[5] M. Sano and Y. Sawada. Measurement of the lyapunov spectrum from a chaotic time series. *Phys. Rev. Lett.*, 55(10):1082–1085, 1985.

[6] P. Grassberger and I. Procaccia. Characterization of strange attractors. *Phys. Rev. Lett.*, 50:346, 1983.

[7] H.-l. Yang, K. A. Takeuchi, F. Ginelli, H. Chaté, and G. Radons. Hyperbolicity and the effective dimension of spatially extended dissipative systems. *Phys. Rev. Lett.*, 102(7):074102, 2009.

[8] B. Alberts. *Molecular Biology of the Cell*. Number p. 2 in Molecular Biology of the Cell. Garland Science, 2002.

[9] A. T. Winfree. *When time breaks down*. Princeton University Press, Cambridge, NJ, 1987.

[10] J. D. Murray. *Mathematical Biology*. Springer Verlag, New York, 1989.

[11] A. Goldbeter. *Biological Oscillations and Cellular Rhythms*. Cambridge University Press, Cambridge, UK, 1996.

[12] J. Keener and J. Sneyd. *Mathematical physiology*. Springer, New York, 1998.

[13] A. Winfree. *The Geometry of Biological Time*. Interdisciplinary applied mathematics: Mathematical biology. Springer, 1980.

[14] M. Loose, E. Fischer-Friedrich, J. Ries, K. Kruse, and P. Schwille. Spatial regulators for bacterial cell division self-organize into surface waves in vitro. *Science*, 320:789, 2008.

[15] J. Lechleiter, S. Girard, E. Peralta, and D. Clapham. Spiral calcium wave propagation and annihilation in xenopus laevis oocytes. *Science*, 252(5002):123–126, 1991.

[16] O. Steinbock, F. Siegert, S. C. Müller, and C. J. Weijer. Three-dimensional waves of excitation during morphogenesis of dictyostelium discoideum. *Proc. Natl. Acad. Sci. U.S.A.*, 90:7332, 1993.

[17] E. Pálsson, K. J. Lee, R. E. Goldstein, J. Franke, R. H. Kessin, and E. C. Cox. Selection for spiral waves in the social amoebae Dictyostelium. *Proc. Natl. Acad. Sci. U.S.A.*, 94:13719, 1997.

[18] A. Goldbeter. Oscillations and waves of cyclic AMP in Dicyostelium: A prototype for spatio-temporal organization and pulsatile intercellular communication. *Bulletin of Mathematical Biology*, 68:1095, 2006.

[19] J. M. Davidenko, A. M. Pertsov, R. Salomonsz, W. Baxter, and J. Jalife. Stationary and drifting spiral waves of excitation in isolated cardiac-muscle. *Nature (London)*, 355(6358):349, 1992.

[20] F. H. Fenton, E. M. Cherry, H. M. Hastings, and S. J. Evans. Multiple mechanisms of spiral breakup in a model of cardiac electrical activity. *Chaos*, 12:852, 2002.

[21] K. H. W. J. ten Tusscher, A. Mourad, M. P. Nash, R. H. Clayton, C. P. Bradley, D. J. Paterson, R. H. Hren, M. Hayward, A. V. Panfilov, and P. Taggart. Organization of ventricular fibrillation in the human heart: experiments and models. *Experimental Physiology*, 94:553, 2009.

[22] I. Rehberg, S. Rasenat, and V. Steinberg. Traveling waves and defect-initiated turbulence in electroconvecting nematics. *Phys. Rev. Lett.*, 62:756–759, 1989.

[23] Q. Ouyang and J. M. Flesselles. Transition from spirals to defect turbulence driven by a convective instability. *Nature (London)*, 379:143, 1996.

[24] C. Beta, A. S. Mikhailov, H. H. Rotermund, and G. Ertl. Defect-mediated turbulence in a catalytic surface reaction. *Europhys. Lett.*, 75(6):868–874, 2006.

[25] J.-S. Park and K. J. Lee. Line-defects-mediated complex-oscillatory spiral waves in a chemical system. *Phys. Rev. E*, 73:066219, 2006.

[26] S. Alonso, F. Sagués, and A. S. Mikhailov. Periodic forcing of scroll rings and control of Winfree turbulence in excitable media. *Chaos*, 16:023124, 2006.

[27] M. Cross and H. Greenside. *Pattern Formation and Dynamics in Nonequilibrium Systems*. Cambridge University Press, 2009.

[28] C. Gu, G. St-Yves, and J. Davidsen. Spiral wave chimeras in complex oscillatory and chaotic systems. *Phys. Rev. Lett.*, 111:134101, 2013.

[29] S. Shima and Y. Kuramoto. Rotating spiral waves with phase-randomized core in nonlocally coupled oscillators. *Phys. Rev. E*, 69:036213, 2004.

[30] A. Turing. The chemical basis of morphogenesis. *Philosophical Transactions of the Royal Society B*, 237:37–72, 1952.

[31] W. Tucker. The Lorenz attractor exists. *C. R. Acad. Sci. Paris*, 328(1):1197–1202, 1999.

[32] I. Stewart. The Lorenz attractor exists. *Nature (London)*, 406(6799):948–949, 2000.

[33] J. P. Crutchfield and K. Kaneko. Are attractors relevant to turbulence? *Phys. Rev. Lett.*, 60:2715–2718, 1988.

[34] P. Coullet, L. Gil, and J. Lega. Defect-mediated turbulence. *Phys. Rev. Lett.*, 62(14):1619–22, 1989.

[35] J. Davidsen and R. Kapral. Defect-mediated turbulence in systems with local deterministic chaos. *Phys. Rev. Lett.*, 91:058303, 2003.

[36] G. St-Yves and J. Davidsen. Defect mediated turbulence in a locally quasiperiodic chemical medium. *J. Chem. Phys.*, 133(4):044909, 2010.

[37] Q. Zhuang, X. Gao, Q. Ouyang, and H. Wang. Dynamical topology and statistical properties of spatiotemporal chaos. *Chaos*, 22(4), 2012.

[38] L. Gil, J. Lega, and J. L. Meunier. Statistical properties of defect-mediated turbulence. *Phys. Rev. A*, 41(2):1138–1141, 1990.

[39] D. A. Egolf. Dynamical dimension of defects in spatiotemporal chaos. *Phys. Rev. Lett.*, 81(19):4120–4123, 1998.

[40] M. P. Fishman and D. A. Egolf. Revealing the building blocks of spatiotemporal chaos: Deviations from extensivity. *Phys. Rev. Lett.*, 96(5):054103, 2006.

[41] K. A. Takeuchi, F. Ginelli, and H. Chaté. Lyapunov analysis captures the collective dynamics of large chaotic systems. *Phys. Rev. Lett.*, 103(15):154103, 2009.

[42] K. E. Daniels and E. Bodenschatz. Defect turbulence in inclined layer convection. *Phys. Rev. Lett.*, 88(3):034501, 2002.

[43] J. Davidsen, M. Zhan, and R. Kapral. Filament-induced surface spiral turbulence in three-dimensional excitable media. *Phys. Rev. Lett.*, 101:208302, 2008.

[44] H. Wang. Statistics of defect-mediated turbulence influenced by noise. *Phys. Rev. Lett.*, 93(15):154101, 2004.

[45] C. Huepe, H. Riecke, K. E. Daniels, and E. Bodenschatz. Statistics of defect trajectories in spatio-temporal chaos in inclined layer convection and the complex Ginzburg–Landau equation. *Chaos*, 14(3):864–874, 2004.

[46] A. Goryachev, R. Kapral, and H. Chaté. Synchronization defect lines. *Int. J. Bifurcation Chaos Appl. Sci. Eng.*, 10:1537, 2000.

[47] A. V. Holden. Cardiac physiology - a last wave from the dying heart. *Nature (London)*, 392:20, 1998.

[48] Blausen.com staff. Blausen gallery. Wikiversity Journal of Medicine, 2014.

[49] F. Fenton and A. Karma. Fiber-rotation-induced vortex turbulence in thick myocardium. *Phys. Rev. Lett.*, 81(2):481–484, 1998.

[50] F. Fenton and A. Karma. Vortex dynamics in three-dimensional continuous myocardium with fiber rotation: Filament instability and fibrillation. *Chaos*, 8(1):20–47, 1998.

[51] A. T. Winfree. Electrical turbulence in 3-dimensional heart-muscle. *Science*, 266:1003, 1994.

[52] A. L. Hodgkin and A. F. Huxley. Currents carried by sodium and potassium ions through the membrane of the giant axon of loligo. *J. Physiol.*, 116:449–472, 1952.

[53] C. H. Luo and Y. Rudy. A model of the ventricular cardiac action potential. depolarization, repolarization, and their interaction. *Circulation Research*, 68(6):1501–26,

1991.

[54] D. Noble and Y. Rudy. Models of cardiac ventricular action potentials: iterative interaction between experiment and simulation. *Philosophical Transactions of the Royal Society of London. Series A: Mathematical, Physical and Engineering Sciences*, 359(1783):1127–1142, 2001.

[55] S. Alonso, M. Bär, and A. V. Panfilov. Negative tension of scroll wave filaments and turbulence in three-dimensional excitable media and application in cardiac dynamics. *Bulletin of Mathematical Biology*, 75(8):1351–1376, 2013.

[56] A. Karma. Spiral breakup in model equations of action potential propagation in cardiac tissue. *Phys. Rev. Lett.*, 71(7):1103–1106, 1993.

[57] B. McLaughlin and K. Bennett. Supervenience. In E. N. Zalta, editor, *The Stanford Encyclopedia of Philosophy*. Spring 2014 edition, 2014.

[58] K. H. Ten Tusscher, R. Hren, and A. V. Panfilov. Organization of ventricular fibrillation in the human heart. *Circulation Research*, 100(12):e87–e101, 2007.

[59] R. Clayton and A. Panfilov. A guide to modelling cardiac electrical activity in anatomically detailed ventricles. *Prog. Biophys. Mol. Biol.*, 96(1-3):19 – 43, 2008.

[60] B. N. Roberts, P.-C. Yang, S. B. Behrens, J. D. Moreno, and C. E. Clancy. Computational approaches to understand cardiac electrophysiology and arrhythmias. *American Journal of Physiology - Heart and Circulatory Physiology*, 303(7):H766–H783, 2012.

[61] R. A. Gray, J. Jalife, A. V. Panfilov, W. T. Baxter, C. Cabo, J. M. Davidenko, A. M. Pertsov, A. V. Panfilov, P. Hogeweg, and A. T. Winfree. Mechanisms of cardiac fibrillation. *Science*, 270(5239):1222, 1995.

[62] P.-S. Chen, T.-J. Wu, C.-T. Ting, H. S. Karagueuzian, A. Garfinkel, S.-F. Lin, and J. N. Weiss. A tale of two fibrillations. *Circulation*, 108(19):2298–2303, 2003.

[63] E. M. Cherry and F. H. Fenton. Visualization of spiral and scroll waves in simulated and experimental cardiac tissue. *New Journal of Physics*, 10(12):125016, 2008.

[64] S. V. Pandit and J. Jalife. Rotors and the dynamics of cardiac fibrillation. *Circulation Research*, 112(5):849–862, 2013.

[65] A. T. Stamp, G. V. Osipov, and J. J. Collins. Suppressing arrhythmias in cardiac models using overdrive pacing and calcium channel blockers. *Chaos: An Interdisciplinary Journal of Nonlinear Science*, 12(3):931–940, 2002.

[66] Z. Cao, P. Li, H. Zhang, F. Xie, and G. Hu. Turbulence control with local pacing and its implication in cardiac defibrillation. *Chaos: An Interdisciplinary Journal of Nonlinear Science*, 17(1):–, 2007.

[67] S. Luther, F. H. Fenton, B. G. Kornreich, A. Squires, P. Bittihn, D. Hornung, M. Zabel, J. Flanders, A. Gladuli, L. Campoy, E. M. Cherry, G. Luther, G. Hasenfuss, V. I. Krinsky, A. Pumir, R. F. Gilmour, and E. Bodenschatz. Low-energy control of electrical turbulence in the heart. *Nature*, 475(7355):235–239, 2011.

[68] R. H. Clayton, E. A. Zhuchkova, and A. V. Panfilov. Phase singularities and filaments: Simplifying comlexity in computational models of ventricular fibrillation. *Prog. Biophys. Mol. Biol.*, 90:378, 2006.

[69] M. Bär and L. Brusch. Breakup of spiral waves caused by radial dynamics: Eckhaus and finite wavenumber instabilities. *New J. Phys.*, 6(1):5, 2004.

[70] R. C. Desai and R. Kapral. *Dynamics of self-organized and self-assembled structures.* Cambridge University Press, Cambridge, 2009.

[71] A. Goryachev and R. Kapral. Spiral waves in chaotic systems. *Phys. Rev. Lett.*, 76:1619–1622, 1996.

[72] J. Davidsen, R. Erichsen, R. Kapral, and H. Chaté. From ballistic to brownian vortex motion in complex oscillatory media. *Phys. Rev. Lett.*, 93:018305, 2004.

[73] J. P. Keener. The dynamics of three dimensional scroll waves in excitable media. *Physica D*, 31:269, 1988.

[74] V. N. Biktashev, A. V. Holden, and H. Zhang. Tension of organising filaments of scroll waves. *Philos. Trans. R. Soc. London Series A*, 347:611, 1994.

[75] V. N. Biktashev. A three-dimensional autowave turbulence. *International Journal of Bifurcation and Chaos*, 08(04):677–684, 1998.

[76] T. Bánsági and O. Steinbock. Negative filament tension of scroll rings in an excitable system. *Phys. Rev. E*, 76:045202R, 2007.

[77] T. Bánsági and O. Steinbock. Three-dimensional spiral waves in an excitable reaction system: Initiation and dynamics of scroll rings and scroll ring pairs. *Chaos: An Interdisciplinary Journal of Nonlinear Science*, 18(2):–, 2008.

[78] M. Hildebrand, M. Bär, and M. Eiswirth. Statistics of topological defects and spatiotemporal chaos in a reaction-diffusion system. *Phys. Rev. Lett.*, 75:1503, 1995.

[79] A. Goryachev, R. Kapral, and H. Chaté. Transitions to line-defect turbulence in complex oscillatory media. *Phys. Rev. Lett.*, 83(9):1878, 1999.

[80] G. D. Granzow and H. Riecke. Ordered and Disordered Defect Chaos. In *eprint arXiv:chao-dyn/9704020*, page 4020, 1997.

[81] G. D. Granzow and H. Riecke. Nonequilibrium defect-unbinding transition: Defect trajectories and loop statistics. *Phys. Rev. Lett.*, 87(17):174502, 2001.

[82] Reid, J. C., Chaté, H., and Davidsen, J. Filament turbulence in oscillatory media. *EPL*, 94(6):68003, 2011.

[83] M. P. Jiang Mi. Vortex turbulence due to the interplay of filament tension and rotational anisotropy. *Chinese Physics Letters*, 26(7):74703, 2009.

[84] G. St-Yves and J. Davidsen. Influence of the medium's dimensionality on defect mediated turbulence. *Phys. Rev. E*, 2014. submited.

[85] A. Pikovsky, M. Rosenblum, and J. Kurths. *Synchronization, A universal concept in nonlinear sciences*. Cambridge, 2001.

[86] S. Puwal, B. J. Roth, and S. Kruk. Automating phase singularity localization in mathematical models of cardiac tissue dynamics. *Mathematical Medicine and Biology*, 22(4):335–346, 2005.

[87] G. V. Osipov, B. Hu, C. Zhou, M. V. Ivanchenko, and J. Kurths. Three types of transitions to phase synchronization in coupled chaotic oscillators. *Phys. Rev. Lett.*, 91(2):024101, 2003.

[88] J. Davidsen and R. Kapral. Phase synchronization and topological defects in inhomogeneous media. *Phys. Rev. E*, 66:055202(R), 2002.

[89] P. S. Hagan. Spiral waves in reaction-diffusion equations. *Siam J. Appl. Math.*, 42(4):762–786, 1982.

[90] R. H. Clayton and A. V. Holden. A method to quantify the dynamics and complexity of re-entry in computational models of ventricular fibrillation. *Physics in Medicine and Biology*, 47:225, 2002.

[91] J. Hoshen and R. Kopelman. Percolation and cluster distribution. i. cluster multiple labeling technique and critical concentration algorithm. *Phys. Rev. B*, 14:3438–3445, 1976.

[92] T. Lewiner, J. ao D. Gomes Jr., H. Lopes, and M. Craizer. Arc-length based curvature estimator. *2012 25th SIBGRAPI Conference on Graphics, Patterns and Images*, 0:250–257, 2004.

[93] S. Nettesheim, A. van Oertsen, H. H. Rotermund, and G. Ertl. Reaction-diffusion patterns in the catalytic CO–oxidation on Pt(100): front propagation and spiral waves. *J. Chem. Phys.*, 98:9977, 1993.

[94] R. Imbihl and G. Ertl. Oscillatory kinetics in heterogeneous catalysis. *Chemical Reviews*, 95:697, 1995.

[95] W. Jahnke, W. E. Skaggs, and A. T. Winfree. Chemical vortex dynamics in the Belousov-Zhabotinsky reaction and in the two-variable oregonator model. *J. Chem. Phys.*, 93:740, 1989.

[96] M. Yoneyama, A. Fujii, and S. Maeda. Wavelength-doubled spiral fragments in photosensitive monolayers. *J. Am. Chem. Soc.*, 117:8188, 1995.

[97] J.-S. Park and K. J. Lee. Complex periodic spirals and line-defect turbulence in a chemical system. *Phys. Rev. Lett.*, 83:5393, 1999.

[98] J.-S. Park and K. J. Lee. Formation of a spiraling line defect and its meandering transition in a period-2 medium. *Phys. Rev. Lett.*, 88:224501, 2002.

[99] T. Y. Kim, S.-J. Woo, S.-M. Hawang, J. H. Hong, and K. J. Lee. Cardiac beat-to-beat alternations driven by unusual spiral waves. *Proc. Natl. Acad. Sci. U.S.A.*, 104:11639, 2007.

[100] Q. Ouyang, H. L. Swinney, and G. Li. Transition from spirals to defect-mediated turbulence driven by a doppler instability. *Phys. Rev. Lett.*, 84:1047, 2000.

[101] L. Q. Zhou and Q. Ouyang. Spiral instabilities in reaction-diffusion system. *J. Phys. Chem. A*, 105:112, 2001.

[102] B. Sandstede and A. Scheel. Period doubling of spiral waves and defects. *SIAM Journal on Applied Dynamical Systems*, 6:494, 2007.

[103] H. M. Hastings, F. H. Fenton, S. J. Evans, O. Hotomaroglu, J. Geetha, K. Gittelson, J. Nilson, and A. Garfinkel. Alternans and the onset of ventricular fibrillation. *Phys. Rev. E*, 62:4043–4048, 2000.

[104] T. Cameron and J. Davidsen. Induced spiral motion in cardiac tissue due to alternans. *Phys. Rev. E*, 86:061908, 2012.

[105] I. Aranson, L. Kramer, and A. Weber. Core instability and spatiotemporal intermittency of spiral waves in oscillatory media. *Phys. Rev. Lett.*, 72:2316–2319, 1994.

[106] I. S. Aranson and L. Kramer. The world of the complex Ginzburg-Landau equation. *Rev. Mod. Phys.*, 74:99–143, 2002.

[107] C. Qiao, H. Wang, and Q. Ouyang. Defect-mediated turbulence in the Belousov-Zhabotinsky reaction. *Phys. Rev. E*, 79:016212, 2009.

[108] G. Rousseau, H. Chaté, and R. Kapral. Twisted vortex filaments in the three-dimensional complex Ginzburg-Landau equation. *Chaos*, 18:026103, 2008.

[109] H. Chaté and P. Manneville. Phase diagram of the two-dimensional complex ginzburg-landau equation. *Physica A: Statistical Mechanics and its Applications*, 224(12):348 – 368, 1996.

[110] D. Krefting and C. Beta. Theoretical analysis of defect-mediated turbulence in a catalytic surface reaction. *Phys. Rev. E*, 81:036209, 2010.

[111] S. Jakubith, H. H. Rotermund, W. Engel, A. von Oertzen, and G. Ertl. Spatiotemporal concentration patterns in a surface reaction: Propagating and standing waves, rotating spirals, and turbulence. *Phys. Rev. Lett.*, 65(24):3013–3016, 1990.

[112] F. Argoul, A. Arneodo, P. Richetti, and J. C. Roux. From quasiperiodicity to chaos in the Belousov-Zhabotinsky reaction. I. experiment. *J. Chem. Phys.*, 86:3325, 1987.

[113] D. Barkley, J. Ringland, and J. S. Turner. Observations of a torus in a model of the Belousov-Zhabotinsky reaction. *J. Chem. Phys.*, 87:3812, 1987.

[114] M. R. Bassett and J. L. Hudson. Quasi-periodicity and chaos during an electrochemical reaction. *J. Phys. Chem.*, 93:2731, 1989.

[115] C. G. Steinmetz and R. Larter. The quasiperiodic route to chaos in a model of the peroxidase-oxidase reaction. *J. Chem. Phys.*, 94(2):1388–96, 1990.

[116] T. V. Bronnikova, W. M. Schaffer, and L. F. Olsen. Quasiperiodicity in a detailed model of the peroxidase-oxidase reaction. *J. Chem. Phys.*, 105:10849, 1996.

[117] L. F. Olsen, T. V. Bronnikova, and W. M. Schaffer. Secondary quasiperiodicity in the peroxidase-oxidase reaction. *Phys. Chem. Chem. Phys.*, 4:1292–8, 2002.

[118] M. Markus, S. C. Müller, and B. Hess. Observation of entrainment, quasiperiodicity and chaos in glycolysing yeast extract under periodic glucose input. *Ber. Bunsenges. Phys. Chem.*, 89:651, 1985.

[119] I. Martinez de la Fuente, L. Martinez, J. Veguillas, and J. M. Aguirregabiria. Quasiperiodicity route to chaos in a biochemical system. *Biophys. J.*, 71:2375–9, 1996.

[120] H. R. Petty, R. G. Worth, and A. L. Kindzelskii. Imaging sustained dissipative patterns in the metabolism of individual living cells. *Phys. Rev. Lett.*, 84:2754, 2000.

[121] L. F. Olsen, U. Kummer, A. L. Kindzelskii, and H. R. Petty. A model of the oscillatory metabolism of activated neutrophils. *Biophys. J.*, 84:69, 2003.

[122] H. G. Schuster. *Deterministic chaos*. VCH Verlag, Weinheim, Germany, 3rd extended edition, 1995.

[123] Z. Qu, J. N. Weiss, and A. Garfinkel. Spatiotemporal chaos in a simulated ring of cardiac cells. *Phys. Rev. Lett.*, 78(7):1387–90, 1997.

[124] W. F. Langford. Numerical studies of torus bifurcations. In *International series of numerical mathematics*, volume 70, page 285. Birkhäuser Verlag Basel, 1984.

[125] P. Richetti, J.-C. Roux, F. Argoul, and A. Arneodo. From quasiperiodicity to chaos in the belousov-zhabotinsky reaction. ii modeling and theory. *J. Chem. Phys.*, 86:3339–57, 1987.

[126] L. Su-Hua, J.-S. Tang, J.-Q. Qin, and X.-B. Yin. Bifurcation analysis and control of periodic solutions changing into invariant tori. *Chin. Phys. B*, 17(5):1691–7, 2008.

[127] H. Degn, L. F. Olsen, and J. W. Perram. Bistability, oscillation, and chaos in an enzyme reaction. *Ann. N.-Y. Acad. Sci.*, 316(1):623–37, 1979.

[128] T. V. Bronnikova, W. M. Schaffer, M. J. B. Hauser, and L. F. Olsen. Routes to chaos in the peroxidase-oxidase reaction. 2. the fat torus scenario. *J. Phys. Chem.*, 102:632–40, 1998.

[129] E. J. Doedel, R. C. Paffenroth, A. R. Champneys, T. F. Fairgrieve, Y. A. Kusnetsov, B. Sandstede, B. Oldeman, X. J. Wang, and C. Zhang. AUTO 07P–Continuation and bifurcation software for ordinary differential equations. *Department of Computer Science, Concordia University, Montreal, QC*, 2007.

[130] M. Bär and M. Eiswirth. Turbulence due to spiral breakup in a continuous excitable medium. *Phys. Rev. E*, 48:R1635–R1637, 1993.

[131] D. Barkley, M. Kness, and L. S. Tuckerman. Spiral-wave dynamics in a simple model of excitable media: The transition from simple to compound rotation. *Phys. Rev. A*, 42(4):2489–2492, 1990.

[132] S. Alonso, F. Sagués, and A. S. Mikhailov. Taming Winfree turbulence of scroll waves in excitable media. *Science*, 299:1722, 2003.

[133] H. Dierckx, H. Verschelde, O. Selsil, and V. N. Biktashev. Buckling of Scroll Waves. *Phys. Rev. Lett.*, 109(17), 2012.

[134] M. P. Nash, A. Mourad, R. H. Clayton, P. M. Sutton, C. P. Bradley, M. Hayward, D. J. Paterson, and P. Taggart. Evidence for multiple mechanisms in human ventricular fibrillation. *Circulation*, 114(6):536–542, 2006.

[135] S. Alonso and A. Panfilov. Negative filament tension in the luo-rudy model of cardiac tissue. *Chaos*, 17:015102, 2007.

[136] S. Alonso and A. Panfilov. Negative filament tension at high excitability in a model of cardiac tissue. *Phys. Rev. Lett.*, 100:217101, 2008.

[137] D. Barkley. A model for fast computer simulation of waves in excitable media. *Physica D: Nonlinear Phenomena*, 49(12):61 – 70, 1991.

[138] F. Sagués, S. Alonso, and J. M. Sancho. Scroll wave instability controlled by external fluctuations. *Physica A: Statistical Mechanics and its Applications*, 351(1):159 – 166, 2005.

[139] V. N. Biktashev and I. V. Biktasheva. Dynamics of filaments of scroll waves. *ArXiv e-prints*, 1403.6654, 2014.

[140] I. S. Aranson, A. R. Bishop, and L. Kramer. Dynamics of vortex lines in the three-dimensional complex ginzburg-landau equation: Instability, stretching, entanglement, and helices. *Phys. Rev. E*, 57:5276–5286, 1998.

[141] Z. Qu, F. Xie, and A. Garfinkel. Diffusion-induced vortex filament instability in 3-dimensional excitable media. *Phys. Rev. Lett.*, 83:2668–2671, 1999.

[142] S. Alonso, R. Kähler, A. S. Mikhailov, and F. Sagués. Expanding scroll rings and negative tension turbulence in a model of excitable media. *Phys. Rev. E*, 70:056201, 2004.

[143] A. Karma. Electrical alternans and spiral wave breakup in cardiac tissue. *Chaos*, 4(3):461–472, 1994.

[144] A. Hagberg and E. Meron. From labyrinthine patterns to spiral turbulence. *Phys. Rev. Lett.*, 72:2494–2497, 1994.

[145] C. Luengviriya, U. Storb, G. Lindner, S. Müller, M. Bär, and M. Hauser. Scroll wave instabilities in an excitable chemical medium. *Phys. Rev. Lett.*, 100:148302, 2008.

[146] K. O'Holleran, M. R. Dennis, and M. J. Padget. Topology of light's darkness. *Phys. Rev. Lett.*, 102:143902, 2009.

[147] A. Mitani and M. Tsubota. Self-organization of vortex-length distribution in quantum turbulence: an approach based on the Barabási-Albert model. *Phys. Rev. B*, 74:024526, 2006.

[148] E. A. L. Henn, J. A. Seman, G. Roati, K. M. F. Magalhães, and V. S. Bagnato. Emergence of turbulence in an oscillating Bose-Einstein condensate. *Phys. Rev. Lett.*, 103:045301, 2009.

[149] M. B. Hindmarsh and T. W. B. Kibble. Cosmic strings. *Rep. Prog. Phys.*, 58:477, 1995.

[150] S. Alonso, M. Bär, and A. V. Panfilov. Effects of reduced discrete coupling on filament tension in excitable media. *Chaos: An Interdisciplinary Journal of Nonlinear Science*, 21(1), 2011.

[151] M. Radszuweit, E. Alvarez-Lacalle, M. Bär, and B. Echebarria. Cardiac contraction induces discordant alternans and localized block. *Phys. Rev. E*, 91:022703, 2015.

[152] Z. Qu, J. Kil, F. Xie, A. Garfinkel, and J. N. Weiss. Scroll wave dynamics in a three-dimensional cardiac tissue model: Roles of restitution, thickness, and fiber rotation. *Biophysical Journal*, 78(6):2761 – 2775, 2000.

[153] R. Majumder, A. R. Nayak, and R. Pandit. Scroll-wave dynamics in human cardiac tissue: Lessons from a mathematical model with inhomogeneities and fiber architecture. *PLoS ONE*, 6(4):e18052, 2011.

[154] H. Wang and Q. Ouyang. Spatiotemporal chaos of self-replicating spots in reaction-diffusion systems. *Phys. Rev. Lett.*, 99(21):214102, 2007.

[155] W. H. Press, S. A. Teukolsky, W. T. Vetterling, and B. P. Flannery. *Numerical recipes, the art of scientific computing*. Cambridge university press, 3rd edition, 2007.